

THE EFFECTS OF GRAVITY MODULATION ON THE INSTABILITY  
OF DOUBLE-DIFFUSIVE CONVECTIONS IN A HORIZONTAL TANK

by

Youmin Yu

---

A Dissertation Submitted to the Faculty of the

DEPARTMENT OF AEROSPACE AND MECHANICAL ENGINEERING

In Partial Fulfillment of the Requirements  
For the Degree of

DOCTOR OF PHILOSOPHY  
WITH A MAJOR IN MECHANICAL ENGINEERING

In the Graduate College

THE UNIVERSITY OF ARIZONA

2006

## THE UNIVERSITY OF ARIZONA

## GRADUATE COLLEGE

As members of the Dissertation Committee, we certify that we have read the dissertation prepared by Youmin Yu

entitled The Effects of Gravity Modulation on the Instability of Double-Diffusive Convections in a Horizontal Tank

and recommend that it be accepted as fulfilling the dissertation requirement for the Degree of Doctor of Philosophy

\_\_\_\_\_  
Cho Lik Chan Date: 04/17/2006

\_\_\_\_\_  
Chuan F. Chen Date: 04/17/2006

\_\_\_\_\_  
Jeffrey W. Jacobs Date: 04/17/2006

\_\_\_\_\_  
Olgierd A. Palusinski Date: 04/17/2006

Final approval and acceptance of this dissertation is contingent upon the candidate's submission of the final copies of the dissertation to the Graduate College.

I hereby certify that I have read this dissertation prepared under my direction and recommend that it be accepted as fulfilling the dissertation requirement.

\_\_\_\_\_  
Dissertation Director: Cho Lik Chan Date: 04/17/2006

## STATEMENT BY AUTHOR

This dissertation has been submitted in partial fulfillment of requirements of requirements for an advanced degree at the University of Arizona and is deposited in the University Library to be made available to borrowers under rules of the Library.

Brief quotations from this dissertation are allowable without special permission, provided that accurate acknowledgment of source is made. Requests for permission for extended quotation from or reproduction of this manuscript in whole or in part may be granted by the head of the major department or the Dean of the Graduate College when in his or her judgment the proposed use of the material is in the interests of scholarship. In all other instances, however, permission must be obtained from the author.

SIGNED:     Youmin Yu

## ACKNOWLEDGEMENTS

I would like to take this opportunity to thank my advisors, Dr. C. F. Chen and Dr. C. L. Chan, for their guidance, supervision, encouragement, support and friendship throughout my six-year graduate study at the University of Arizona. They help me to build up not only my academic abilities but also many other valuable experiences. Our collaboration and friendship will be remembered forever.

I would also like to thank my committee members, Dr. J. W. Jacobs, Dr. R. N. Strickland and Dr. O. A. Palusinski. Their valuable comments and suggestions provide a new perspective to my research. Thanks also to the people in Machine Shop of the Department of Aerospace and Mechanical Engineering for their great contribution in building and setting up my experimental apparatus as well as the administrative staff in the department for their friendly assistance throughout my graduate study.

The financial support provided by NASA Grant NAG3-2354 for this work is gratefully acknowledged.

Finally, I would like to express thanks to my wife Jianhong and my daughters Xiaoxuan (Jenny) and Jessica. It is their love and support that make all these possible.

## TABLE OF CONTENTS

ABSTRACT.....	7
CHAPTER 1. INTRODUCTION.....	9
1.1. Overview.....	9
1.2. Previous Studies of Steady Gravity.....	10
1.3. Previous Studies of Gravity Modulation.....	12
1.4. Outline of Dissertation.....	15
CHAPTER 2. EXPERIMENTAL APPARATUS AND PROCEDURE.....	16
2.1. Experimental Apparatus.....	16
2.2. Experimental Procedure.....	18
2.3. Experimental Error.....	21
CHAPTER 3. NUMERICAL SIMULATIONS.....	23
3.1. Problem Formulation.....	23
3.2. Numerical Schemes.....	27
CHAPTER 4. DETERMINATION OF FREQUENCY OF INSTABILITY.....	29
CHAPTER 5. EXPERIMENTAL RESULTS AND DISCUSSION.....	31
5.1. Steady Gravity.....	31
5.2. Gravity Modulation.....	35
CHAPTER 6. NUMERICAL SIMULATIONS OF EXPERIMENTS.....	39
6.1. Steady Gravity.....	39
6.2. Ideal Gravity Modulation.....	43

TABLE OF CONTENTS -- Continued

6.3. Actual Gravity Modulation.....	43
CHAPTER 7. KINETIC ENEGY CONSIDERATION.....	46
7.1. Steady Gravity.....	46
7.2. Gravity Modulation of High Frequency.....	49
7.3. Gravity modulation of Low Frequency.....	50
CHAPTER 8. FURTHER COMPUTATIONAL INVESTIGATIONS.....	52
8.1. Resonance Phenomenon.....	53
8.2. Resonance Phenomenon Under Different Conditions.....	56
8.3. Density-Mode Instability.....	57
8.3.1. Interaction of Density-Mode and Double-Diffusive Instabilities.....	58
8.3.2. Density-Mode Instability.....	59
8.3.3. Effect of Density-Mode Instability.....	60
8.3.4. Cause of Density-Mode Instability.....	62
8.3.5. Density-Mode Instability under Modulation Amplitudes.....	64
8.4. Gravity Modulation Without Background Gravity.....	65
CHAPTER 9. CONCLUSIONS.....	70
APPENDIX A: FIGURES.....	74
APPENDIX B: TABLES.....	121
REFERENCES.....	129

## ABSTRACT

The effects of gravity modulation on the instability of double-diffusive convections in a horizontal tank with aspect ratio (width/height) of 11 have been investigated by experiments and numerical simulations. The stably stratified fluid layer is set up with ethanol-water solution of 0.0 and 2.0% (by weight). The tank is fixed on a platform that can oscillate in the vertical direction. A constant temperature difference is maintained across the tank at thermal Rayleigh number  $Ra_T = 161,560$ . The fluid layer becomes unstable as the initially stable solute gradient slowly decreases due to the non-diffusive boundary conditions. The experiments determine that the instability onset under steady gravity is at  $Ra_S = 125,540$  with onset vortices of wavelength  $\lambda = (0.91 \sim 1.09)$  and oscillatory frequency  $f_{onset} = 27.02$ . When the tank is oscillated at modulation frequency  $\omega_m = 628.3$  and amplitude  $gy_1 = 0.403$ , the fluid layer is destabilized slightly with a critical  $Ra_S = 136,140$  and onset vortices of  $\lambda = (1.39 \sim 2.26)$  and  $f_{onset} = 35.81$ . A two-dimensional numerical simulation has accurately reproduced the experimental results of steady gravity, and demonstrated that the slight destability effect of gravity modulation is contributed by the asymmetry of the actual gravity modulation.

Further simulations have yielded following results: (1) Under steady gravity, the kinetic energy and mechanical work components oscillate synchronously with  $f_{onset}$ . Under modulated gravity, they only oscillate synchronously with  $\omega_m$  when  $\omega_m$  is low, whereas not only synchronously with  $\omega_m$  locally but also synchronously with  $f_{onset}$ .

globally when  $\omega_m$  is high; (2) The resonance phenomenon predicted by Chen (2001) also exists under the present lab conditions. Such instability is in the sub-harmonic mode and the destability effect increases as  $gy_1$  increases. (3) The double-diffusive fluid layer may experience density-mode instability before the double-diffusive instability onset at certain  $\omega_m$  and  $gy_1$ . Such density-mode instability is generally in the sub-harmonic mode, although it may be in the synchronous mode when  $\omega_m$  is low and  $gy_1$  is large. This instability accelerates the mixing of the density gradient across the fluid layer and thus affects the succeeding double-diffusive instability; (4) When the background gravity  $gy_0$  is absent, the purely modulated gravity  $gy_1$  destabilizes the fluid layer when  $\omega_m$  is low. On the contrary, it stabilizes the fluid layer when  $\omega_m$  is high and the instability onset is in the synchronous mode.

## CHAPTER 1.

### INTRODUCTION

#### 1.1. Overview

When a fluid in a gravitational field contains two components with different molecular diffusivities that make opposite contributions to the density gradient of the fluid in the vertical direction, double-diffusive phenomenon occurs. Two modes of instability are possible: a “finger” mode if the component with smaller diffusivity is heavy on top or a “diffusive” mode if the component with larger diffusivity is heavy on top. In both cases instability may onset when the overall density distribution is still stable. Taking heat (temperature) and solute (salt) as the two typical diffusive components in a salt-water solution in which the thermal diffusivity is roughly one hundred times larger than the solutal diffusivity, the instability in the case of stably stratified salt-water solution layer heated from below is in the “diffusive” mode and the instability in the opposite case of the unstably stratified salt-water solution layer heated from above is in the “finger” mode. Although the initial research about this topic was in the field of oceanography, the study of double-diffusive convection has been finding its applications in many areas, such as metallurgy, chemistry, geophysics, etc. Turner (1974, 1985) and Huppert & Turner (1981) reviewed the early work of double-diffusive phenomena in detail. Schmitt (1994) summarized the later development of double-diffusive knowledge in oceanography. Chen & Johnson (1984) summarized the engineering applications of double-diffusive convections.

Similar to other natural convections, the double-diffusive convections are the consequences of mutual interactions of the gravitational body force and the fluid density gradients. In other words, the existences of the double-diffusive convections cannot be isolated from the gravitational field. Therefore, it is natural to imagine that the double-diffusive convections may be reduced and even eliminated in microgravity environments (for instance, space stations) when they are unwanted, or may be enhanced by changing gravity when they are desired. Both cases may be practical in engineering applications, for example, material processing and crystal growth. However, it is well known that microgravity in a space station fluctuates in frequency, amplitude and direction. Such fluctuation is often referred to as g-jitter. Compared with the steady gravity, the g-jitter may affect the convections significantly. Therefore, it is of great importance to understand the effects of gravity modulation on the double-diffusive phenomena.

Even they are simply due to the two components, the ‘finger’ and ‘diffusive’ regimes under steady gravity display fundamentally different features of instability onset and subsequent convections. The gravity modulations can stabilize or destabilize the onset and subsequent convections. All these topics deserve investigations. In this dissertation, the focus of attention is the effect of gravity modulation on the onset of the double-diffusive instability in the ‘diffusive’ regime. The related previous work is reported below.

## 1.2. Previous Studies of Steady Gravity

The study of double-diffusive convections under steady gravity started in the early 1960s. The instability onset of the convections is characterized as oscillatory motion in terms of frequency and wave number. Shirtcliffe (1967) reported the first experimental observation of an oscillatory onset of the double-diffusive convection in a sugar-water layer. The oscillatory motion at onset is displayed by the differential output of two thermocouples set vertically apart from each other near the bottom of the layer. Turner (1968) experimentally observed the oscillatory onset in a salt-water solution by the fluctuations of the temperature gradient recorded with two thermistors. Shirtcliffe (1969) presented stability diagrams in the  $Ra_T - Ra_S$  plane ( $Ra_T$  is the thermal Rayleigh number;  $Ra_S$  is the solutal Rayleigh number) and the cellular motions at onset demonstrated by schlieren pictures. In his experiments, the solute gradient of sugar (equivalently  $Ra_S$ ) decreases slowly and therefore is approximately constant; while the temperature gradient (equivalently  $Ra_T$ ) increases quickly and therefore is unsteady. Baines & Gill (1969) examined the stability problem with fixed linear temperature and solute gradients and dynamically free boundary conditions using linear stability analysis. Marginal stability maps are presented in the  $Ra_T - Ra_S$  plane, in which the conditions for different instability modes such as stable, oscillating unstable only, direct and oscillating unstable, and direct unstable only, are specified. To get a better comparison with analytical predictions, Wright & Loehrke (1976) investigated this problem again by experiments. By bounding a salt-water solution layer with two porous plates through which both salt and heat can diffuse, they established the similar linear solute and

temperature profiles and specified boundary conditions to linear stability analysis. They found that the instability limit for their system lies within the unstable region predicted by linear theory and approaches the linear boundary of instability at high  $Ra_T$  and  $Ra_S$ .

### 1.3. Previous Studies of Gravity Modulation

The gravity modulation usually is modeled as a sinusoidal modulation specified by frequency and amplitude. Based on its relation to the modulation frequency, the instability onset of single- and double-diffusive convections is generally classified as one of the three modes: synchronous mode when the oscillatory frequency is equal to the modulation frequency, sub-harmonic mode when the instability motion oscillates at half of the modulation frequency, and quasi-periodic mode when the onset frequency is different from the above two values. The effect of gravity modulation was studied first in a single-diffusive fluid layer by Gresho & Sani (1970). They examined the stability of a horizontal pure water layer heated from either above or below under a sinusoidal modulation of the gravitational field by linear stability analysis. They found that the gravity modulation can significantly affect the stability limits of the layer. Specifically, a uniform fluid layer heated from below can be stabilized by gravity modulations of high frequency and small amplitude, and the same layer heated from above can be destabilized by modulations of high frequency and large amplitude. The vortices of onset motion respond synchronously when the modulation frequency is low and sub-harmonically

when the frequency is high. Clever, Schubert & Busse (1993) expanded this problem over a much wider range of modulation frequencies and amplitudes and into different fluids.

The effects of the gravity modulation on the double-diffusive convections were extended naturally from the single diffusions. Saunders et al (1992) investigated the effects of vertically time-periodic gravity modulation on the onset of thermosolutal convection in an infinite horizontal layer by linear stability analysis. The basic state consists of stationary fluid layer with linear temperature and solute profiles, stress-free boundary conditions and with or without steady background gravity. They found that unstable resonances due to the gravity modulation occur at states which are stable in the corresponding unmodulated system. The resonances are shown as a series of sharp dips on the neutral stability curve with most critical one of highest frequency. All dips are alternatively synchronous and sub-harmonic, and exhibit strong coupling with the oscillatory frequency of instability onset of the unmodulated system. In a word, gravity modulation may destabilize a stable flow sharply at certain modulation frequencies. Terrones & Chen (1993) studied the effects of the gravity modulation and cross diffusion on the same system but with rigid boundaries by linear stability analysis. A striking feature they reported in the gravity modulated doubly cross-diffusive fluid layers is the existence of bifurcating neutral stability curves with double minima, one of which corresponds to a quasi-periodic branch and the other to a sub-harmonic branch. In other words, at a same  $Ra_T$ , there are possibly two incommensurate critical wave numbers at two incommensurate onset frequencies. Further more, the latter branch is more sensitive

to small parameter variations than the former branch. Chen (2001) analytically investigated the bifurcation phenomenon. By checking three different fluids under different frequencies and amplitudes of the gravity modulation, it turns out that the bifurcation is a resonance in the sub-harmonic mode in the range of low modulation frequencies. Therefore, the gravity modulation of low frequency may also decrease the stability limit of fluid layers compared with the steady gravity case. Furthermore, the destabilization generally increases as the amplitude of modulation increasing, and the resonant effects become more significant in fluids of low Prandtl number. Jue & Ramaswamy (2002) investigated the heat and mass transfer of the thermosolutal convective flow in a two-dimensional rectangular cavity (aspect ratio  $A = 2$ ) under sinusoidal gravity modulations for a series of modulation frequencies by direct non-linear simulation. The continuity, Navier-Stokes, energy and solute equations were solved by a finite element method. They found, for different modulation frequencies, there are two types of response of flow evolution -- synchronous and sub-harmonic. The responses affect the heat and mass transfer rates. The overall Nusselt number and Sherwood number exhibit larger values for the sub-harmonic flow field.

While the gravity modulation is usually simplified by a sinusoidal fluctuation, the actual g-jitter measured in space stations is random in both time and direction. Shu, Li & de Groh (2001) conducted a numerical study on the real g-jitter induced double-diffusive convection in a micro-gravity environment. Their simulated results show that both the velocity and solute become random following approximately the same pattern as the g-

jitter perturbations. No related experimental investigations on the double-diffusive instability have been found so far to the best of the author's search.

#### 1.4. Outline of Dissertation

In the present work, the effects of gravity modulation on the double-diffusive convection have been investigated by experiments and by direct numerical simulations. Here is the outline of this dissertation. The experimental apparatus and procedure are described in Chapter 2 and the method of numerical simulations in Chapter 3. Since the oscillatory frequency of the instability onset is of great importance in this study, Chapter 4 is devoted to briefly introduce the method to determine it using power spectrum estimations. The experimental and corresponding numerical results are presented and discussed in Chapter 5 and 6 respectively. The consideration of kinetic energy is presented in Chapter 7. Then, attention is dedicated in Chapter 8 to further computational investigation of the effects of gravity modulation, which are difficult to be conducted by experiments. Last, conclusions of this work are summarized in Chapter 9.

## CHAPTER 2.

### EXPERIMENTAL APPARATUS AND PROCEDURE

#### 2.1. Experimental Apparatus

Experiments were conducted in a shallow horizontal tank (see figure 1) with interior dimensions of 108 mm wide  $\times$  10 mm high  $\times$  54 mm deep. The tank is transparent from top and side views for visualization purpose. All sidewalls are made of 12.7-mm-thick Plexiglas. The cover of the tank is a sealed shallow box made of Plexiglas except its bottom, which is made of 1-mm-thick transparent Sapphire plate and served as the upper boundary of the fluid layer. The transparent glycerin-water solution from a constant temperature bath is circulated through the box to keep the temperature of the sapphire plate constant at a set temperature. The upper boundary temperature of the fluid layer is maintained at a constant value due to the high thermal conductivity of sapphire. The lower boundary of the fluid layer is the bottom wall of the tank made of 12.7-mm-thick copper plate with sealed passages in it. The temperature of the copper plate is maintained by circulating coolant supplied by another constant temperature bath, so that the temperature of fluid layer on the lower boundary is constant as well. The temperature of the lower boundary is measured by a thermocouple embedded in the copper plate. The temperature of the upper boundary, rather than being measured which is limited by the visualization and thin thickness of sapphire plate, is deduced using the following procedure: determine the flow condition of the glycerin-water solution in the cover box

according to the circulation rate of the bath and the geometry of the box, so that the heat transfer coefficient of the glycerin-water flow is determined using the correlation given by Incropera & DeWitt (2002) (Page 492); calculate the thermal resistances of the glycerin-water flow, sapphire plate and ethanol-water solution of double-diffusive fluid layer; measure the temperatures at the inlet and outlet of the box with thermocouples to obtain the average temperature of the glycerin-water flow; lastly, with the average temperature, the temperature of the lower boundary and the related thermal resistances available, calculate the temperature on the upper boundary using equivalent thermal circuits in the vertical direction (see figure 2). The temperature difference  $\Delta T$  between the upper and lower boundaries of the fluid layer is then used to calculate the thermal Rayleigh number  $Ra_T = (g\beta_T H^3 \Delta T) / (\kappa_T \nu)$ .

An oscillating platform is used to impact gravity modulation in the vertical direction. By using a Scotch-Yoke mechanism, the rotary motion of a flywheel driven by a DC motor is transformed into sinusoidal vertical motions of a vertical shaft (see figure 3). The platform is mounted rigidly on the shaft. The vertical trace of the shaft is 100 mm. The test tank and a digital camera are mounted on the oscillating platform so that the camera is able to record any motion of the fluid in the tank while the entire system is under oscillation. The desired frequency and amplitude of gravity modulation are controlled by adjusting the input current of DC motor. When the platform is oscillating at  $1.0\text{Hz}$ , the acceleration of the platform is  $3.948\text{m}^2/\text{s}$  or  $0.403\text{g}$ . The acceleration of the platform is measured by an accelerometer fixed on the platform. All the signals of temperature and gravity modulation are streamed into a personal computer through

hardware configuration. With a code developed in LabVIEW, the signals are then displayed, processed and saved (see figure 4).

For flow visualization and PIV (Particle Image Velocimetry) purposes, the test fluid is seeded with 10- $\mu\text{m}$  polycrystalline particles. A Coherent 4 W laser provides the light source. The initial laser light beam is rendered into a light sheet of approximately 1 mm thickness by a set of cylindrical lenses and the light sheet is deflected downward to illuminate the mid-plane of the tank. The motions of illuminated particles are captured by the camera and streamed into a Macintosh computer as movie clips. The movie clips are then used to construct streaklines of flow motions and are analyzed by PIV software to get the velocities of the flow field. Some detailed information about the experimental apparatus is also described by Yu (2002). The hooked-up experimental apparatus are shown in figure 5.

## 2.2. Experimental Procedure

The fluids used to set up the stratified fluid layer are 0.0% and 2.0% (by weight) ethanol-water solutions. The thermophysical properties of the fluid layer are evaluated at the mixed 1.0% ethanol-water solution, which can be found in Landolt & Bornstein (1989). At 22.5°C, the kinematic viscosity  $\nu = 1.005 \times 10^{-6} \text{ m}^2/\text{s}$ , thermal diffusivity  $\kappa_T = 1.429 \times 10^{-7} \text{ m}^2/\text{s}$ , solutal diffusivity  $\kappa_S = 1.208 \times 10^{-9} \text{ m}^2/\text{s}$ , thermal expansion coefficient  $\beta_T = 2.330 \times 10^{-4} 1/\text{K}$ , and solutal expansion coefficient  $\beta_S = 1.863 \times 10^{-3} 1/\text{wt}\%$ , which yield the Prandtl number  $\text{Pr} = 7.033$  and the Lewis number  $Le = 118.295$  for the fluid.

To set up a stably stratified fluid layer, the isothermal seeded pure water (0.0%) is first poured into the test tank. Then, a 50 mm × 25 mm thin piece of Balsa wood floats on it. The equal amount of isothermal seeded 2.0% ethanol-water solution is then injected slowly on the wood piece by a syringe so that turbulent mixing can be reduced as much as possible. Last, the wood piece is removed carefully and the cover box is secured to the tank by four screws. A nearly stepwise distribution of solute is therefore setup. The filled tank is then left standing 30 min for the ethanol to diffuse.

The transient solute distribution of the fluid in the vertical direction in the tank is calculated by the one-dimensional transient mass diffusion equation

$$\frac{\partial S^*}{\partial t^*} = \kappa_s \frac{\partial^2 S^*}{\partial y^{*2}} \quad (1)$$

where  $S^*$  is solute,  $\kappa_s$  solute diffusivity,  $t^*$  time and  $y^*$  vertical distance in dimensional form. With the same experimental boundary conditions

$$\frac{\partial S^*}{\partial y^*} = 0 \text{ at } y = 0, 10mm \quad (2)$$

and the initial conditions

$$S^* = 2.0\% \text{ when } 6.65mm \leq y \leq 10mm \quad (3)$$

$$S^* = \frac{2.0}{33.0}(y - 33.5)\% \text{ when } 3.35mm < y < 6.65mm \quad (4)$$

$$S^* = 0.0\% \text{ when } 0mm \leq y \leq 3.35mm \quad (5)$$

Eq. (1) is approximated by finite difference method and solved by Crank-Nicolson method. The effects of different initial conditions will be discussed in section 2.3. Figure 6 shows the solute distributions at different times estimated by Eq. (1). The solute difference between the upper and lower boundaries is used to calculate the solutal Rayleigh number  $Ra_s = (g\beta_s H^3 \Delta S^*) / (\kappa_T \nu)$  at a given time.

According to the solution of Eq. (1), the solute distribution is smooth enough to start experiments after 30 min. The coolant of different temperatures (the bottom one is higher than the top one) from two baths starts circulating to control an intended temperature difference between the upper and lower boundaries. The temperature and gravity modulation signals are displayed on the PC and the images of fluid layer on the Macintosh computer. The linear temperature distribution is reached quickly (less than 3 min) and then is kept constant throughout the entire experiment while the solute of ethanol keeps diffusing. Therefore, the  $Ra_T$  is maintained constant (due to the constant temperature difference) whereas the  $Ra_s$  is decreasing (due to the ethanol diffusion) (see figure 6). The quiescent fluid layer is being monitored by the camera. The first detected motion of fluid is defined as the instability onset and is captured as movie clips. The time it takes from the start of the experiment to the onset of motion is recorded as the onset time of the instability,  $t_{onset}$ . After the end of the experiment, the movie clips are exported as frame sequences. The streakline images of fluid motions at onset are constructed by superposing suitable number of consecutive frames. The velocities of fluid motions at onset are obtained by analyzing the frames using the PIV program.

### 2.3. Experimental Error

The experimental error mainly arises in determining the thermal Rayleigh number  $Ra_T$ , the critical solutal Rayleigh number  $Ra_S$ , the oscillation frequency of instability onset  $f_{onset}$  and the time of onset  $t_{onset}$ . The accuracy of  $Ra_T$  is determined by the measurement error of the temperature difference  $\Delta T$ . With the actual  $\Delta T \geq 10.0^\circ\text{C}$  (see second column in Table 1 and 2) and the maximum thermocouple error of  $\pm 0.1^\circ\text{C}$  (the actual measured error saved in LabVIEW is within  $\pm 0.1^\circ\text{C}$  because the averaging algorithm in the LabVIEW code already cancels out most of the random error), the relative accuracy of  $Ra_T$  is within  $\pm 1.0\%$ .

The error of  $Ra_S$  is due to the uncertainty in estimating the solute difference  $\Delta S$ . The uncertainty is mainly decided by the initial condition when calculating the  $\Delta S$  in the one-dimensional transient diffusion. Considering the unavoidable turbulent mixing when filling the tank, the initial condition is chosen as Eq. (3), (4) and (5), that is, uniform distribution of 2.0% ethanol-water solution in upper one-third fluid layer, linear distribution in the mid one-third fluid layer and 0.0% ethanol-water in lower one-third fluid layer. The two possible extreme cases of the initial condition are completely step-wise distribution (2.0% ethanol-water solution in the upper half of the fluid layer and 0.0% ethanol-water solution in the lower half of the fluid layer) and completely linear distribution. The difference between the two cases and the adopted initial condition (Eq.(3), (4) and(5)) are +2.81% and -29.0%. The shadowgraph of the solute distribution

right after the filling in figure 7 shows that the actual situation is more likely to be the step-wise case rather than the linear case. Therefore the adopted initial distribution is reasonable. The filling procedure in the present experiments is similar to those in the double-diffusive convections studied by Chen, Briggs & Wirtz (1971) and Tanny & Chen (1995), in both of which the transient solute profiles are calculated and are confirmed by actual measurements of the distribution. Chen, Briggs & Wirtz (1971) estimated that their uncertainty in solute gradient is within  $\pm 3.0\%$ . Tanny & Chen (1995) reported that the calculated profile is almost the same as the measured one. Therefore, the relative error of  $Ra_S$  in present experiments is deduced within  $\pm 3.0\%$  as well.

When conducting the power spectrum estimation to determine the discrete onset frequency, the frequency increment is less than  $0.002\text{Hz}$  in dimensional form. The corresponding error of the onset frequency  $f_{onset}$  thus is within  $\pm 4.65\%$  (knowing that  $f_{onset} = 0.043\text{Hz}$  is a typical value in the experiments). The uncertainty of the onset time  $t_{onset}$  is within  $\pm 1.18\%$  as a result that  $t_{onset}$  in every single experiment is rounded up to minute and all  $t_{onset} \geq 82\text{ min}$ .

Overall speaking, the uncertainty in present experiments is within  $\pm 5.0\%$  in terms of  $Ra_T$ ,  $Ra_S$ ,  $f_{onset}$  and  $t_{onset}$ .

## CHAPTER 3.

## NUMERICAL SIMULATIONS

## 3.1. Problem Formulation

The double-diffusive convection has also been investigated using direct non-linear simulations. Here we assume two-dimensional double-diffusive convection of a Newtonian fluid in a horizontal tank of width  $W$  and height  $H$  with aspect ratio  $A = W/H = 11$ . The temperatures of the top and bottom walls are kept at constant  $T_t$  and  $T_b (> T_t)$  respectively while the sidewalls are held adiabatic. The solute on all walls is non-diffusive. The coordinate system is shown in figure 8. With the Boussinesq approximation, dimensional governing equations of the transient, incompressible double-diffusive convection of constant properties except variable viscosity are

$$\frac{\partial u^*}{\partial x^*} + \frac{\partial v^*}{\partial y^*} = 0 \quad (6)$$

$$\begin{aligned} \rho \left( \frac{\partial u^*}{\partial t^*} + u^* \frac{\partial u^*}{\partial x^*} + v^* \frac{\partial u^*}{\partial y^*} \right) = & -\frac{\partial p^*}{\partial x^*} + \rho (gx_0^* + gx_1^* \cos(\Omega t^*)) [\beta_T (T^* - T_0) - \beta_S (S^* - S_0)] \\ & + \frac{\partial}{\partial x^*} \left( \mu \left( 2 \frac{\partial u^*}{\partial x^*} \right) \right) + \frac{\partial}{\partial y^*} \left( \mu \left( \frac{\partial u^*}{\partial y^*} + \frac{\partial v^*}{\partial x^*} \right) \right) \end{aligned} \quad (7)$$

$$\begin{aligned} \rho \left( \frac{\partial v^*}{\partial t^*} + u^* \frac{\partial v^*}{\partial x^*} + v^* \frac{\partial v^*}{\partial y^*} \right) = & -\frac{\partial p^*}{\partial y^*} + \rho (gy_0^* + gy_1^* \cos(\Omega t^*)) [\beta_T (T^* - T_0) - \beta_S (S^* - S_0)] \\ & + \frac{\partial}{\partial x^*} \left( \mu \left( \frac{\partial u^*}{\partial y^*} + \frac{\partial v^*}{\partial x^*} \right) \right) + \frac{\partial}{\partial y^*} \left( \mu \left( 2 \frac{\partial v^*}{\partial y^*} \right) \right) \end{aligned} \quad (8)$$

$$\frac{\partial T^*}{\partial t^*} + u^* \frac{\partial T^*}{\partial x^*} + v^* \frac{\partial T^*}{\partial y^*} = \kappa_T \left( \frac{\partial^2 T^*}{\partial x^{*2}} + \frac{\partial^2 T^*}{\partial y^{*2}} \right) \quad (9)$$

$$\frac{\partial S^*}{\partial t^*} + u^* \frac{\partial S^*}{\partial x^*} + v^* \frac{\partial S^*}{\partial y^*} = \kappa_S \left( \frac{\partial^2 S^*}{\partial x^{*2}} + \frac{\partial^2 S^*}{\partial y^{*2}} \right) \quad (10)$$

where  $T_0 = (T_b + T_t)/2$  is the reference temperature,  $S_0 = 1.0\%$  the reference solute, and gravities in both  $x$ - and  $y$ - directions are written as sum of constant background part  $g_0^*$  and modulated part  $g_1^* \cos(\Omega t^*)$ . The corresponding boundary conditions are

$$u = v = 0, \quad \frac{\partial S^*}{\partial x^*} = 0, \quad \frac{\partial T^*}{\partial x^*} = 0 \quad \text{at } x = 0, 108 \text{ mm} \quad (11)$$

$$u = v = 0, \quad \frac{\partial S^*}{\partial y^*} = 0, \quad T^* = T_b, T_t \quad \text{at } y = 0, 10 \text{ mm} \quad (12)$$

Introducing characteristic quantities  $W$  for horizontal length,  $H$  for vertical length,  $H^2/\nu$  for time,  $\nu/H$  for velocity,  $g (= 9.807 m/s^2)$  and  $\nu/H^2$  for amplitude and frequency of gravity modulation, the non-dimensional governing equations written in terms of streamfunction  $\psi$  and vorticity  $\omega$ , are

$$\frac{\partial^2 \psi}{A^2 \partial x^2} + \frac{\partial^2 \psi}{\partial y^2} = -\omega \quad (13)$$

$$\begin{aligned}
\frac{\partial \omega}{\partial t} = & \underbrace{\left( \frac{\partial \psi}{A \partial x} \frac{\partial \omega}{\partial y} - \frac{\partial \psi}{\partial y} \frac{\partial \omega}{A \partial x} \right)}_{(a)} + \underbrace{f_v \left( \frac{\partial^2 \omega}{A^2 \partial x^2} + \frac{\partial^2 \omega}{\partial y^2} \right)}_{(b)} \\
& + \underbrace{\frac{Ra_T}{Pr} (gy_0 + gy_1 \cos(\omega_m t)) \frac{\partial \theta}{A \partial x} - \frac{Ra_T}{Pr} (gx_0 + gx_1 \cos(\omega_m t)) \frac{\partial \theta}{\partial y}}_{(c)} \\
& - \underbrace{\frac{Ra_S}{Pr} (gy_0 + gy_1 \cos(\omega_m t)) \frac{\partial C}{A \partial x} + \frac{Ra_S}{Pr} (gx_0 + gx_1 \cos(\omega_m t)) \frac{\partial C}{\partial y}}_{(d)} \\
& + 2 \underbrace{\left( \frac{\partial f_v}{A \partial x} \frac{\partial \omega}{A \partial x} + \frac{\partial f_v}{\partial y} \frac{\partial \omega}{A \partial y} \right) - \left( \frac{\partial^2 f_v}{A^2 \partial x^2} - \frac{\partial^2 f_v}{\partial y^2} \right) \left( \frac{\partial^2 \psi}{A^2 \partial x^2} - \frac{\partial^2 \psi}{\partial y^2} \right) - 4 \frac{\partial^2 f_v}{A \partial x \partial y} \frac{\partial^2 \psi}{A \partial x \partial y}}_{(e)}
\end{aligned} \tag{14}$$

$$\frac{\partial \theta}{\partial t} = \underbrace{\left( \frac{\partial \psi}{A \partial x} \frac{\partial \theta}{\partial y} - \frac{\partial \psi}{\partial y} \frac{\partial \theta}{A \partial x} \right)}_{(a)} + \underbrace{\frac{1}{Pr} \left( \frac{\partial^2 \theta}{A^2 \partial x^2} + \frac{\partial^2 \theta}{\partial y^2} \right)}_{(b)} \tag{15}$$

$$\frac{\partial C}{\partial t} = \underbrace{\left( \frac{\partial \psi}{A \partial x} \frac{\partial C}{\partial y} - \frac{\partial \psi}{\partial y} \frac{\partial C}{A \partial x} \right)}_{(a)} + \underbrace{\frac{1}{Pr Le} \left( \frac{\partial^2 C}{A^2 \partial x^2} + \frac{\partial^2 C}{\partial y^2} \right)}_{(b)} \tag{16}$$

where  $u = \partial \psi / \partial y$ ,  $v = -\partial \psi / A \partial x$ , and  $\omega = \partial v / A \partial x - \partial u / \partial y$ . The non-dimensional temperature  $\theta$  and solute  $C$  are defined as  $\theta = (T^* - T_0) / \Delta T$  and  $C = (S^* - S_0) / \Delta S$  where  $\Delta T = T_b - T_t$  the imposed temperature difference in experiments and  $\Delta S = S_b - S_t$  the solute difference after 30-min diffusion from Eq. (1). The non-dimensional parameters are defined as: aspect ratio  $A = W/H$ , Prandtl number  $Pr = \nu / \kappa_T$ , Lewis number  $Le = \kappa_T / \kappa_S$ , thermal Rayleigh number  $Ra_T = (g \beta_T H^3 \Delta T) / (\kappa_T \nu)$ , solutal Rayleigh number  $Ra_S = (g \beta_S H^3 \Delta S) / (\kappa_T \nu)$ , and  $f_v = f_v(\theta)$  is the kinematic viscosity

ratio and it is approximated as  $f_v(\theta) = 1 - 0.24888\theta$ , which corresponds to the viscosity variation due to the actual temperature difference in experiments. The related boundary conditions are

$$\psi = \frac{\partial \psi}{\partial x} = 0, \quad \frac{\partial \theta}{\partial x} = 0, \quad \frac{\partial C}{\partial x} = 0 \quad \text{at } x = 0, 1 \quad (17)$$

$$\psi = \frac{\partial \psi}{\partial y} = 0, \quad \theta = 0.5, \quad -0.5, \quad \frac{\partial C}{\partial y} = 0 \quad \text{at } y = 0, 1 \quad (18)$$

The initial conditions are the quiescent state at the uniform  $\theta = 0.0$  and the solutal distribution after 30-min diffusion from Eq (1). The  $Ra_T$  s and  $Ra_S$  s are written as positive quantities such that thermal buoyancy makes the fluid layer unstable and solutal buoyancy makes it stable.

Eq. (13), (14), (15) and (16) are general forms for the problem. Under specific cases, they may be simplified. Although the convective terms (a) are always there, they are zero before the instability onset. Therefore, the solutal distributions solved by Eq. (1) and (16) are same before the instability onset. When there is no gravity in  $x$ -direction,  $gx_0 = gx_1 = 0.0$  in buoyancy term (c) and (d). When studying the steady gravity in  $y$ -direction,  $gy_1 = 0.0$  in term (c) and (d), When studying the modulated gravity,  $gy_0 = 1.0$  and  $gy_1 \neq 0.0$ . When there is no background gravity,  $gy_0 = 0.0$ . When viscosity is constant,  $f_v = 1.0$  in term (b) and the whole term (e) is equal to zero. The desired frequency and amplitude of gravity modulation can be implemented flexibly by assigning the desired values to them.

Following the same method in Chan, Yu & Chen (2004), the rate of change of the kinetic energy of the fluid is calculated as well. That is, after the solution of Eq. (13), (14), (15 and (16) is obtained, the substantial derivative of kinetic energy in non-dimensional form is calculated by forming the inner product of the velocity with the momentum equation. For simplicity, here we only consider the cases of constant viscosity and gravity modulation in  $y$ -direction. The substantial derivative of kinetic energy in non-dimensional form is written as:

$$\frac{D}{Dt} \left( \frac{u^2 + v^2}{2} \right) = \underbrace{- \left( u \frac{\partial p}{\partial x} + v \frac{\partial p}{\partial y} \right)}_{\text{(I)}} + \underbrace{(u \nabla^2 u + v \nabla^2 v)}_{\text{(II)}} + \underbrace{v \frac{Ra_T}{Pr} \theta}_{\text{(III)}} - \underbrace{v \frac{Ra_S}{Pr} C}_{\text{(IV)}} \quad (19)$$

in which terms (I), (II), (III) and (IV) are pressure work, shear work, thermal buoyancy work and solutal buoyancy work respectively. With  $u$ ,  $v$ ,  $\theta$ ,  $C$  and  $\nabla p$  at a point in flow field are solved, these work components are calculated straightforwardly and so is the rate of change of the kinetic energy.

### 3.2. Numerical Schemes

The numerical scheme of finite difference method used in Chan, Yu & Chen (2004) is used to solve the non-dimensional equations. That is, the time derivatives are discretized by the central-difference method, the convection terms by Arakawa (1966)'s nine-point method, the diffusion terms by the DuFort-Frankel method (DuFort & Frankel (1953)), and the Poisson equation (13) by a fast Fourier solution technique using the fourth-order-

accurate nine-point finite-difference scheme of Houstis & Papatheodorou (1979) . The boundary vorticity is determined by Thom's rule (Roache 1982). The solute equation (16) is treated the same as the energy equation (15). Eq (19) and the extra terms due to variable viscosity in Eq. (14) are discretized by central-difference approximation. The overall scheme is temporally and spatially second-order accurate. The detailed validation of the code based on this scheme is presented in Chan, Yu & Chen (2004). A supplementary validation has also been conducted against the thermal Rayleigh-Bénard problem. The code predicts a critical  $Ra_T = 1750$  , which is close to the well known critical  $Ra_T = 1708$  . The computations are usually run at  $513(x) \times 65(y)$  grid points and time step  $\Delta t = 0.0001$  with continuous random perturbations of  $5 \times 10^{-6}$  superposed on the flow field unless otherwise noted.

## CHAPTER 4.

## DETERMINATION OF FREQUENCY OF INSTABILITY

Fluid particles oscillate at the instability onset. The frequency of such oscillation is determined by estimating the power spectrum of the time sequence of its vertical component of velocity. In experiments, the time sequence is obtained by analyzing the experimental images using the PIV program. The sequence is usually 5 ~ 10 min long and is sampled every second (see figure 9). Taking the time sequence as a discrete-time signal, we estimate its power spectrum using the Periodogram, the Modified Covariance method and the Burg's method. The Periodogram first estimates the autocorrelation sequence of the signal and then takes the Fourier transform of the autocorrelation sequence to obtain an estimate of the power spectrum. The Modified Covariance method and the Burg's method first select an appropriate model for the signal, then estimate the model parameters from the given signal, and last estimate the power spectrum by incorporating the estimated parameters into the parametric form for the spectrum. The details of the methods can be found in Hayes (1996) and Proakis & Manolakis (1996). The dominant frequency is determined according to the overall behavior of the power spectra from the three estimations (see figure 10). For instance, a frequency is considered as the dominant frequency when at least two of the three methods yield that frequency.

This procedure is applied to time sequences of the vertical velocities at 70 discrete points in the tank (see figure 9), which spanned the range of  $x = (0.25 \sim 0.75)W$

and  $y = 0.25H$  in each experiment, and is applied to all experiments. All determined frequencies from experiments (say,  $70 \times n$  frequencies from  $n$  experiments) are statistically lumped as frequencies vs. the times that they occur. The frequency which appears most times (i.e. the peak on the statistical distribution) is considered as the oscillation frequency ( $f_{onset}$ ) of the instability onset by experiments.

In computations, the time sequences of the vertical component of velocity at different points in the flow field are recorded as well. New signal sequences of equivalent length to experiments are obtained by sampling the time sequences of the velocity with appropriate sampling rate. Then, we analyze the signal sequences using the same procedure to determine the oscillation frequency of instability onset. Due to the fact that the time sequences of the vertical component of velocity at different points are consistently close to each other and so are their power spectra, we just analyze the time sequences at three points located  $(2.75, 0.25)$ ,  $(5.5, 0.25)$  and  $(8.25, 0.25)$  to estimate their frequencies, and a corresponding statistical distribution of the oscillation frequencies in computations is not needed. The frequency estimated from the three time sequences is accepted as the oscillation frequency ( $f_{onset}$ ) of instability onset by computations.

## CHAPTER 5.

### EXPERIMENTAL RESULTS AND DISCUSSION

In this chapter, the unstable motion at onset and their oscillatory frequency will be studied in terms of streaklines, velocities and vorticity contours. The flow field is 10 mm high  $\times$  54 mm wide, which is the middle half domain of the test tank. The exposure time of streakline images is 4 sec unless otherwise noted. The characteristics of instability onset in terms of  $Ra_T$ ,  $Ra_S$ ,  $t_{onset}$ ,  $f_{onset}$  and  $\lambda$  are presented first for the case of steady gravity, and then the features under unsteady gravity. Compared with the steady gravity, the instability onset under the actual gravity modulation occurs earlier and oscillates at higher frequency. The streaklines show that the instability onset under steady gravity consists of two-layer counter-rotating vortices whereas the onset under unsteady gravity is single-layer counter-rotating vortices.

#### 5.1. Steady Gravity

In experiments, the instability onset is determined by the first regular motion detected by flow visualization and the onset of regular oscillation of the vertical component of velocity. For instance, figure 11 shows that the instability onset at  $t_{onset} = 91$  min determined by the regular oscillation of the vertical component of velocity in Experiment H5 in Table 1. A streakline image sequence of  $Ra_T = 161,560$  and

$t_{onset} = 99$  min in Experiment H6 is shown in figure 12 to illustrate the development of the instability onset. The flow is quiescent in image 1. One min later, the first motion of cellular structure is detected in the lower half of the fluid layer in image 2. It is noted that the cellular motion is very weak here as a result of the longer exposure time of images 1 and 2 (6 sec rather than 4 sec). The phenomenon that the first cellular motion is limited in the lower half is explained as follows: we can see from figure 6 that the solute gradient  $dS/dy$  next to the top and bottom boundaries is nearly zero (i.e. almost uniform solute there) but the temperature gradient  $dT/dy$  remains constantly linear. The combination of the two gradients may cause unstable motions next to the boundaries even though the overall density distribution across the fluid layer is still stable. Therefore the instability is generally expected to onset as one row of cells next to the top boundary and the other row of cells next to the bottom boundary. As the temperature of fluid close to the bottom is higher than that close to the top, the viscosity of local fluid near the bottom is consequently smaller, resulting in a higher  $Ra_T$  and thus causing the flow in the lower half to become unstable first. Image 3 shows that more cells of motion appear in the lower half across the tank, and in the meantime the cellular motion also starts emerging in the upper half. Every cell rotates in the opposite sense to all cells around itself (shown in next paragraph). The cells fill up the entire tank quickly, grow in strength, and adjust their orientations in images 3, 4 and 5. All cells are of about same size whereas the ones in the lower half are generally stronger than the ones in the upper half. Taking images 2, 3, 4 and 5 as the critical stage, the instability onset has a two-layer cellular flow pattern

with wavelength  $\lambda = (0.91 \sim 1.09)H$ , which matches the linear stability predictions by Chen (2004). Shirtcliffe (1969) reported in his experiments that the cells are independent and not contiguous. The present streakline images, however, show that the cells are contiguous. Chen (2004) also predicted the contiguity of the cells. In images 6 and 7, some existing cells are still two-layer structured, and grow stronger and larger (hence the  $\lambda$  is larger) (see the right part of images 6 and 7), while some other developed cells are merging into one-layer larger cells because of the solute mixing due to the preceding onset motions (see the left part in images 6 and 7). Images 8, 9 and 10 show the one-layer cellular motions are dominating the fluid layer more and more, and eventually the initial stably stratified fluid layer is mixed and the flow becomes supercritical convections (image 10). The time for the instability to develop is 12 min.

Figure 13 shows the velocity vectors and vorticity contours of images 5 and 7 of figure 12. Red vorticity contours are positive and blue ones are negative. The vorticity contours indicate that, first, the flow patterns are two-layer cells and each layer occupies approximately half the thickness of the fluid layer; second, every cell rotates in the opposite sense to its neighbor cells. These two features can also be observed by playing the movies slowly.

The data of six experiments were collected and summarized in Table 1 for the steady gravity case. From Table 1, the average temperature difference between the top and bottom boundaries is  $\Delta T = 10.16^\circ\text{C}$ , which yields  $Ra_T = 161,560$ . The average onset time is  $t_{onset} = 94.8\text{min}$ . The solute difference  $\Delta S$  at  $t_{onset} = 94.8\text{min}$  is then determined by

solving Eq. (1) and the solved solute difference  $\Delta S$  determines that the average critical solutal Rayleigh number is  $Ra_s = 125,540$ .

The oscillation of onset motion is shown in figure 14 by vorticity contours at six different times spanning 25 sec in total, where the first one corresponds to image 2 in figure 12. Observing the vorticity contours at a fixed coordinate point, it is seen that the vortex changes its sense of rotation continuously, oscillating clockwise and counter-clockwise. The fact that each cell rotates in the opposite sense to its neighbor cells is seen again in this figure.

The oscillatory frequency of the instability onset is determined by the procedure introduced in Chapter 4. Figure 15 shows the evolution of the vertical component of velocity  $v$  at one point in the flow field. It is seen from the figure that, first, the onset motion is being magnified and therefore the flow is becoming unstable, and secondly, the unstable motion is oscillatory as shown in figure 14 and predicted by linear stability analysis. All evolutions of velocities from the six experiments were analyzed by the power spectrum estimations. The dominant frequencies of the instability onset are summarized in figure 16. It is seen that the frequencies fall into a finite band of  $(0.035 \sim 0.051) Hz$ . The statistical distribution of the frequencies is shown in figure 17. The estimated frequencies show a good Gaussian distribution. From the distribution, the oscillatory frequency of the instability onset under the steady gravity is determined as  $f_{onset} = 0.043 Hz$ , which agrees very well with the critical frequency  $f_{onset} = 0.045 Hz$  predicted by Chen (2004).

As shown in Turner (1973), for a double-diffusive fluid layer with linear temperature and solute profiles and dynamic free boundaries, linear stability analysis predicts the angular oscillatory frequency of the most unstable instability mode is

$$\left[ \frac{1 - 1/Le}{3(Pr+1)} \right]^{1/2} N \quad (20)$$

where the buoyancy frequency  $N$  is

$$N = \left( - \frac{g}{\rho^*} \frac{\partial \rho^*}{\partial y^*} \right)^{1/2} \quad (21)$$

Using the values of the present experimental conditions, the predicted frequency of the instability onset is  $f_{predict} = 0.2722 rad/s = 0.0433 Hz$ , essentially the same as the  $f_{onset}$  obtained from experiments.

## 5.2. Gravity Modulation

The effects of gravity modulation on the instability onset were investigated at the modulation frequency of  $1.0 Hz$  and the modulation amplitude of an additional acceleration of  $0.403g$  ( $g = 9.807 m/s^2$  is the constant background gravity). Among the seven experiments conducted, the streaklines of the onset motion from two of them show the similar two-layer cellular flow structure of the steady gravity case but now they evolve into the supercritical state in a shorter time compared with the steady gravity case. The streakline images from the other five experiments show the onset motion under the

unsteady gravity possess different characteristics, which are illustrated by the streakline images in Experiment H8 (see Table 2) in figure 18. The flow is quiescent in image 1. The first unstable motion appears as a single big cell spanning the entire height of the tank in the right part of image 2. The second cell forms right next to the first one in image 3. All cellular motions are very slow so far. In image 4, another pair of cells emerges in the left part of the image. The cellular motions then fill up the entire tank in image 5, merge and orient their positions into five cells in image 6. The cells are now one-layer structured and fill up the entire height of the tank. Vorticity contours in figure 19 show that each pair of cells rotates in an opposite sense and changes their sense of rotation continuously. Therefore, the instability onset is oscillatory but one-layer cellular pattern. The wavelength varies in a wider range of  $\lambda = (1.39 \sim 2.26)H$ . From images 7 through 9, in the right part of the images, the previous slow motions are becoming strong convections; in the middle part, most of the one-layer cells still persist; and in the left part, cells keep the breaking-merging process. In image 10, the strong convective motions dominate the most part of the fluid layer. The fluid layer is mixed and the flow is completely unstable from then on. The time for the instability to develop is 10 min, 2 min less than the steady gravity case.

The experimental data of the seven experiments are summarized in Table 2. Similar to the steady gravity case, the temperature difference remains constant as  $\Delta T = 10.15^\circ\text{C}$  and  $Ra_T = 161,330$ . The average onset time is  $t_{onset} = 85.7$  min and the critical  $Ra_S = 136,140$ , which are 9.6% decrease and 8.4% increase from the steady

gravity case respectively. The higher critical  $Ra_S$ , the shorter onset time  $t_{onset}$  and the one-layer cellular structure are the consequences of the gravity modulation.

The vorticity contours in figure 19, where first one corresponds to image 5 in figure 18, confirm the fact that the vortices fill up the whole thickness of the fluid layer and rotate oppositely to the neighbor vortices. The contours also demonstrate that the cells keep changing the sense of rotation (oscillatory) when fixing our observation at a point.

Figure 20 is the evolution of the vertical component of velocity  $v$  at a point in flow field at the instability onset. Compared with that of steady gravity, the onset motion now oscillates faster with larger amplitude. The procedure introduced in Chapter 4 is used again to determine the oscillation frequency. The statistical distribution of the dominant frequencies of the seven experiments is shown in figure 21. The frequency spectrum is much broader than steady gravity case but still shows a fairly good Gaussian distribution. From the distribution, it is determined that the oscillatory frequency of the instability onset under the gravity modulation is  $f_{onset} = 0.057Hz$ , 32.6% increase from the steady gravity case. Compared with the steady gravity case, the present distribution is much broader with a lower peak. These differences can also be attributed to the effects of the gravity modulation.

The parameters at the instability onset determined by experiments and linear theory are summarized in Table 3 to compare the effects of the gravity modulation on the instability onset. All the dimensional parameters are converted into non-dimensional form so that it will convenient to compare with the simulated results that will be

presented in next chapter (characteristic time is 100.0 sec). Briefly summarizing, the gravity modulation of 1.0Hz frequency and 0.403g amplitude slightly destabilizes the fluid layer than the steady gravity. The destability effects are demonstrated by the shorter onset time  $t_{onset}$  (-9.6%), the greater critical  $Ra_s$  (+8.4%) and a much higher oscillatory frequency  $f_{onset}$  (+32.6%). In addition, the onset motions under the gravity modulation have a larger wavelength  $\lambda$  compared with the steady gravity.

## CHAPTER 6.

## NUMERICAL SIMULATIONS OF EXPERIMENTS

The two-dimensional numerical simulations have been carried out to study the problem as well. The experimental condition and procedure are simulated closely by setting the parameters  $Pr = 7.0$ ,  $Le = 118.3$ ,  $Ra_T = 161,560$ , initial  $Ra_S = 238,830$  and a sinusoidal gravity modulation, and then looking for the instability onset and determining the critical  $Ra_S$ ,  $t_{onset}$ ,  $f_{onset}$  and  $\lambda$ . The onset motions and frequencies will be discussed in terms of streamline, velocity, vorticity contour and the same power spectrum estimation. From now on, all parameters are discussed in non-dimensional form. The characteristic time that converts the time between dimensional and non-dimensional forms is 100.0 sec. For the steady gravity case, the features observed in the experiments are replicated in the simulations. For the gravity modulation case, the observed phenomena in experiments are not able to be reproduced under ideal sinusoidal gravity modulation. However, by combining possible causes into it, computations indicate the similar trend of experiments that gravity modulation affects the fluid layer slightly.

## 6.1. Steady Gravity

In computations, the instability onset is determined by the first appearance of streamline contour in the flow field and the first regular oscillation of stream function  $\psi$ .

Figure 22 shows the time history of an absolute value of stream function  $|\psi|$  under steady gravity with  $gx_1 = -0.01$ . From the figure, we see that the instability onset at  $t_{onset} = 57.0$  determined by appearance of first streamline contour is confirmed by the oscillation of  $|\psi|$  from that time. The evolution of instability onset of this case is shown in figure 23. The time interval is  $t = 0.6$  except image 9 which is  $t = 1.8$  after image 8. Image 1 is the first image in which the streamline contours are detected. Here the scale of the contour is  $\Delta\psi = (-0.1 \sim 0.1)/18$ , approximately 2000 times greater than the random noise in the flow field. The convection cells show up first in the lower half of the flow field due to the smaller local viscosity discussed in section 5.1. In image 2, following the cells in the lower half, new cells also appear in the upper half. The cells in two halves then develop transversely over the entire flow field, and grow stronger in images 3, 4 and 5. The two-layer vortices observed in experiments are replicated. Again, the neighboring cells are in counter-rotating each other. The wavelength based on contours in images 3, 4 and 5 is  $\lambda = (0.82 \sim 1.00)H$ , which agrees with the  $\lambda = (0.91 \sim 1.09)H$  obtained from the experiments. The scales of streamline contour indicate that the onset motions are very weak so far. The cells grow up quickly from image 5. The two-layer vortices start breaking down from the right end of the flow field in image 6. In image 7, while the two-layer cellular motions exist in the middle region, the larger and stronger single cellular motions start dominating the flow field. Following image 7, the entire field is filled up with strong convection cells shown in image 8. Image 9 shows a streamline pattern of the well-mixed fluid flow (1.8 non-dimensional time after image 8), which is the well-known

Rayleigh-Bérnard pure thermal convection. The time for the instability to develop is 5.4, 1.8 shorter than the experiments.

The solute profile (see figure 6) provides a clear view to explain the development of the instability onset. Due to the non-diffusive conditions on the top and bottom boundaries, the solute gradient is smaller when approaching to both boundaries but larger when toward the mid region of the layer. Therefore, with the constant temperature gradient across the layer, the flow regions next to the two boundaries become unstable first, and so the onset cells emerge first there and organize as the two-layer vortices. The two-layer vortices exist for certain time because the largest solute gradient at the mid region behaves a kind of separation between them. Then, they merge into the bigger single-layer vortices due to the mixing effect of the two-layer motions. And the fluid flow becomes supercritical eventually.

With the given  $Ra_T = 161,560$ , the computations determined that the critical  $Ra_S = 122,560$  and  $t_{onset} = 58.2$ , which are only 2.3% off the experimental values. The oscillatory feature of the instability, shown by streakline and velocity  $v$  in the experiments, are now shown by the streamlines in figure 23 and the evolution of the vertical component of velocity  $v$  in figure 24. The procedure described in Chapter 4 is used to estimate the power spectra of the velocity evolutions at points (2.75, 0.25), (5.5, 0.25) and (8.25, 0.25). The three time sequences of the vertical component of velocity yield a frequency distribution of (25.76 ~ 30.66) with a peak value of 28.27. Since the distribution is narrow and the peak value is so dominant, the oscillation frequency of the

instability onset is determined as  $f_{onset} = 28.27$  , which agrees well with the experimental  $f_{onset} = 27.02$  , and the statistical distribution of oscillation frequencies which was presented in experiments is not needed. The parameters at the instability onset are summarized in Table 4.

The experimental movies show that there are very slow creeping motions in the horizontal direction after the temperature difference is imposed in the experiments (see figure 25(a)), even it is well before the instability onset. There may be several possible causes for this phenomenon. The most likely one is the slight misalignment of the platform and therefore a small gravity component in the horizontal direction comes into the flow field. The small horizontal gravity and the big temperature difference in the vertical direction ( $\Delta T = 10.16^\circ\text{C}$  in the experiments) may work together to induce the creeping natural convection. Setting the horizontal gravity  $gx_0 = -0.01$  , a similar horizontal convection is seen in computations (see figure 25(b)). With this correction, the computations determined that the instability onset under the steady gravity is at  $Ra_S = 124,030$  ,  $f_{onset} = 28.27$  and  $t_{onset} = 57.0$  , which improved the agreement with the experimental results (see Tables 3 and 4). The horizontal convection in figure 25(b) consists of two elongated cells. The cellular motion makes the fluid layer more mixed within the upper and lower halves but more stratified between the two halves. The former causes the local flow is less stable and the instability show up earlier. The latter extends the existence of the two-layer cellular patterns.

## 6.2. Ideal Gravity Modulation

In simulations, the gravity modulation is simulated by a sinusoid of given frequency and amplitude. Other conditions and the procedure are kept the same as the steady gravity case. Initially, the gravity modulation is simulated by an ideal sinusoid with the frequency  $\omega_m = 628.3$ , the amplitude  $gy_1 = 0.403$  and the background gravity  $gy_0 = 1.0$ , and it is further assumed that  $gx_0 = gx_1 = 0.0$ . The results show that there is no discernible difference in terms of  $t_{onset}$ ,  $f_{onset}$  and  $Ra_S$  (see Table 4), and the flow pattern still consists of two-layer vortices at the instability onset. That is to say, the gravity modulation does not affect the instability in simulations. While this conclusion contradicts to the experimental results presented in section 5.2, the simulated results agree with the linear theory prediction by Chen (2001) (see his figure 6.19). The results seem also consistent with the linear theory prediction by Sounders et al (1992) (see their figure 7) if the discrepancy of parameters ( $Pr$ ,  $Ra_T$  and  $Ra_S$ ) is neglected. Both of them predicted that under the gravity modulation of the amplitude and frequency adopted in the experiments there is no resonance.

## 6.3. Actual Gravity Modulation

It was noticed that the ideal gravity modulation is different from the actual modulation to certain extent. The measured acceleration of the platform shown in figure 26 exhibits an asymmetry due to the mechanical gearing in the Scotch-Yoke mechanism. It is certain that a larger gravity will affect the double-diffusive convection more. For

instance, with the steady gravity  $gy_0$  increased up to 1.50 in computations, the time of onset is shortened to  $t_{onset} = 55.0$ . Within a cycle of the actual acceleration, the duration of gravity larger than 1.0 is longer than the duration of gravity smaller than 1.0. The accumulation of the net difference within every cycle may affect the instability. The ideal gravity ( $gy_0 + gy_1 \cos(\omega_m t)$ ) in the momentum equation (14) is now replaced by the actual gravity by inputting the measured discrete acceleration into the computations. Other parameters and conditions remain unchanged. The simulated critical  $Ra_S(+0.16\%)$ ,  $t_{onset}(-4.12\%)$  and  $f_{onset}(+8.45\%)$  are slightly different from those of the steady gravity case (see Table 4). The small differences are not random numerical errors because they exist under different numerical conditions in simulations (for instance, different order of perturbations, different discretization of the actual gravity). Since the gravity modulation in the vertical direction is the only factor changed from the ideal situation, the consistent differences may be attributed to the effects of the actual asymmetry of the gravity modulation.

When combining the actual measured vertical gravity and the horizontal gravity component into the simulations, the instability onset is at  $Ra_S = 125,750$ ,  $f_{onset} = 31.92$  and  $t_{onset} = 54.0$ , which are closer to the experimental values.

It is noted, however, the flow is still the two-layer structure so far and thus the wavelength does not change essentially. The single-layer structure observed in the experiments has not been observed in the simulations. It is also noted that the simulations show that the possible modulation of horizontal gravity does not affect the instability

onset perceivably, even though it is included in computations. Table 4 summarizes the related results discussed in Sections 6.1, 6.2 and 6.3.

## CHAPTER 7.

### KINETIC ENERGY CONSIDERATION

The rate of change of the fluid kinetic energy of the double-diffusive convection is considered in this chapter. The roles that pressure, shear stress, thermal buoyancy and solutal buoyancy play before, at and after the instability onset are shown by their respective mechanical work contributions in Eq. (19). When the gravity is steady, the total kinetic energy and mechanical work components oscillate synchronously with the unstable motions at the instability onset and vary randomly before or after the instability onset. When the gravity is modulated, the oscillations of the total kinetic energy and mechanical work components depend on the modulation frequency of gravity. At high modulation frequencies, the total energy and work components oscillate not only synchronously with the instability onset in global view but also synchronously with the modulation frequency in local view, and they only oscillate synchronously with the modulation frequency after the instability onset. At low modulation frequencies, the total kinetic energy and work components oscillate only synchronously with the modulation frequency throughout the instability onset.

#### 7.1. Steady Gravity

The consideration of kinetic energy is helpful to understand the physical mechanisms of the double-diffusive convection during the instability onset. Figure 27 shows the time

rate of change of the total kinetic energy and work components contributed by pressure, shear stress, thermal buoyancy and solutal buoyancy during the instability onset as computed by Eq. (19). Here the “total” means that the sum of the energy and work components at every point in the flow field at a certain time. As expected, both the energy and work components are zero before the instability onset (at  $t_{onset} = 58.2$ ) as the fluid layer is quiescent. Even shortly after the onset, they are still negligibly small due to the weakness of the motions at the onset and compared with their subsequent magnitudes. Then the thermal buoyancy work, which drives the convective motions, quickly climbs up to a certain level and remains that level from then on. The work by shear stress, which dissipates the convections, reaches a similar but opposite level and keeps steady as well. The thermal buoyancy work and shear work essentially cancel each other. The solutal buoyancy work, which stabilizes or destabilizes the flow depending on whether heavier fluid is near the bottom or the top boundaries, is only significant before the fluid is well mixed. As the fluid is mixed more and more, the solute gradient is smaller and smaller and so is the solutal buoyancy work. After completely mixed, there is no solute difference any more and the solutal buoyancy work vanishes from then on. The pressure work is negligibly small compared with other terms and does not fluctuate as much as other work components. The time rate of change of the total kinetic energy oscillates as the flow becomes unstable while its magnitude basically remains an unchanged level throughout the onset stage.

Doing power spectrum estimations to the total energy and work components around the instability onset, it is found that their oscillation frequencies are either at the

frequency of instability onset ( $f_{onset} = 28.27$ ), or at twice the value. Specifically, the time rate of change of the total kinetic energy and shear work oscillate at frequency  $f = 56.54$ , pressure work at  $f = 27.65$ , thermal work and solutal work first at  $f = 27.65$  shortly and then at  $f = 56.54$ . Figure 28 shows these oscillations. From the figure, it is seen that the thermal and solutal works oscillate at  $f = 27.65$  within time duration of  $t = (58.2 \sim 58.8)$  and then at  $f = 56.54$  within  $t = (58.8 \sim 59.4)$ . After the instability onset, all the total energy and work components fluctuate randomly.

The distributions of the mechanical work components in the fluid layer along the horizontal direction, that is, the work components are summed up in the vertical direction at a certain  $x$ -position at a certain time, also shed instructive information to understand the double-diffusive convection. Figure 29 shows the distributions before, at and after the instability onset, where (b) and (c) correspond to the streamline image 5 and 9 in figure 23. Figure 29(a) is at a sub-critical state. It is seen that before the instability onset, thermal buoyancy work and solutal buoyancy work are dominant and basically counteract each other. The pressure work is negligibly small. The shear work is zero as a result of motionlessness of the flow field. Figure 29 (b) shows the distributions of work components at the instability onset. While the thermal and solutal buoyancy work components are still dominant and cancel each other, the small shear work indicates that there are motions yet the motions are weak, which is what streamlines show in image 5 of figure 23. Figure 29(c) shows the distributions of the work components at a completely supercritical state consisting of a row of rotating motions. Now rather than the solutal

buoyancy work which disappears as a result of well mixing, the shear work due to the convective motions counteracts the thermal buoyancy work. The peaks on the curve of the thermal buoyancy work and the valleys on that of shear work represent the faster motions between every two cells, and the bumps on the curve of the pressure work indicate the slower motions in the cores of cell. In addition, figure 29(c) confirms what was discussed in figure 27: the total thermal buoyancy work is dominantly positive while the total shear work is dominantly negative. They cancel each other. Due to the cancellation between its positive and negative parts in figure 29, the total pressure work is negligibly small in figure 27.

## 7.2. Gravity Modulation of High Frequency

Figure 30 shows the total kinetic energy and work components under the ideal gravity modulation of frequency  $\omega_m = 628.3$  and amplitude  $gy_1 = 0.403$ . The total kinetic energy and pressure work, which do not oscillate much under steady gravity, oscillate significantly now due to the gravity modulation. The total work components by shear force, thermal buoyancy and solutal buoyancy keep the similar oscillations as they do under steady gravity. Power spectrum estimations indicate that all of them oscillate globally and/or locally as shown in figure 31. Note: the kinetic energy is partially covered by the pressure work in figure. Figure 31(a) shows the oscillations at the instability onset. On the one hand, the kinetic energy, pressure work and shear work globally oscillate at frequency  $f = 56.54$ ; thermal and solutal buoyancy work first at  $f = 27.65$  (see their

envelopes change within  $t = (58.2 \sim 58.8)$  shortly and then at  $f = 56.54$  (see their envelopes change within  $t = (58.8 \sim 59.4)$ ), which are the same behavior as they vary in the steady gravity case except there pressure work varies at  $f = 27.65$ . On the other hand, all the energy and work components locally oscillate at frequency  $f = 622.6$ , which is essentially the modulation frequency  $\omega_m$ . Both the global and local oscillations are clear at the instability onset. Figure 31(b) shows the oscillations after the instability onset. All the energy and work components now oscillate solely at the local frequency  $f = 622.6$  except the solutal buoyancy work, which is zero now.

### 7.3. Gravity Modulation of Low Frequency

Besides  $\omega_m = 628.3$ , the oscillations of the total energy and work components are also investigated under different modulation frequencies, specifically  $\omega_m = 1.10, 1.05, 0.95, 0.90, 0.75, 0.50, 0.25$  and  $0.125$  of  $628.3$ . It is found that their oscillations are related to the modulation frequencies as well. When the modulation frequency  $\omega_m$  is high, the total kinetic energy and work components oscillate at both local and global frequencies at the instability onset and oscillate only at local frequencies after the instability onset, which is discussed with  $\omega_m = 628.3$  in last paragraph. When the modulation frequency  $\omega_m$  is low, the total kinetic energy and work components oscillate only at its local frequency (i.e. modulation frequency  $\omega_m$ ) throughout the instability. Figure 32 shows such oscillations at modulation frequency  $\omega_m = 78.5$ . In a word, the gravity modulation affects the total

kinetic energy and mechanical work components to oscillate synchronously throughout all the modulation frequencies.

The horizontal distributions of the mechanical work components are also computed for the unsteady gravity case. They are essentially the same as that under steady gravity, which was already discussed and shown in figure 29.

## CHAPTER 8.

## FURTHER COMPUTATIONAL INVESTIGATIONS

In this chapter, several computational investigations of gravity modulation that may not be studied easily by experiments have been carried out. First, the resonance phenomenon under micro-gravity conditions predicted by Chen (2001) using linear stability theory is confirmed. Such resonance also exists under the present lab conditions and the destability effect due to the resonance increases as the modulation amplitude increases. As Gresho & Sani (1970) showed that a stably stratified fluid layer can become unstable under gravity modulation when the amplitude of the modulation is large enough, this phenomenon is encountered in the present study of the resonance conditions. Such mode of instability is found to occur before the double-diffusive instability in the case studied by Chen (2001) and in the present lab conditions. This instability in the statically stable fluid layer, subsequently referred to as the “density-mode instability”, is in the sub-harmonic mode at higher modulation frequencies and is in the synchronous mode at low modulation frequencies and higher modulation amplitude, as predicted by Gresho & Sani (1970). The motions generated by the density-mode instability definitely promote the mixing of the solute across the fluid layer and thus affecting the succeeding double-diffusive instability. Lastly, the effects of purely modulated gravity, i.e. without any constant background gravity, have been investigated in some selected cases. Compared with the gravity modulation with the background gravity, the pure gravity modulation destabilizes the fluid layer rapidly at low modulation frequencies and the accompanying

unstable motions are chaotic or sub-harmonic. On the contrary, it stabilizes the fluid layer at high modulation frequencies and the delayed instability onset is in the synchronous mode.

### 8.1. Resonance Phenomenon

As introduced in Chapter 1, Chen (2001) investigated the effects of gravity modulation on the instability of a horizontal double-diffusive layer under micro-gravity conditions using linear stability theory. The basic flow within the infinitely long horizontal fluid layer is at stationary state with fixed linear temperature and solute differences across the layer. Given the parameters  $Pr = 7.0$ ,  $Le = 100.0$ ,  $Ra_S = 3200$ ,  $gy_0 = 1.0$  and  $gy_1 = 0.40$ , he found an instability resonance region centered at the critical  $\omega_m = 54.26$ . At the critical frequency of the modulation, the critical  $Ra_T$  decreases from 4,758 (which is the critical  $Ra_T$  under the steady gravity) to 4,214, a drop of 11.4%. The oscillatory instability onset is in the sub-harmonic mode, i.e.  $f_{onset} = 27.13 = \omega_m/2$ . Adopting the same parameters and the procedure, the resonance phenomenon has been investigated for a linearly stratified fluid in a finite horizontal tank of aspect ratio  $A = 10$  using the direct simulation. In computations, the grid points are 257 (in x-direction)  $\times$  33 (in y-direction); the time step is  $\Delta t = 0.0001$ ; random perturbations not more than  $5 \times 10^{-4}$  are superposed on the basic flow at every time step. The critical  $Ra_T$  for a given  $Ra_S$  is determined by try-and-error method: set a  $Ra_T$  and compute the transient flow up to

time  $t = 250$ ; the state is considered as supercritical (sub-critical) if onset motions are (are not) detected when  $t \leq 250$ ; then set a smaller (larger)  $Ra_T$  and repeat this procedure till a critical  $Ra_T$  is determined.

Figure 33 shows the computed instability map. Here all frequencies in Chen (2001)'s study are converted into the present non-dimensionalization system by dividing them by 7.0. The blue curve represents the double-diffusive instability predicted by Chen (2001). The green curve represents the density-mode instability, which will be discussed in detail in section 8.3. It is seen that the resonance phenomenon predicted by Chen (2001) is obtained by the nonlinear simulation as well. The resonance is within the modulation frequencies of 3.0 to 12.0 with the critical  $\omega_m = 7.50$ , which agrees with  $\omega_m = 7.75$  found by Chen (2001). At  $\omega_m = 7.50$ , the critical  $Ra_T$  decreases from 4,937.5 (under the steady gravity) to 4,330.0, which is a decrease of 12.3% and compares well with the decrease of 11.4% reported by Chen (2001). The reason for the upward shift of the instability curve from Chen (2001)'s map (between 4,214 and 4,758) to the present map (between 4,330.0 and 4,937.5) may be attributed to the finite horizontal tank and finite time of the present computations. The power spectrum estimations determine that the oscillation frequencies of the instability onset are  $f_{onset} = 3.84$  under both the steady gravity and the resonant gravity modulation ( $\omega_m = 7.50$ ), consistent with  $f_{onset} = 3.88$  predicted by Chen (2001). Thus, the instability onset is in the sub-harmonic mode. The streamline patterns of the onset motions are similar to that of Rayleigh-Bénard problem, i.e. every streamline contour fills up the entire thickness of the fluid layer with opposite rotating sense to the

cells next to it, except the cellular convections here alternate their sense of rotation senses continuously. The dominant wavelength of the oscillatory motions is  $\lambda = 2.0$ .

The thus-far-discussion is restricted to the double-diffusive instability represented by blue curve *abcdefgh* in figure 33. Besides it, it is found that there is an additional unstable region under the micro-gravity conditions enclosed by green curve *dgf* and blue curve *def*, within which the instability is in the density-mode. When  $Ra_T$  is below the curve *dgf* for a given modulation frequency, the fluid layer is absolutely stable. When  $Ra_T$  is between the curves *dgf* and *def*, the fluid layer is unstable only in the density-mode. While it takes long time for the unstable motions to develop and grow in the double-diffusive instability, the unstable motions of the density-mode instability occur shortly after computations start and develop quickly into a series of strong convective cells. The developed cells then exist in the flow field for certain time, become weaker compared with their early stages, and fade away eventually. The fluid layer restores stably motionless again. When  $Ra_T$  is above the curve *def* for a given modulation frequency, the fluid layer experiences the density-mode instability first and then evolve into the double-diffusive instability. The unstable motions for this case do not decay after their birth and exist there forever. The power spectrum estimations show that the density-mode instability onset is oscillatory and the dominant frequency is  $f_{onset} = (4.60 \sim 5.52)$ . The convective cells are single-layer structured and the wavelength is  $\lambda = (1.33 \sim 1.67)H$ . When the modulation frequency  $\omega_m$  is beyond the frequency range of the density-mode instability, there is no density-mode instability in the fluid layer.

## 8.2. Resonance Phenomenon Under Different Conditions

Do the resonance phenomenon and the density-mode instability also exist under the terrestrial condition? The question is answered by carrying out the computational investigations under the present lab conditions (i.e.  $Pr = 7.0$ ,  $Le = 118.3$ ,  $Ra_T = 161,560$ , initial  $Ra_S = 238,830$  and  $gy_0 = 1.0$ ) with four modulation amplitudes at 0.40, 0.50, 0.75 and 1.00. Since now the solute distribution is not a fixed linear profile but a sinusoidal profile (see figure 6) with the solute difference across the layer decreasing due to non-diffusive boundary conditions, the onset time  $t_{onset}$  is used as the parameter to indicate the resonance phenomenon. When  $t_{onset}$  under gravity modulation is shorter than  $t_{onset}$  under steady gravity, there is resonance effect in the flow due to gravity modulation. And a shorter  $t_{onset}$  means a larger resonance.

Figure 34 shows  $t_{onset}$  at different  $\omega_m$  with the four modulation amplitudes. It is seen that the resonance phenomenon also exists on the earth. When the modulation frequency  $\omega = 0.0$ , i.e, the steady gravity, the onset time  $t_{onset} = 58.2$ ; When the  $\omega_m$  increases but less than 60.0, the  $t_{onset}$  decreases and thus the resonance effect increases; When  $\omega_m = (60.0 \sim 80.0)$ , the  $t_{onset}$  is the shortest and thus the resonance phenomenon reaches its critical state; When the  $\omega_m$  increases from 80.0 but less than 120.0, the  $t_{onset}$  increases and the resonance effect becomes less; When the  $\omega_m > 120.0$ , the  $t_{onset}$  restores its corresponding value of steady gravity and the resonance effect disappears (the

different behavior of the  $t_{onset}$  of  $gy_1 = 1.0$  will be discussed in section 8.3). The critical modulation frequency of the resonance phenomenon is  $\omega_m = (60.0 \sim 80.0)$ . The power spectrum estimations determine that the critical oscillation frequency of the instability onset  $f_{onset} = 31.91, 35.59$  and  $38.04$  when the modulation frequency  $\omega_m = 63.6, 70.6$  and  $77.7$  respectively regardless of the variation of the modulation amplitude. The instability onset, thus, is in the sub-harmonic mode. The development of the unstable motions is similar to those shown in figure 23 and discussed in section 6.1. The wavelengths of the onset motions are  $\lambda = (1.00 \sim 0.96), (0.92 \sim 0.81)$  and  $(0.79 \sim 0.73)$  when the modulation frequency  $\omega_m = 63.6, 70.6$  and  $77.7$ , insensitive to the change of the modulation amplitude.

Contrary to the oscillation frequency and wavelength, which are insensitive to the variation of the modulation amplitude, the onset time  $t_{onset}$  decreases with the increase of the modulation amplitude  $gy_1$ . For  $\omega_m = 70.6$ ,  $t_{onset}$  decreases from 51.0 when  $gy_1 = 0.40$  to 38.0 when  $gy_1 = 1.00$ , a decrease of 25.5% of the onset time. Therefore, the resonance phenomenon increases as the modulation amplitude increases.

### 8.3. Density-Mode Instability

The density-mode instability first introduced in section 8.1 also exists under the present lab conditions. This section is dedicated to the detailed study of this phenomenon. It is found that the density-mode instability exists in certain combinations of modulation

frequency and amplitude under either double- or single-diffusive conditions. Under double-diffusive conditions, the density-mode instability onsets before the double-diffusive instability onsets. The density-mode instability is due to the density gradient of the fluid layer that is sensitive to certain modulation frequencies and amplitudes. When the modulation frequency is low and the modulation amplitude is large, the instability is in the synchronous mode. When the frequency is high and the amplitude is small, the instability is in the sub-harmonic mode, which usually is the case. The unstable motions of the instability are one-layer cellular strong convections. The convections promote the mixing of the solute gradients, thus causing the succeeding double-diffusive instability to onset earlier.

### 8.3.1. Interaction of Density-Mode and Double-Diffusive Instabilities

The interaction of the density-mode instability and the double-diffusive instability is illustrated by a study of the  $gy_1 = 0.75$  case and the results are shown in figure 35. In figure 35 (a), the red-circle-connected curve is the onset time  $t_{onset}$  of the double-diffusive instability at different modulation frequencies  $\omega_m$ . The fluid layer is stable when time is shorter than  $t_{onset}$  and unstable when time is longer than  $t_{onset}$ . It is seen that there are two minima on the instability curve. The deeper one near the left is the resonance phenomenon at low modulation frequencies ( $0.0 < \omega_m \leq 120.0$ ) discussed in section 8.2 (see figure 34). The shallower one at higher frequencies ( $183.6 \leq \omega_m \leq 296.6$ ) is caused by the density-mode instability, which occurs at an earlier time. Because the mixing

caused by the density-mode instability, the fluid layer becomes less stable. The features of the double-diffusive instability within the two minima, such as  $f_{onset}$ , flow pattern and wavelength  $\lambda$ , do not display obvious difference from those of steady gravity. When the modulation frequency is beyond the two minima, there is no effect of the gravity modulation on the fluid layer.

The density-mode instability is the closed region surrounded by the blue-dot-connected curve in figure 35(a), which is approximately specified by  $0.0 \leq t \leq 30.0$  and  $180.0 \leq \omega_m \leq 300.0$ . When the gravity modulation has a frequency  $183.6 \leq \omega_m \leq 296.6$ , the fluid layer becomes unstable in the density-mode and evolves into convective motion. As time goes on, the convective mixing and the diffusion in the fluid layer reduce the density gradient and thus the fluid layer is motionless once again. Certain time later, the stable fluid layer experiences the double-diffusive instability.

The density-mode instability can also exist in a stable single-diffusive layer (setup by letting  $Ra_T = 0.0$  and keeping  $Ra_S$  unchanged) as shown in figure 35 (b). The unstable region for this case expands into a wider frequency range of  $211.9 \leq \omega_m \leq 430.8$  and longer unstable time up to  $t = 76.0$ .

### 8.3.2. Density-Mode Instability

The unstable convective motion is studied by the streamlines at  $\omega_m = 240.1$ ,  $gy_1 = 0.75$  and  $Ra_T = 161,560$  shown in figure 36. Rather than the two-layer cellular

pattern in the double-diffusive instability, the unstable motion has a one-layer cellular pattern throughout its growing and decaying stages. The scales of stream function indicated in the caption show that the initial double-diffusion rapidly develops into strong convection once the fluid layer becomes unstable (see image 1, 2 and 3). The developed convective motion is maintained for certain time (see image 3, 4 and 5), then decays gradually (see image 5, 6, 7 and 8), and dies out eventually (see image 8 and 9). The fluid layer becomes a stable layer again of smaller solute gradient across it. The evolution of the vertical component of velocity  $v$  at point (5.5, 0.25) in the flow field shown in figure 37 confirms this procedure. In addition, figure 37 indicates the unstable motion is oscillatory. The oscillatory frequencies of the instability determined by the power spectral estimations are summarized in Table 5. It is seen that the density-mode instability is in the sub-harmonic mode. The wavelength of the oscillatory motion decreases throughout the unstable process, with  $\lambda_{\max} = 1.69$  at the beginning and  $\lambda_{\min} = 1.10$  in the end.

When there is no temperature difference across the fluid layer, i.e. the pure solutal diffusion ( $Ra_T = 0$ ), the unstable motion is still one-layer cellular convection and the process for them to grow and decay is similar to that of  $Ra_T = 161,560$ . The oscillation of the unstable motion is still sub-harmonic but with a wider range of wavelength with  $\lambda_{\max} = 2.75$  initially and  $\lambda_{\min} = 1.00$  lastly.

### 8.3.3. Effect of Density-Mode Instability

Since the magnitude of velocity  $v$  in figure 37 is significant, it is suspected whether the unstable motion affects the solute difference across the fluid layer. The positive answer is provided by plotting the solute differences at different modulation frequencies but at same time. Figure 38 shows the solute difference  $|C_t - C_b|$  at  $t = 50.0$  with  $Ra_T = 161,560$  and  $Ra_T = 0$ . When there is no unstable convection, i.e. the modulation frequency  $\omega_m \leq 183.6$  or  $\omega_m \geq 289.6$  under  $Ra_T = 161,560$  and modulation frequency  $\omega_m \leq 211.9$  or  $\omega_m \geq 430.8$  under  $Ra_T = 0$ ,  $|C_t - C_b| = 0.5309$ , which is only due to the diffusion. When the fluid layer experiences the density-mode instability at  $183.6 < \omega_m < 289.6$  under double-diffusive condition and at  $211.9 < \omega_m < 430.8$  under single-diffusive condition, the solute difference is reduced due to both the unstable convection and the diffusion. The critical decrease of the solute difference due to the density-mode instability is at  $\omega_m = 212.0$  under double-diffusive condition and at  $\omega_m = 254.25$  under single-diffusive, at which the solute difference is decreased to  $|C_t - C_b| = 0.5061$ , 4.7% drop and  $|C_t - C_b| = 0.4249$ , 20.0% drop respectively.

The decrease of the solute difference across the fluid layer due to the density-mode instability can also be seen on the non-dimensional solute profiles shown in Figure 39. The solute profiles at  $\omega_m = 169.5$  and  $282.5$  with  $Ra_T = 0$  are the solute distributions at  $t = 36.0$ , which is the time right after the density-mode instability is over in the fluid layer when  $\omega_m = 282.5$ . At  $\omega_m = 169.5$ , the solute difference is larger because the fluid layer does not experience the density-mode instability at all (see figure 35 (b)) and the

solute difference decreases only due to diffusion. At  $\omega_m = 282.5$ , the solute difference is smaller because the fluid layer experiences the density-mode instability (see figure 35 (b)) and the solute difference decreases due to both convection and diffusion.

#### 8.3.4. Cause of Density-Mode Instability

Although the unstable time that the density-mode instability exists and the decrease of the solute difference due to the density-mode instability look like so different for a same  $\omega_m$  with  $Ra_T = 161,560$  and  $Ra_T = 0$  ( for instance, at  $\omega_m = 240.1$ , the unstable time (in figure 35 (a), (b) and the decrease of the solute difference (in figure 38) are 9.0 and 3.7% with  $Ra_T = 161,560$ , and 50.0 and 17.3% with  $Ra_T = 0$ ), the density-mode instabilities under  $Ra_T = 161,560$  and  $Ra_T = 0$  cases can be understood similarly as the effect of gravity modulation on the net density gradient across the fluid layer. The net density profile across the fluid layer can be calculated as

$$\frac{\rho}{\rho_0} = 1.0 - \beta_T (T^* - T_0) - \beta_S (S^* - S_0) \quad (22)$$

where  $\beta_T$  and  $\beta_S$  are thermal and solutal expansion coefficients,  $\rho_0$ ,  $T_0$  and  $S_0$  the related parameters at reference state,  $T^*$  and  $S^*$  the dimensional temperature and solute, respectively. Figure 40 (a) shows the density profiles right after their density-mode instabilities are over at  $\omega_m = 240.1$ . It is seen that the net density distributions right after the density-mode instability are essentially same in the mid region for both

$Ra_T = 161,560$  and  $Ra_T = 0$  cases, even though their temperature and solute distributions are obviously different from each other. In other words, whether the density-mode instability disappears only depends on if the net density gradient is below a certain value and is regardless of the single- or double diffusion. When  $Ra_T = 161,560$ , a double-diffusive case, the density-mode instability exists only for  $t = 9.0$  because the temperature difference contributes an additional decrease of the density gradient. When  $Ra_T = 0$ , a single-diffusive case, the density-mode instability exists for up to  $t = 50.0$  because there is no density-decreasing contribution by the temperature difference but only the solute diffusion. Their net density profiles after  $t = 9.0$  under  $Ra_T = 161,560$  and  $t = 50.0$  under  $Ra_T = 0$  are essentially same in the mid region of the fluid layer, and thus the density-mode instabilities disappear at the same density gradient. The density profiles at  $\omega_m = 282.5$  shown in figure 40 (b) indicate the same fact.

Gresho & Sani (1970) pointed out that a single thermal diffusive layer heated from above can be destabilized by gravity modulations of high frequency and large amplitude and the instability is sub-harmonic. The reason for their conclusion is because the gravity modulation has effect on the stable density gradient of the fluid built up by the temperature difference across the fluid layer. The density-mode instability in the present case is understood in the similar way, i.e. the instability is induced by gravity modulation to the density gradient. The difference is that the density gradient in Gresho & Sani (1970)'s study is established by the temperature gradient across the fluid layer, while the

present density gradient is by solute-only or solute-and- temperature gradient across the fluid layer.

### 8.3.5. Density-Mode Instability under Modulation Amplitudes

Besides  $gy_1 = 0.75$  , the density-mode instability has also been investigated with modulation amplitudes at 0.40, 1.00 and 2.00. When  $gy_1 = 0.40$  , there is only the double-diffusive instability when  $Ra_T = 161,560$  and there is nothing happened when  $Ra_T = 0$  . So, no density-mode instability exists for this case.

When  $gy_1 = 1.00$  , the density-mode instability is shown in figure 41. The feature of the density-mode instability of  $gy_1 = 1.00$  is the same as that of  $gy_1 = 0.75$  . That is, the instability onset is one-layer convective cells, the oscillatory unstable motion is in the sub-harmonic mode, the strong convection accelerates the mixing of the solute difference, and the density gradients right after the instability regions are essentially same regardless of the single- or double-diffusion. The differences are quantitative. When  $Ra_T = 161,560$  , the density-mode instability lies in the region of  $130.7 \leq \omega_m \leq 324.9$  and  $0.0 \leq t \leq 42.0$  . The effect of the density-mode instability on the succeeding double-diffusive instability is seen again. When  $105.9 \leq \omega_m \leq 162.4$  , the density-mode instabilities exist close to the double-diffusive instabilities such that the double-diffusive instability onsets are one-layer convective cells , which are noted by curve *abcd* in figure 41 (a). When  $162.4 \leq \omega_m \leq 324.9$  , the density-mode instability causes the double-diffusive instability to

occur earlier. When  $Ra_T = 0$ , the region of the density-mode instability expands to  $155.4 \leq \omega_m \leq 466.1$  and  $0.0 \leq t \leq 112.0$  (see figure 41(b)).

When  $gy_1 = 2.00$  with  $Ra_T = 0$ , the density-mode instability expands to a wider range of modulation frequency  $28.25 \leq \omega_m \leq 565.0$ . The oscillation frequencies of the instability within this range are summarized in Table 6. Although it is still sub-harmonic at most modulation frequencies as before, the density-mode instability is in the synchronous mode at low modulation frequencies. This agrees with Gresho & Sani (1970)'s conclusion. That is, a stable thermal diffusive layer can be destabilized by gravity modulations sub-harmonically at high frequency and synchronously at low frequency. Saunders et al (1992) reported a similar prediction by linear stability analysis. They predicted that a stably stratified solute layer may experience the most critical instability in the sub-harmonic mode at high modulation frequency, and by increasing the modulation amplitude the solute layer may experience a second critical instability in the synchronous mode as modulation frequency decreasing (See their figure 9).

#### 8.4. Gravity Modulation Without Background Gravity

As noted by Terrones & Chen (1993) and Shu, Li & de Groh (2001), the magnitude of the modulated part of the gravity may be several or even many times of its constant background part in micro-gravitational environment. Therefore, it is interesting to see how the double-diffusive instability behaves under such condition and also to see the effects of background gravity on the instability. Since the net gravity now is upward and

downward alternately, the consequent double diffusion is in the diffusive- and finger-modes alternately. The problem becomes more complicated than before. By letting  $gy_0 = 0.00$  and  $gy_1 = 1.00$ , a computational study has been carried out for different modulation frequencies. Table 7 summarizes the  $t_{onset}$ ,  $f_{onset}$  at different  $\omega_m$ . The related features are presented as follows.

When  $0 < \omega_m \leq 84.75$ , the fluid layer becomes unstable shortly after the computations start. The unstable convective motion is chaotic and no regular pattern can be observed. Power spectrum estimations indicate that there is no consistent dominant frequency  $f_{onset}$  for the unstable motions. The solute gradient is essentially mixed within first  $t = (3.6 \sim 4.8)$ .

When  $84.75 < \omega_m \leq 157.1$ , the fluid layer still becomes unstable shortly after the computations start. The unstable motion is chaotic first and then evolves into regular one-layer vortices fitted in the entire thickness of the fluid layer. The cellular motion is in the sub-harmonic mode. The solute gradient is essentially mixed within initial  $t = 15.0$ .

When  $169.5 \leq \omega_m \leq 197.7$ , the fluid layer is at a transition stage. When  $\omega_m < 197.7$ , the evolution of the unstable motion is similar to that of  $84.75 < \omega_m \leq 157.1$  although it takes up to  $t = 39.0$  for the solute gradient to mix. The estimated frequency for the oscillatory motion, however, is in the synchronous mode first and then switches to the sub-harmonic mode. When  $\omega_m \geq 197.7$ , the fluid layer becomes unstable as before. However, the unstable motion damp out after initial  $t = 9.0$ , and the solute gradient is decreased

through the unstable motion but is still held after the motion. When  $t = 52.8$ , the second instability onsets. And the flow becomes completely unstable since then. The oscillatory frequency of the unstable convection is still in the synchronous mode first and then the sub-harmonic mode.

When  $\omega_m \geq 211.9$ , the fluid layer is stable for at least  $t = 55.8$ . Before the instability onset, the flow is quiescent and the solute difference is decreased only by diffusion. After the instability onset, the unstable convective motion always oscillates in the synchronous mode (see lower part of Table 7). The development of the unstable convective motion, however, is of different features at different modulation frequencies, which is presented as follow:

When  $211.9 \leq \omega_m \leq 392.7$ , the initial convection appears only in the lower half of the layer. After  $t = (3.6 \sim 5.4)$ , new cellular motion also shows up in the upper half, which is obviously weaker than their counterpart in the lower half. Passing another  $t = (3.0 \sim 4.8)$ , the cells separated along the midway start breaking and mixing. The unstable motion is chaotic. Finally the solute gradient disappears across the layer. At this stage, the onset time  $t_{onset}$  is at the same level as the onset time  $t_{onset}$  ( $= 58.2$ ) of the instability under steady gravity.

When  $424.3 \leq \omega_m \leq 628.3$ , the unstable motion still appears in the lower half of the layer first as a series of cells. The cells then stretch upward and fill the entire fluid layer in subsequent  $t = (6.0 \sim 7.8)$ . The developed one-layer cells then start breaking and mixing after another  $t = (1.8 \sim 3.0)$ . The motion is chaotic again. Compared with the onset

time  $t_{onset} = 58.2$  when  $gy_0 = 1.0$ , the onset time  $t_{onset}$  now is increased by (6.2 ~ 22.7) % (see specific  $t_{onset}$  in Table 6). Therefore, the pure gravity modulation makes the fluid layer slightly more stable now.

When  $\omega_m \geq 659.7$ , the unstable motion first appears in the mid region of the fluid layer as small cells. Following it, the cells are stretched upward and downward in vertical direction and fill the whole thickness of the layer as one-layer cells. After  $t = (9.6 \sim 10.8)$  from the onset motion, the one-layer cells start breaking and mixing. The onset time  $t_{onset}$  now is  $t_{onset} \geq 71.4$ , at least a 22.7% increase. In other words, the pure gravity modulation of higher frequency stabilizes the fluid layer even further.

To summarize, the pure modulated gravity may have a significant effect on the double-diffusive fluid layer. When the modulation frequency  $\omega_m$  is low, the gravity modulation makes the fluid layer unstable quickly and the unstable motion is chaotic. As  $\omega_m$  increases, the pure modulated gravity still makes the fluid layer unstable quickly but the induced unstable convection is in the sub-harmonic mode. As  $\omega_m$  increase further to higher range, the modulation makes the fluid layer more and more stable compared with the gravity modulation with constant background part, and the unstable motion is in the synchronous mode. Saunders et al (1992) predicted that a fluid layer of  $Pr = 0.1$  and  $Le = 100$  with  $Ra_r = 1000$ ,  $Ra_s = 300,000$  and  $gy_0 = 0.0$  experiences the sub-harmonic and synchronous modes of instability alternatively with the former is the most critical

mode at high  $\omega_m$ . Here the results show that the instability at high  $\omega_m$  is in the synchronous mode.

## CHAPTER 9.

## CONCLUSIONS

The effects of gravity modulation on the instability of double-diffusive convection of an ethanol-water solution in a horizontal tank heated from below have been investigated by experiments and direct numerical simulations. The conclusions are drawn as follows:

1. For the steady gravity case, a total of six experiments were conducted with intended temperature differences. The average temperature difference is  $\Delta T = 10.16^\circ\text{C}$  and the average time of onset is 94.8 min with a variation from 90 min to 99 min. That is, for a constant  $Ra_T = 161,560$ , the critical state is at  $Ra_S = 125,540$ . The onset is in the oscillatory mode and the dominant oscillatory frequency is  $f_{onset} = 0.043\text{Hz}$ . The flow pattern at onset is two-layer counter-rotating vortices and the wavelength is  $\lambda = (0.91 \sim 1.09)H$ . The two-dimensional numerical simulations accurately reproduce the experiments. Given  $Pr = 7.0$ ,  $Le = 118.3$  and  $Ra_T = 161,560$ , the simulations predict that the instability onsets 97.0 min later, the critical  $Ra_S = 124,030$  and the oscillatory frequency  $f_{onset} = 0.045\text{Hz}$ . The flow pattern is two-layer cells at the onset and the wavelength is  $\lambda = (0.82 \sim 1.00)H$ . The experimental, numerical and analytical results agree with each other very well.

2. For the modulated gravity case, seven experiments were conducted under the same conditions as the steady gravity case except that the gravity is modulated sinusoidally at

frequency of  $1.0\text{Hz}$  and amplitude of  $0.403g$ . It is found that the actual gravity modulation has a destabilizing effect. Specifically, the average onset time reduces to  $t_{onset} = 85.7\text{ min}$  ( $-9.8\%$  from the steady gravity case), the average critical  $Ra_s$  increases to  $Ra_s = 136,140$  ( $+7.8\%$ ) and the onset frequency increases to  $f_{onset} = 0.057\text{Hz}$  ( $+32.6\%$ ). The flow pattern at onset, which is another notable difference, is one-layer counter-rotating vortices, and the wavelength is  $\lambda = (1.39 \sim 2.26)H$ . The computations show that the differences may be due to the actual asymmetry of the gravity modulation. When the gravity is simulated by an ideal sinusoidal modulation of  $1.0\text{Hz}$  and  $0.403g$ , the instability is the same as that under steady gravity. This result is in agreement with the linear stability analysis. When the actual gravity modulation measured in experiments, which is asymmetrical, is fed into the computations, the instability occurs  $90.0\text{ min}$  later with critical  $Ra_s = 125,750$  and  $f_{onset} = 0.051\text{Hz}$ , closer to the experimental results than the ideal gravity modulation.

3. The kinetic energy and mechanical work by pressure, shear stress, thermal buoyancy and solutal buoyancy have been computed for both the steady gravity and the gravity modulation cases. Their oscillation frequencies are closely related to the modulation frequency and/or the onset frequency. For the steady gravity, the energy and all work components oscillate in the synchronous mode with the unstable motion at the onset, and vary randomly before or after the instability onset. For the modulated gravity case, the energy and all work components oscillate synchronously with the modulation frequency throughout the entire instability process. When the modulation frequency is

high, they also oscillate in the synchronous mode with the onset motion at the instability onset.

With the success of the two-dimensional numerical simulation method in predicting the onset of instability in stratified fluid layers, the computation method is used to investigate the following cases that are difficult to investigate experimentally. The results are summarized in the following:

4. The density-mode instability, which is due to the density gradient of the fluid layer that is sensitive to certain frequencies and amplitudes of gravity modulation, is found in certain examples in this study. The density-mode instability exists in both single- and double-diffusive fluid layers and occurs before the double-diffusive instability. When the modulation frequency is high and the modulation amplitude is small, the density-mode stability is in the sub-harmonic mode. When the modulation frequency is low and the modulation amplitude is large, the instability is in the synchronous mode. This result is in agreement with those of Gresho & Sani (1970) for thermally stratified fluid layers under gravity modulation. The unstable motion of the density-mode instability is one-layer cellular convection. The convection accelerates the mixing of the density gradient of the fluid layer, thus causing the succeeding double-diffusive instability to onset earlier.

5. Chen (2001) predicted that a resonance phenomenon exists in a double-diffusive fluid layer of  $Pr = 7.0$ ,  $Le = 100.0$ ,  $Ra_s = 3200$  under gravity modulation of  $gy_0 = 1.0$  and  $gy_1 = 0.40$ . The critical  $Ra_T$  decreases from 4,758 under steady gravity to 4,214 under modulated gravity at the critical modulation frequency  $\omega_m = 54.26$ , and the instability

onset is in the sub-harmonic mode. Such resonance phenomenon has been confirmed by the direct simulations and also been found under the present lab conditions of  $Pr = 7.0$ ,  $Le = 118.3$ ,  $Ra_T = 161,560$ , initial  $Ra_S = 238,830$  and  $gy_0 = 1.0$ . At critical modulation frequency  $\omega_m = 70.6$ , the onset time  $t_{onset}$  decreases from 58.2 under steady gravity to 51.0, 43.5 and 38.0 for  $gy_1 = 0.40$ , 0.75 and 1.00 respectively. That is, the destability effect due to the resonance increases as the modulation amplitude increases.

6. The computations have also shown that the background constant gravity may have important effects on the double-diffusive layers under the lab conditions. With the background gravity, the instability onset is at  $t_{onset} = 58.2$  and  $f_{onset} = 28.27$  for both steady gravity and ideal modulated gravity of high frequency. Without the background gravity, effects of the gravity modulation depend on the modulation frequency  $\omega_m$ . When  $\omega_m$  is low, the gravity modulation destabilizes the fluid layer. The instability occurs rapidly and the unstable motion is chaotic. When  $\omega_m$  is intermediate, the instability may still develop quickly but the onset motions is in the sub-harmonic mode; or the instability may also happen at the equivalent onset time  $t_{onset}$  of steady gravity and the onset motion is in the synchronous mode. When  $\omega_m$  is high, the gravity modulation stabilizes the fluid layer and the delayed instability onset is in the synchronous mode.

## APPENDIX A

## LIST OF FIGURES

Figure 1. The test tank.....	78
Figure 2. Diagram to illustrate the deduction of temperature on the upper boundary.....	79
Figure 3. The oscillating platform.....	80
Figure 4. The front panel of LabVIEW program.....	81
Figure 5. The hooked-up experimental apparatus.....	82
Figure 6. Solute and temperature distributions at different times.....	83
Figure 7. The shadowgraphs of solute distribution in the tank at different times.....	84
Figure 8. The coordinate system.....	85
Figure 9. Velocities at discrete points in flow field.....	86
Figure 10. Power spectrum estimations of the oscillation of onset motion.....	87
Figure 11. Vertical component of velocity $v$ to confirm the instability onset in experiments .....	88
Figure 12. The time sequence of streakline images to illustrate the instability onset under steady gravity.....	89
Figure 13. Velocity vectors and vorticity contours obtained by the PIV program.....	91
Figure 14. Velocity vectors and vorticity contours of the unstable motion to illustrate the oscillation of instability onset.....	92
Figure 15. Evolution of vertical component of velocity $v$ to illustrate the oscillation of instability onset under steady gravity.....	93

## LIST OF FIGURES -- Continued

Figure 16. The distribution of dominant frequencies within the mid-half width of the tank from experiments under steady gravity.....	94
Figure 17. The distribution of dominant frequencies of steady gravity.....	95
Figure 18. The time sequence of streakline images to illustrate the instability onset under gravity modulation.....	96
Figure 19. Velocity vectors and vorticity contours of the unstable motion to illustrate the oscillation of instability onset.....	98
Figure 20. The evolution of vertical component of velocity under unsteady gravity.....	99
Figure 21. The distribution of dominant frequencies of gravity modulation.....	100
Figure 22. The time history of $ \psi $ to confirm the instability onset.....	101
Figure 23. The time sequence of streamline images to illustrate the development of instability onset under steady gravity.....	102
Figure 24. The evolution of vertical component of velocity $v$ under steady gravity.....	103
Figure 25. The creeping horizontal convection.....	104
Figure 26. Comparison of the ideal and actual gravity modulations.....	105
Figure 27. The time rate of change of the total kinetic energy and mechanical work under steady gravity.....	106
Figure 28. The oscillation frequencies of the total kinetic energy and mechanical work under steady gravity.....	107
Figure 29. Longitudinal distributions of mechanical work under steady gravity.....	108

## LIST OF FIGURES -- Continued

Figure 30. The time rate of change of the total kinetic energy and mechanical work under gravity of modulation of $\omega_m = 628.3$ and $gy_1 = 0.40$ .....	109
Figure 31. The oscillation frequencies of the total kinetic energy and mechanical work under gravity modulation of $\omega_m = 628.3$ and $gy_1 = 0.40$ .....	110
Figure 32. The oscillation frequencies of the total kinetic energy and mechanical work under gravity modulation of $\omega_m = 78.5$ and $gy_1 = 0.40$ .....	111
Figure 33. The resonance phenomenon under gravity modulation of $gy_0 = 1.0$ and $gy_1 = 0.40$ with constant $Ra_s = 3200$ .....	112
Figure 34. The resonance phenomenon under gravity modulation of $gy_0 = 1.0$ and $gy_1 = 0.40, 0.50, 0.75$ and $1.00$ with initial $Ra_s = 238,830$ .....	113
Figure 35. The instability maps under gravity modulation of $gy_1 = 0.75$ .....	114
Figure 36. The time sequence of streamline contours of the unstable motion of the density-mode instability at $Ra_T = 161,560$ , $\omega_m = 240.1$ and $gy_1 = 0.75$ .....	115
Figure 37. The evolution of vertical component of velocity $v$ throughout the density-mode instability under gravity modulation of $\omega_m = 240.1$ and $gy_1 = 0.75$ ...	116
Figure 38. The solute differences across the fluid layer at $t = 50.0$ .....	117
Figure 39. Solute profiles under modulated gravity of $gy_1 = 0.75$ and $\omega_m = 169.5, 282.5$ at $t = 36.0$ .....	118

## LIST OF FIGURES -- Continued

- Figure 40. The distributions of density right after the density-mode instability  
under gravity modulations of  $gy_1 = 0.75$  and  $\omega_m = 240.1, 282.5$  .....119
- Figure 41. The instability maps under gravity modulation of  $gy_1 = 1.00$  .....120

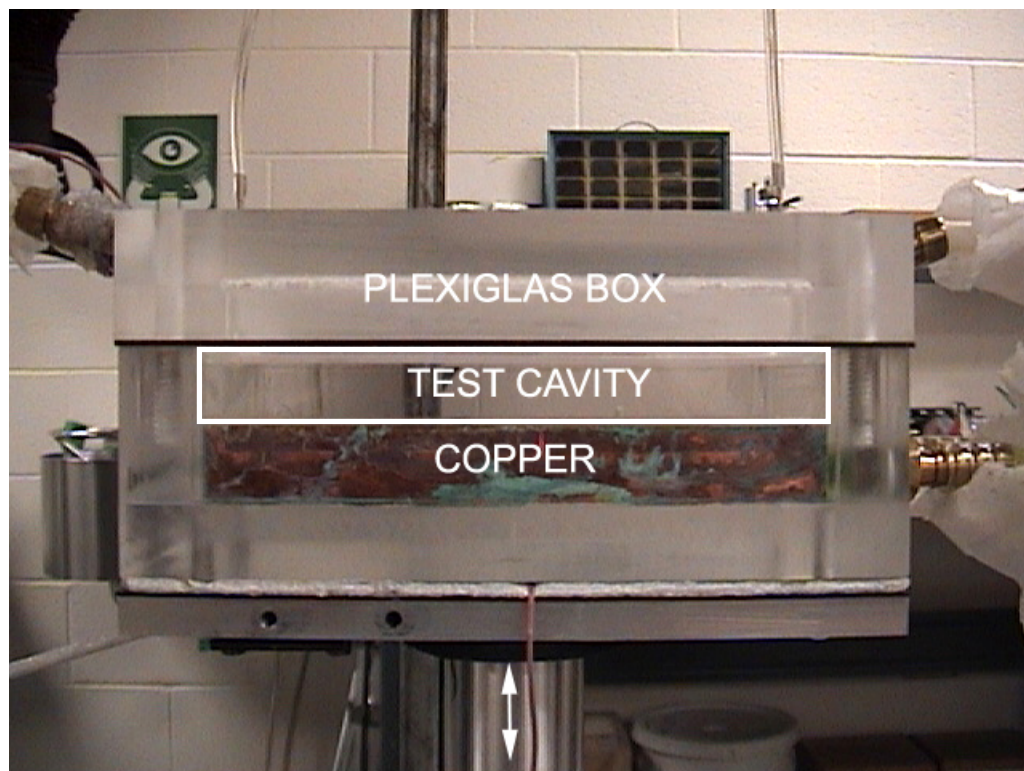


Figure 1. The test tank.

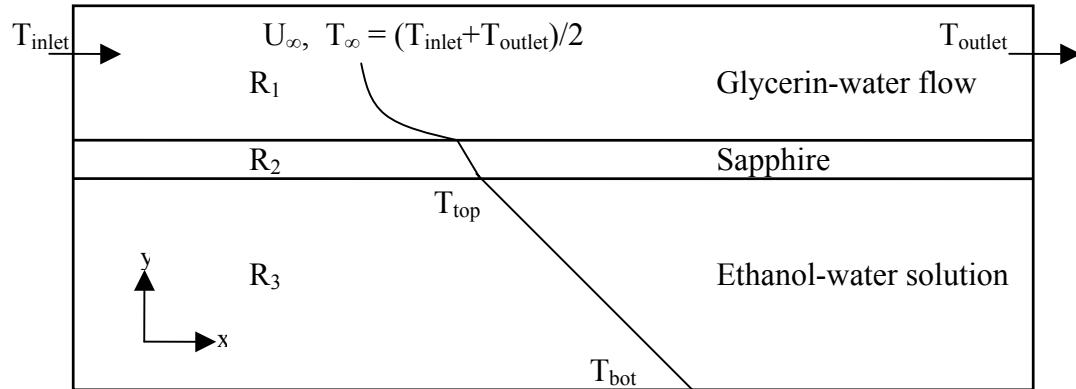
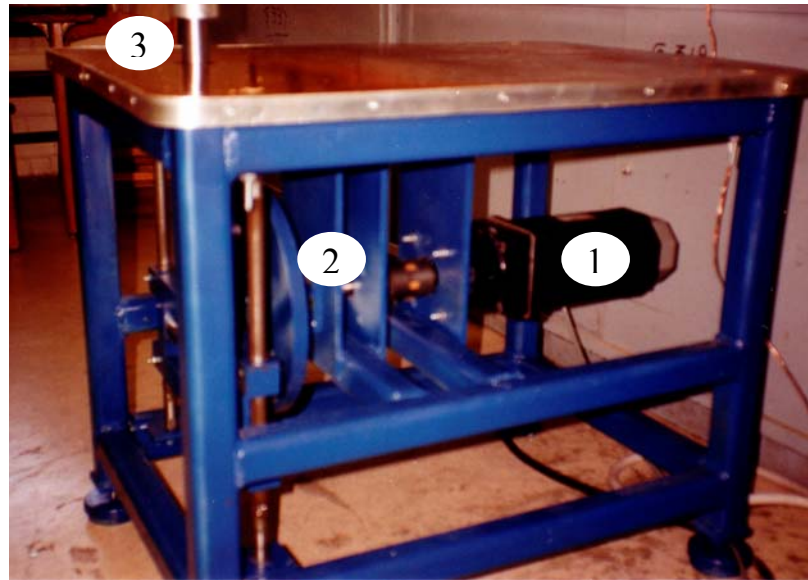


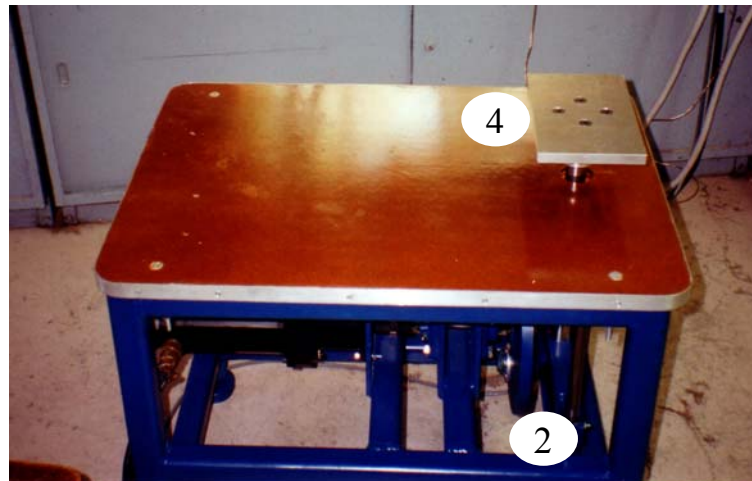
Figure 2. Diagram to illustrate the deduction of temperature on the upper boundary.

$U_{\infty}$  is estimated by circulation rate of bath and geometry of passage. Thermal resistance  $R_1$  is estimated by the internal turbulent correlation given by Incropera & DeWitt (2002).  $R_2$  and  $R_3$  are calculated by their properties and geometry. Lastly,  $T_{top}$  is solved from the

equation of energy balance in  $y$ -direction 
$$\frac{T_{bot} - T_{top}}{R_3} = \frac{T_{bot} - T_{\infty}}{R_1 + R_2 + R_3}.$$



(a)



(b)

Figure 3. The oscillating platform. (a) side view; (b) top view. 1--DC motor; 2--flywheel; 3--vertical shaft; 4--platform to mount the test tank and camera.

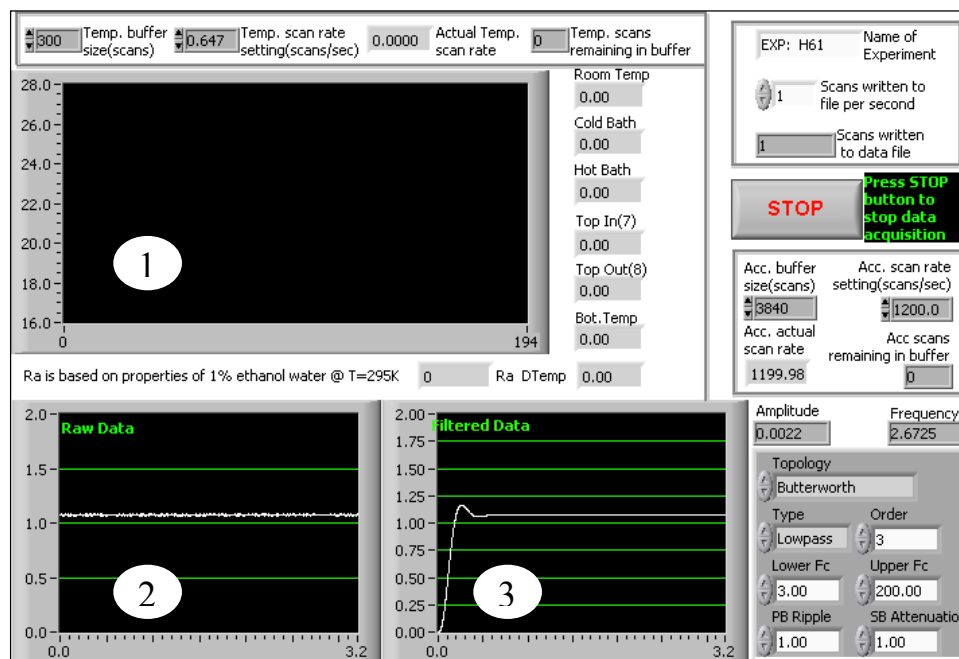


Figure 4. The front panel of LabVIEW program.

Window ① displays measured temperatures. Windows ② and ③ displays the measured gravitational accelerations without and with filtering.

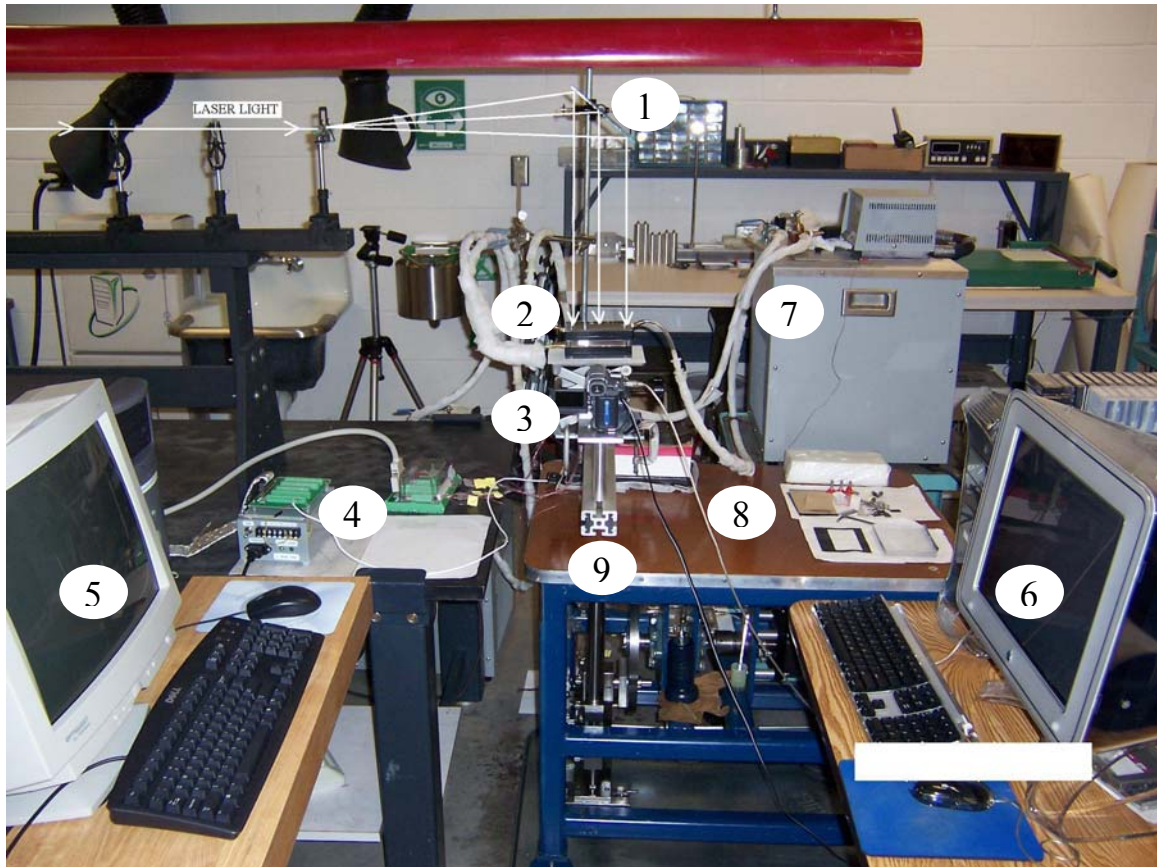


Figure 5. The hooked-up experimental apparatus.

1--deflecting mirror to cast the light sheet to illuminate the mid-plane of the tank; 2--test tank; 3--camera; 4--LabVIEW connectors to stream temperature and acceleration signals into PC; 5--PC to display and save the signals; 6--Apple computer to display and save movie clips; 7--constant temperature bath; 8—oscillating platform; 9--rail (connected to the vertical shaft) on which the tank and camera are fixed.

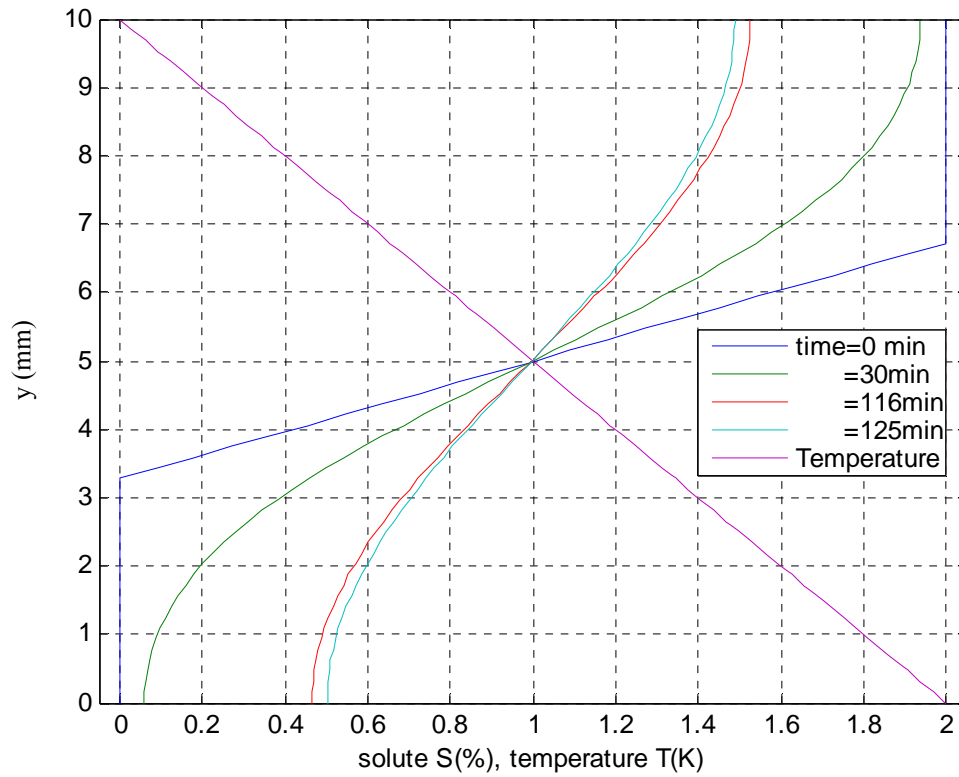


Figure 6. Solute and temperature distributions at different times.

Note: the solute profile is shrinking as time increases while the imposed temperature is fixed. The scale of temperature is shifted arbitrarily for convenience. The solute distributions at  $t = 116$  min and  $125$  min are the distributions corresponding to the instability onset under steady and modulated gravities.



(a) right after filling



(b) 30 min after filling

Figure 7. The shadowgraphs of solute distribution in the tank (a) right after filling and (b) 30 min after filling. The pure water in the lower half is dyed in orange and the 2% ethanol-water solution in the upper half is colorless without dyeing. It is seen from (a) that the initial solute distribution is essentially step-wise and from (b) that the step-wise distribution is smoothing out.

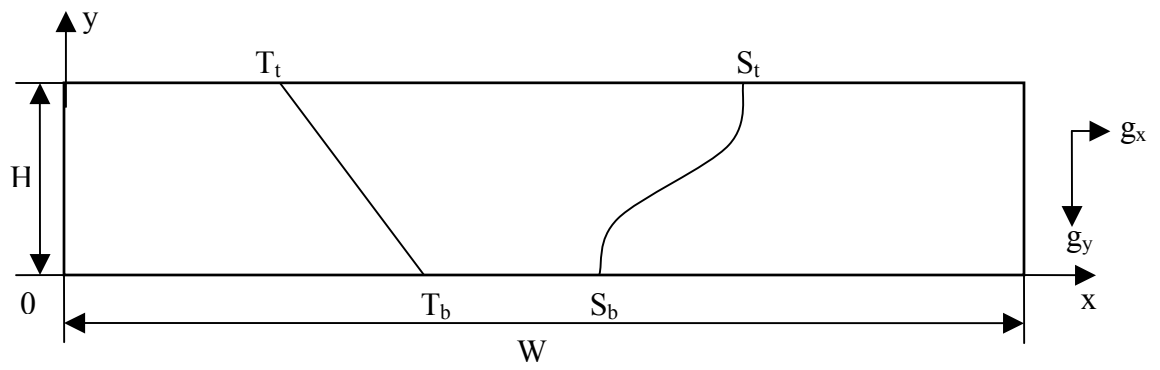


Figure 8. The coordinate system.

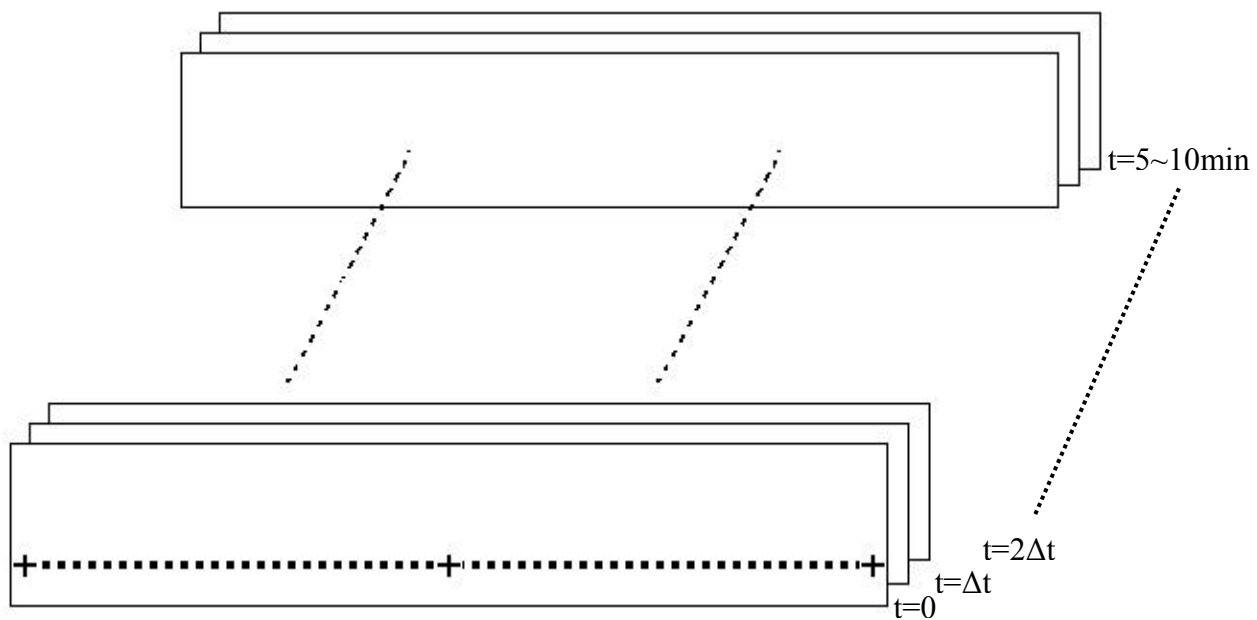


Figure 9. Velocities at discrete points in flow field.

Square – experimental locations; Cross – computational locations.

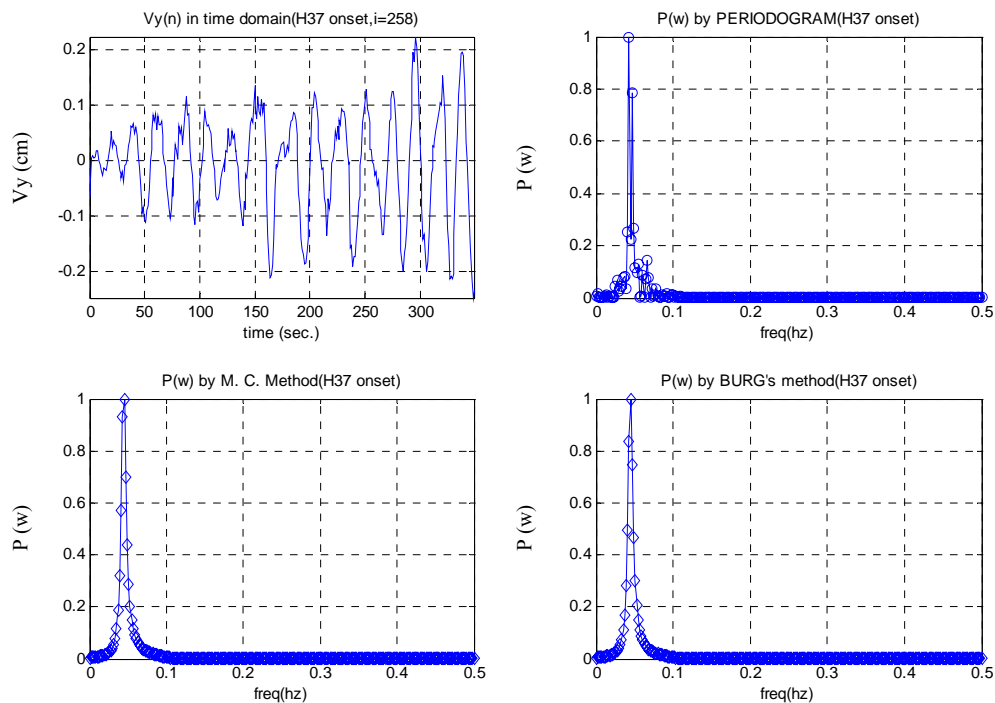


Figure 10. Power spectrum estimations of the oscillation of onset motion.

The upper-left figure shows the time sequence of vertical component of velocity at a point in flow field. The other three figures show the power spectra of the time history by the three methods. The oscillatory frequency is determined by the overall behavior of power spectra from the three methods.

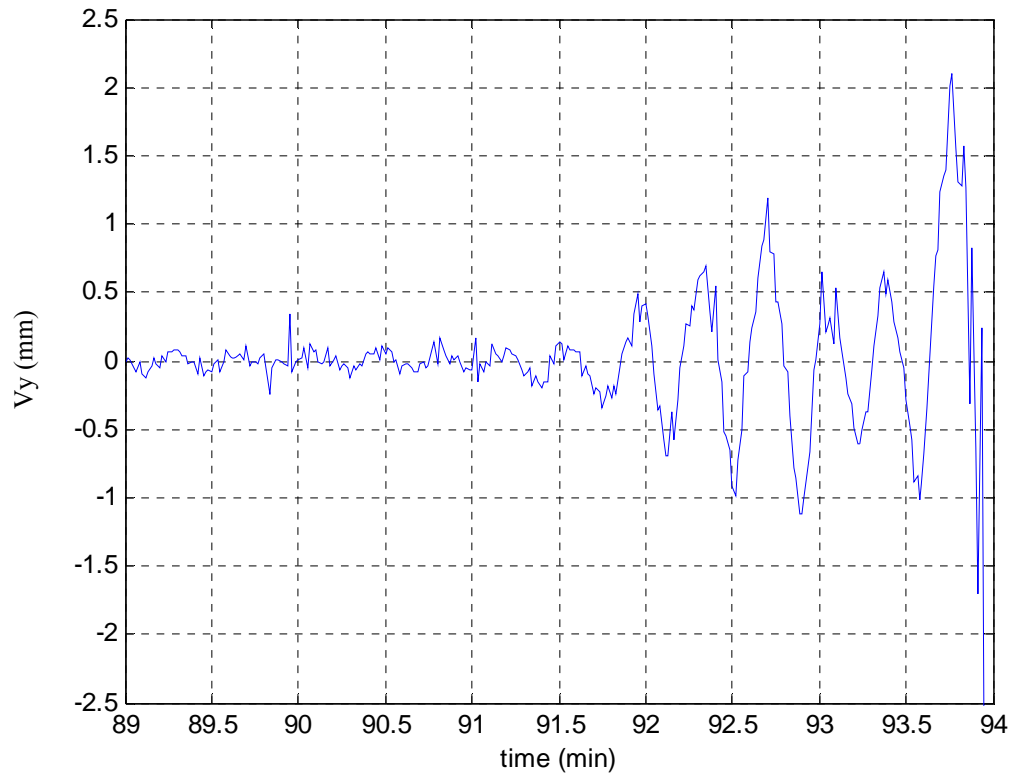


Figure 11. Vertical component of velocity to confirm the instability onset in experiments by observing the onset of its regular oscillation. Here the velocity is from Experiment H5 and the instability onset of H5 is decided at  $t_{onset} = 91$  min . Experiment H5 is summarized in Table 1.

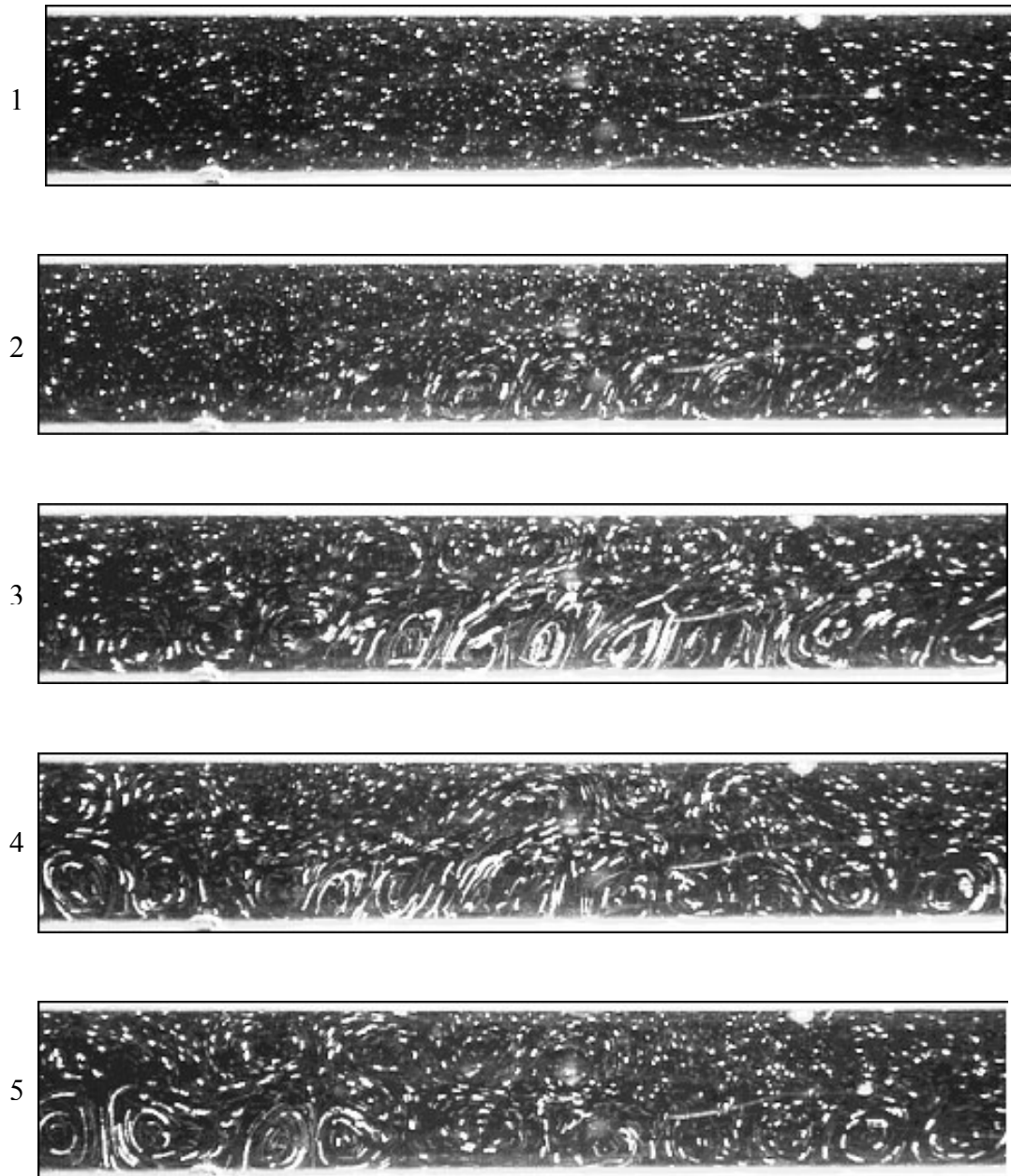


Figure 12. The time sequence of streakline images from Experiment H6 to illustrate the instability onset under steady gravity. Image 1 is at  $t = 98$  min and the time of onset is  $t_{onset} = 99$  min . The exposure time of images 1 and 2 is 6sec. The time interval is 1 min except for images 8, 9 and 10 with interval of 2 min.

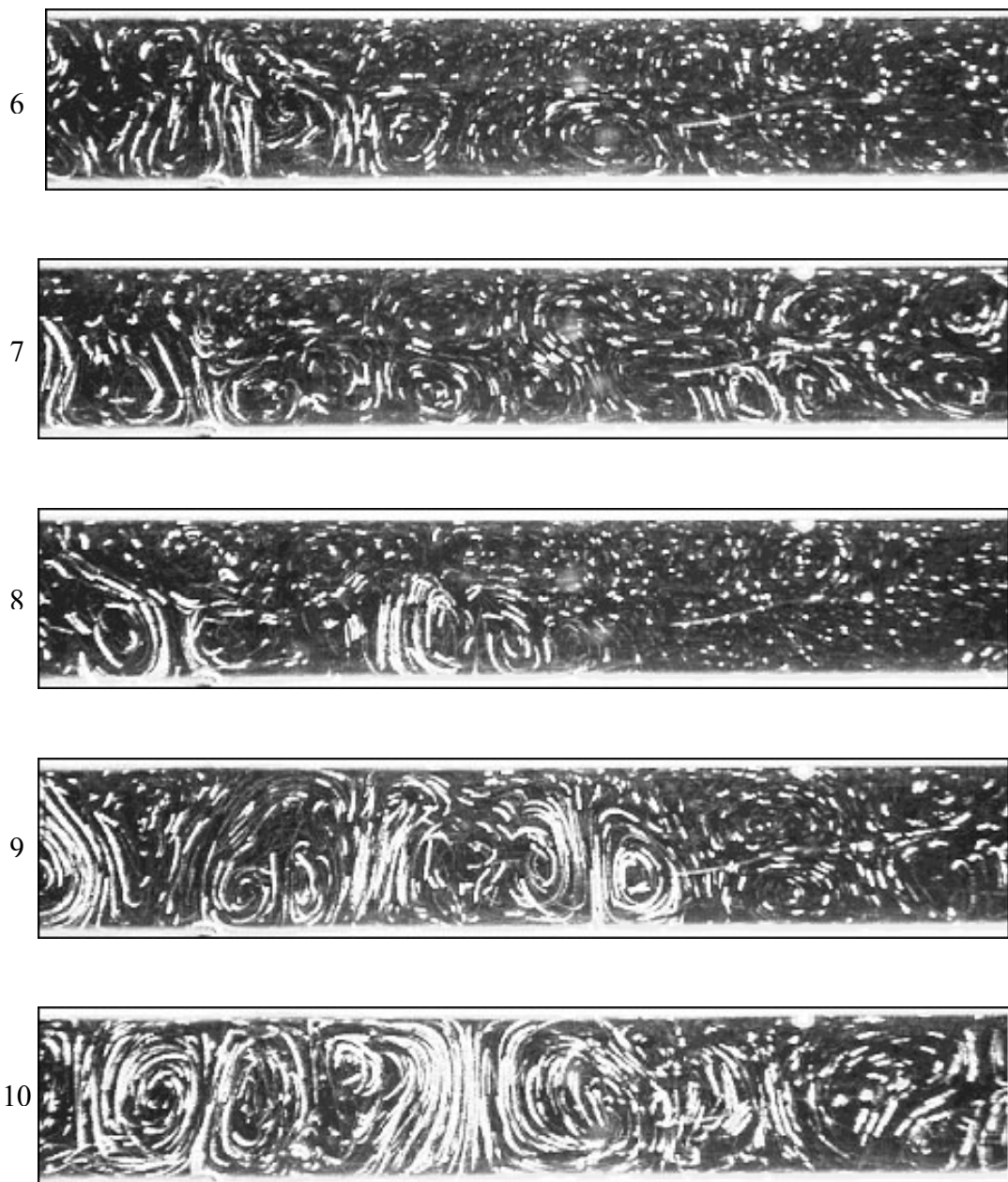


Figure 12 Continued.

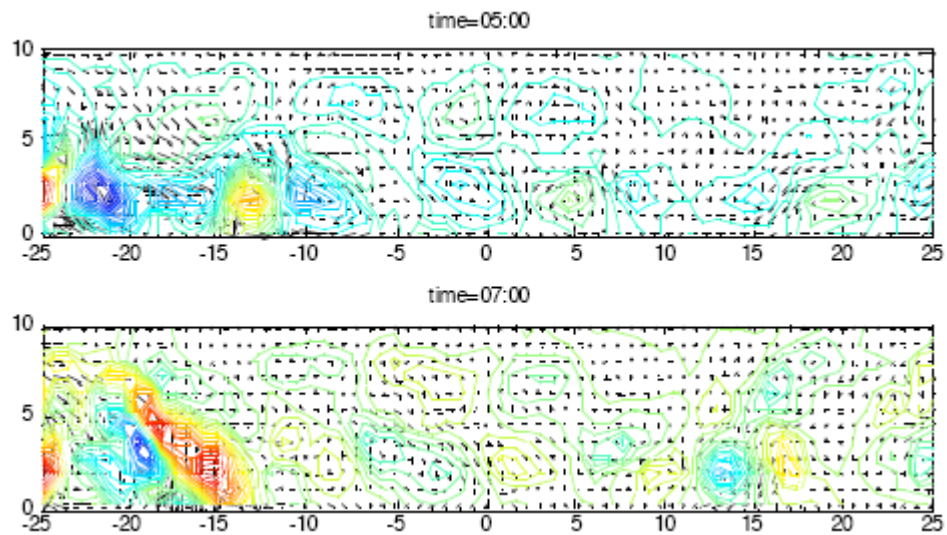


Figure 13. Velocity vectors and vorticity contours of images 5 and 7 in figure 12 obtained by the PIV program. Color index of vorticity contours: red – positive; blue – negative.

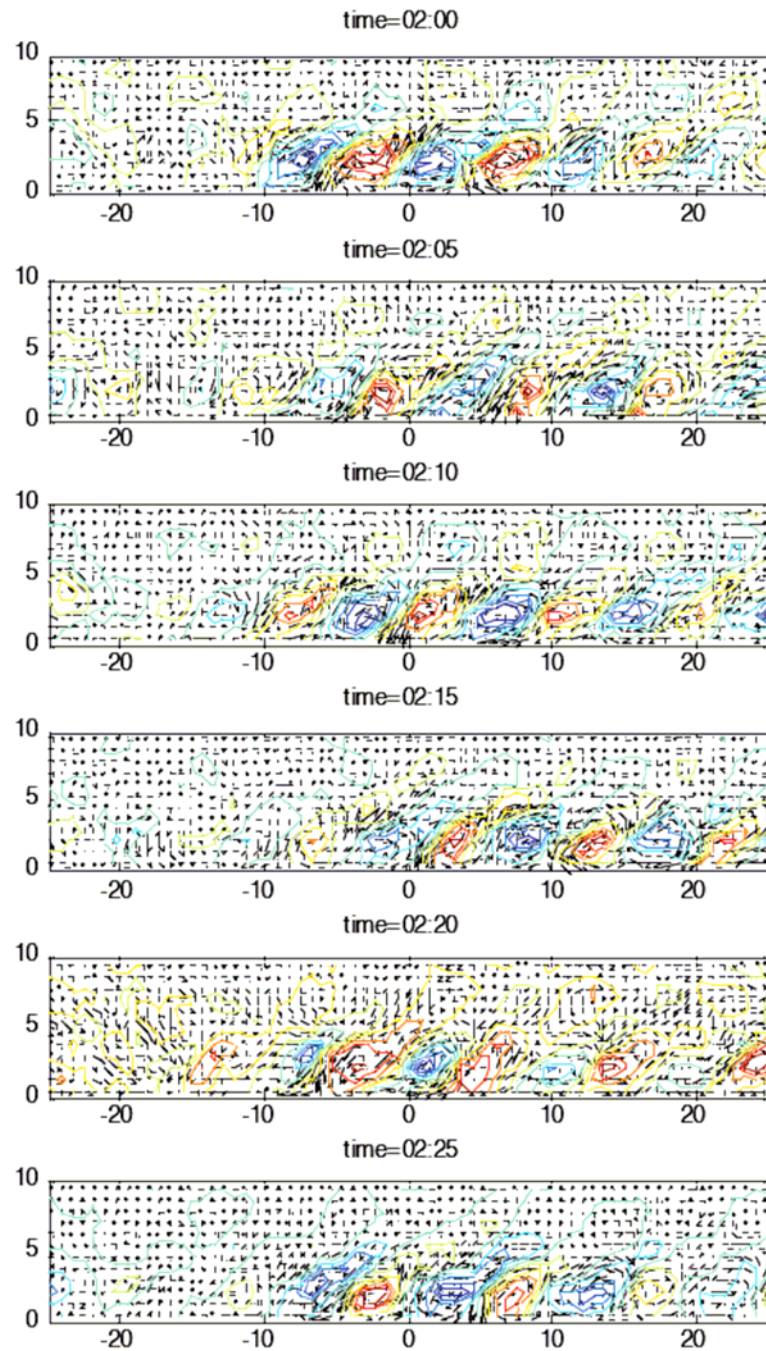


Figure 14. Velocity vectors and vorticity contours of the unstable motion to illustrate the oscillation of instability onset. The first image corresponds to the streakline image 2 in figure 12.

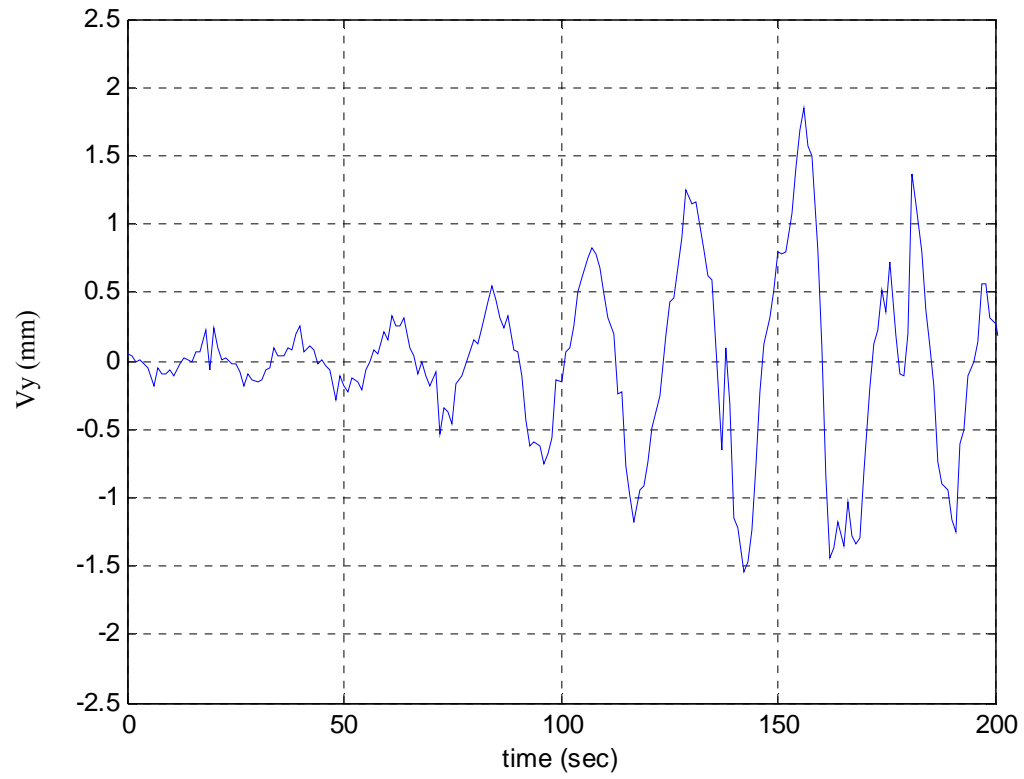


Figure 15. Evolution of vertical component of velocity  $v$  at a point from Experiment H2 to illustrate the oscillation of instability onset under steady gravity.

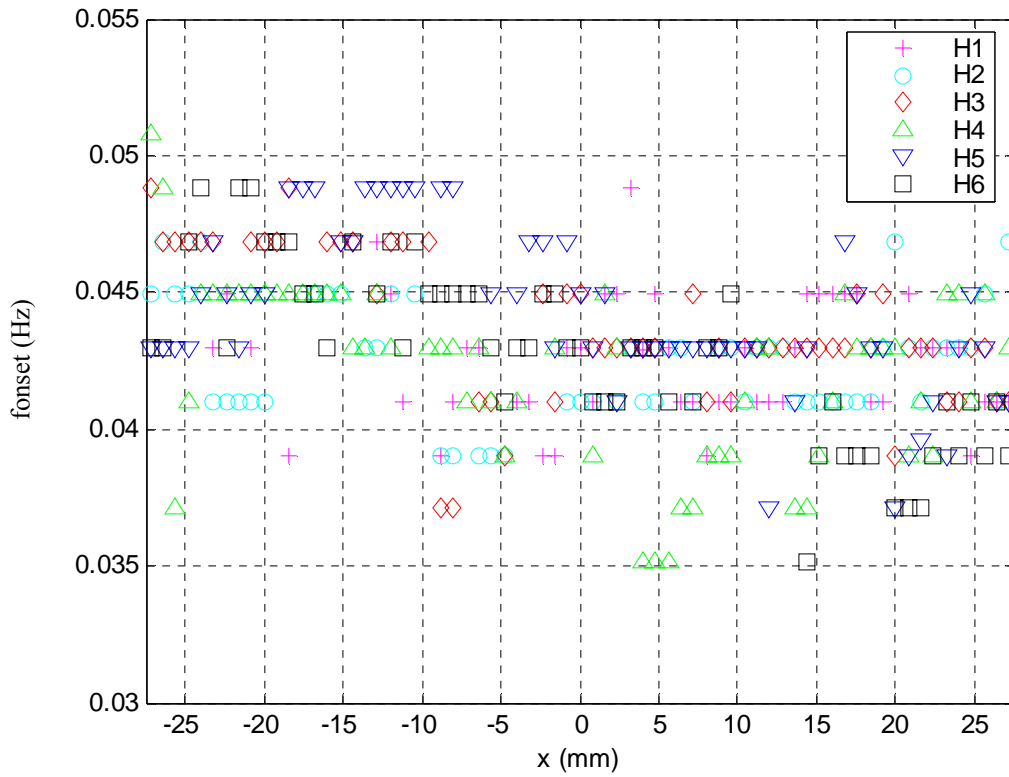


Figure 16. The distribution of dominant frequencies within the mid-half width of the tank from six experiments of steady gravity.

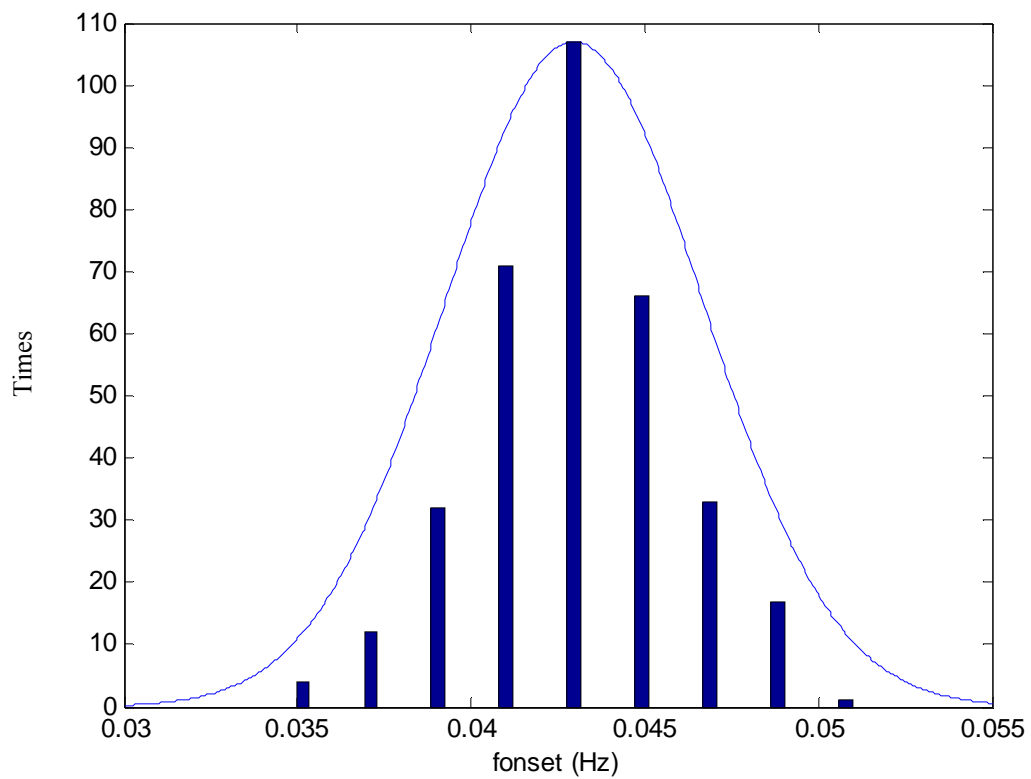


Figure 17. The distribution of dominant frequencies of steady gravity. Line: ideal Gaussian distribution; bar: actual distribution.

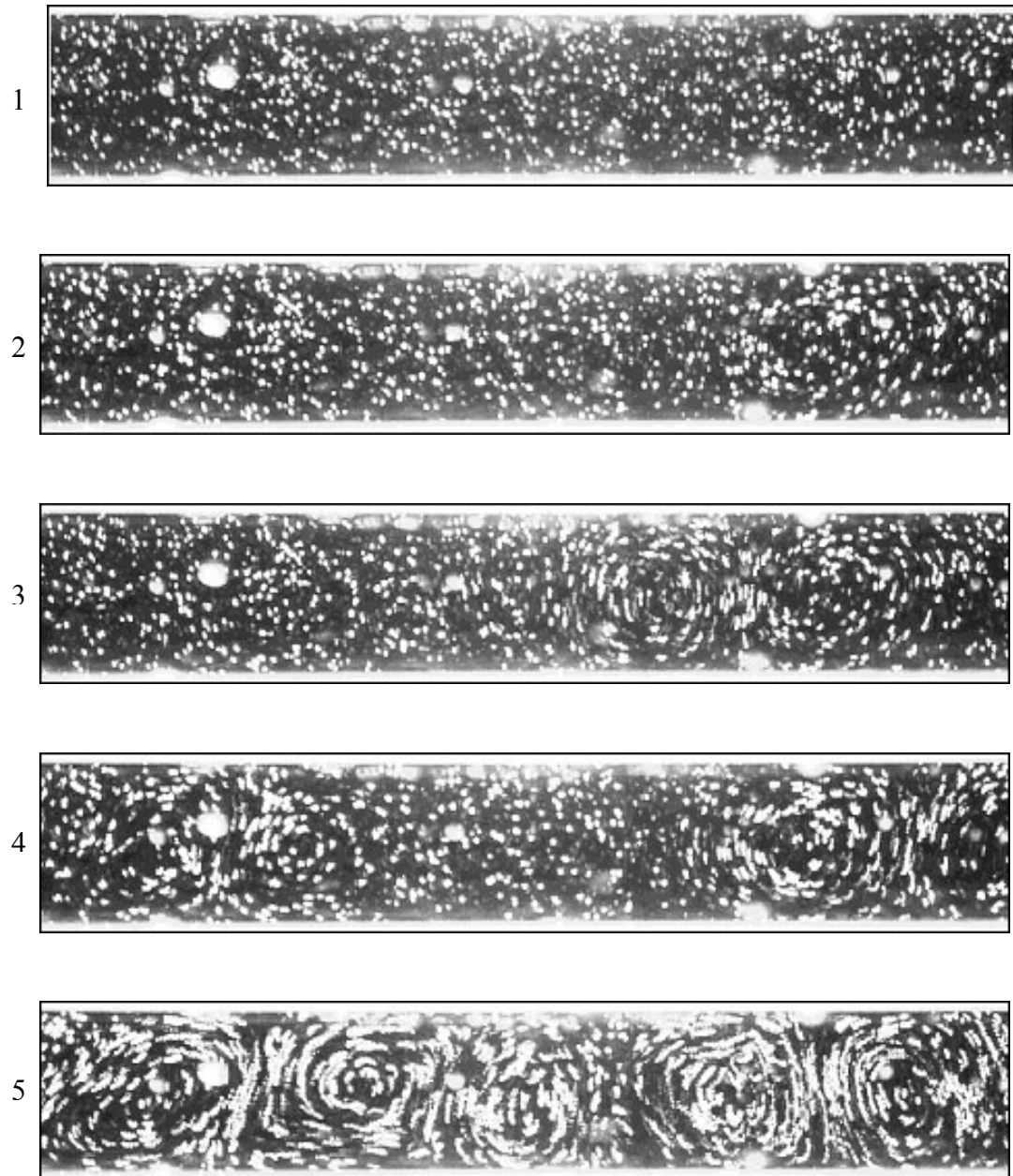


Figure 18. The time sequence of streakline images from Experiment H8 to illustrate the instability onset under the gravity modulation. Image 1 is at  $t = 86$  min and the time of onset  $t_{onset} = 87$  min . The exposure time of images 1 and 2 is 6 sec. The time interval is 1 min.

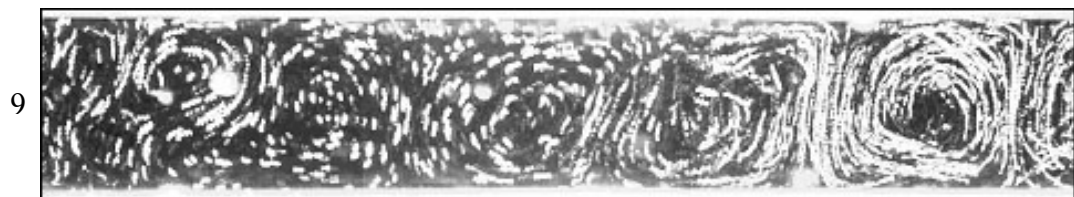
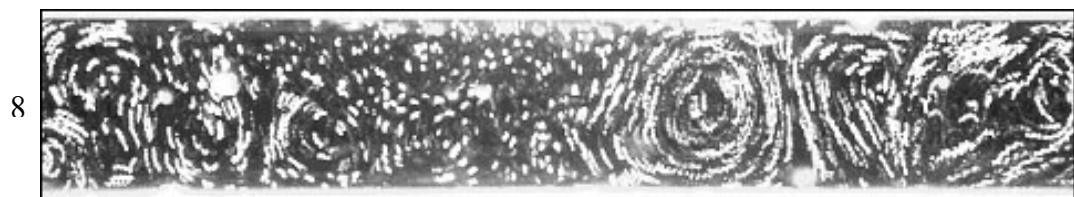
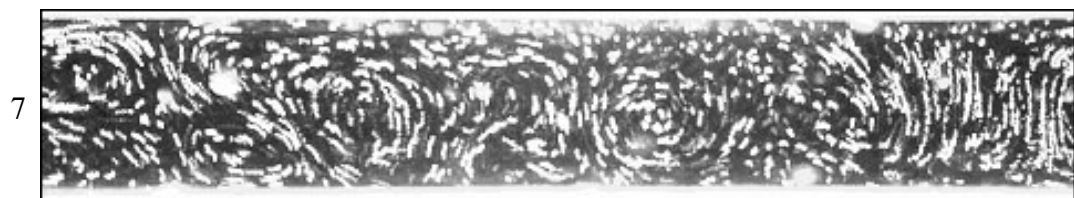


Figure 18 Continued.

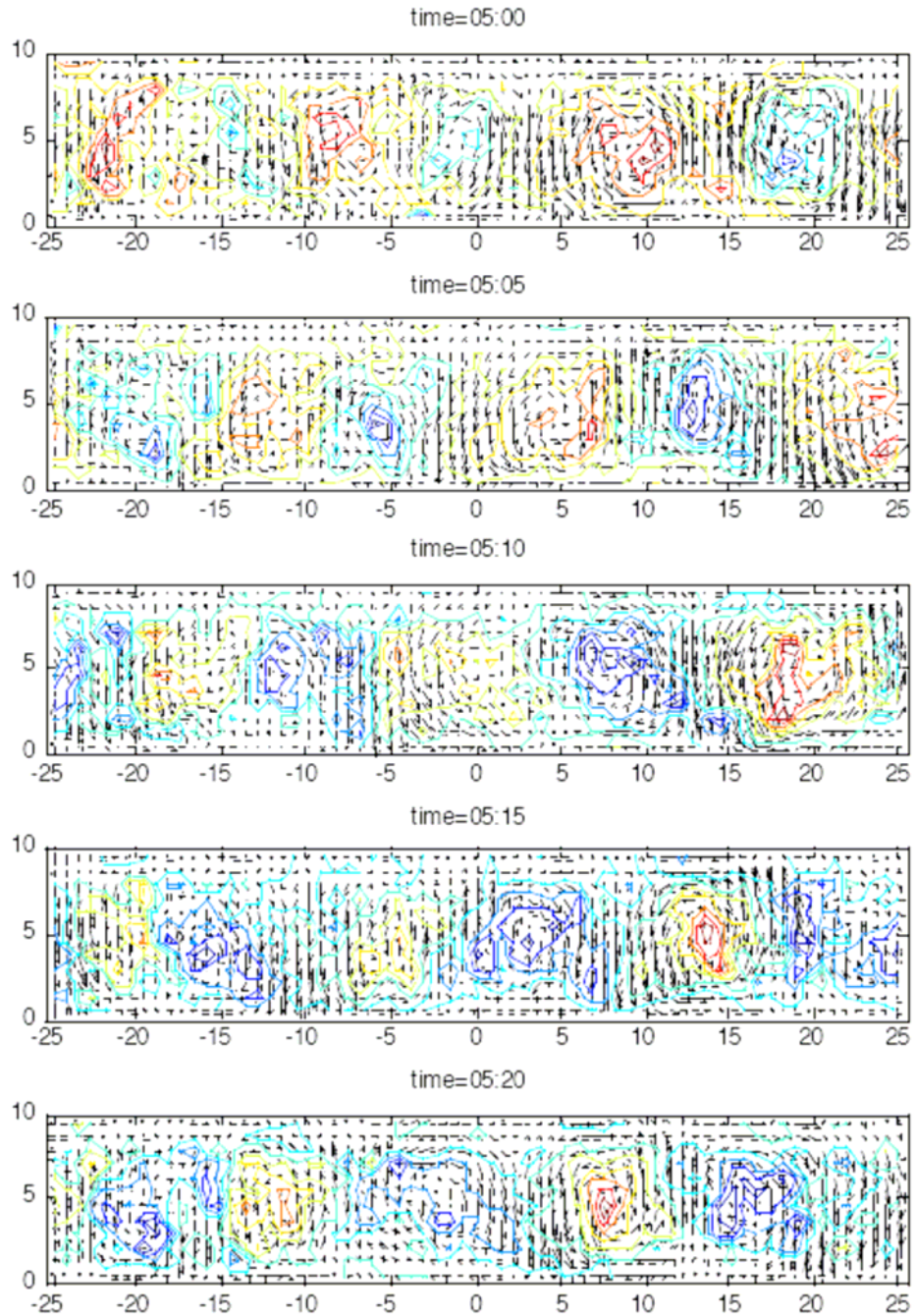


Figure 19. Velocity vectors and vorticity contours of the unstable motion to illustrate the oscillation of the instability. The first image corresponds to streakline image 5 in figure 18.

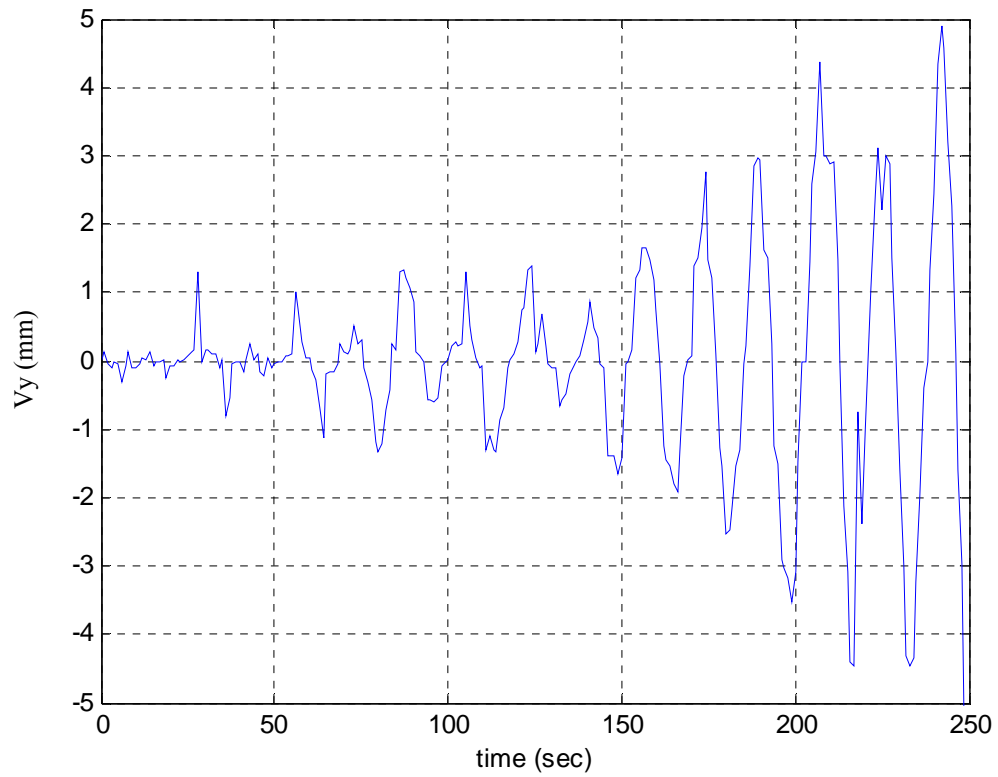


Figure 20. The evolution of the vertical component of velocity  $v$  at a point from Experiment H8 to illustrate the oscillation of onset motion under modulated gravity.

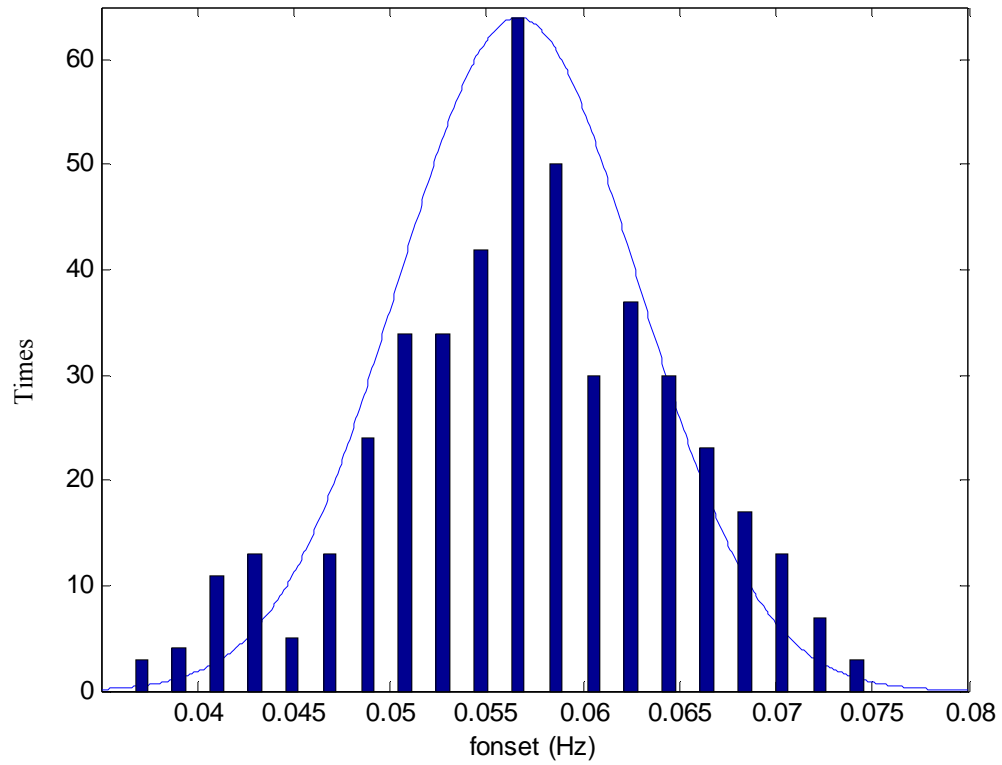


Figure 21. The distribution of dominant frequencies from seven experiments of modulated gravity. Line: ideal Gaussian distribution; bar: actual distribution.

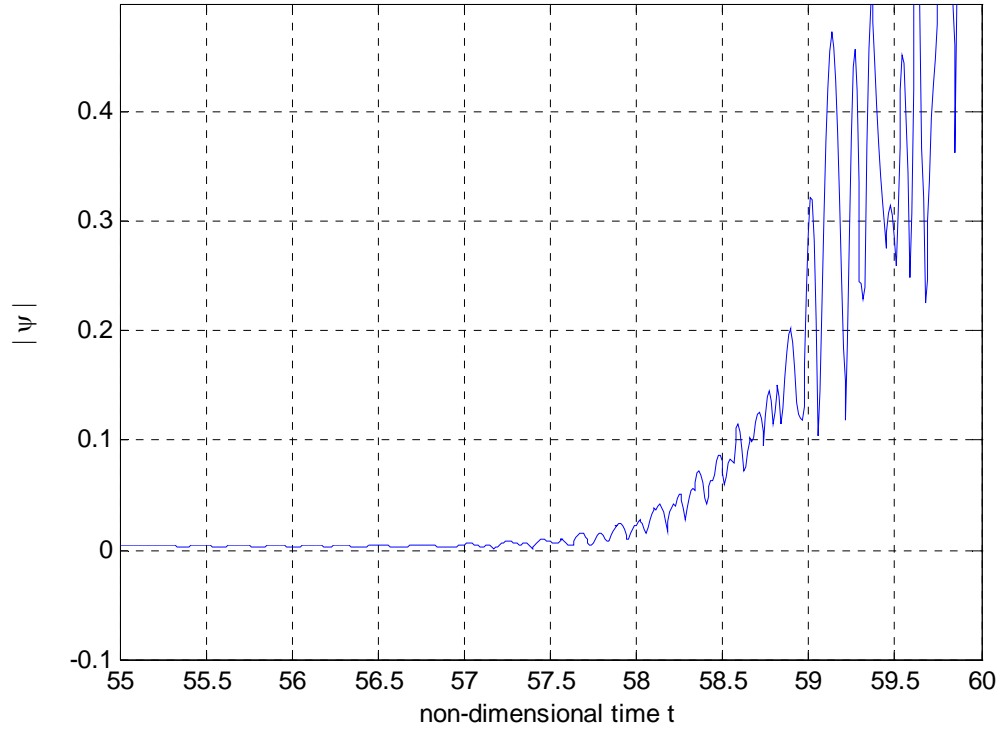


Figure 22. The time history of  $|\psi|$  to confirm the instability onset.

The  $|\psi|$  is the average absolute value of stream functions at points  $(2.75, 0.25)$ ,  $(5.5, 0.25)$  and  $(8.25, 0.25)$  in the flow field. It is seen that  $|\psi|$  oscillates from  $t = 57.0$ . The related parameters of this case are  $Pr = 7.0$ ,  $Le = 118.3$ ,  $Ra_T = 161,560$ , initial  $Ra_s = 238,830$ ,  $gy_0 = 1.00$ ,  $gy_1 = 0.00$ ,  $gx_0 = -0.01$  and  $gx_1 = 0.00$ .

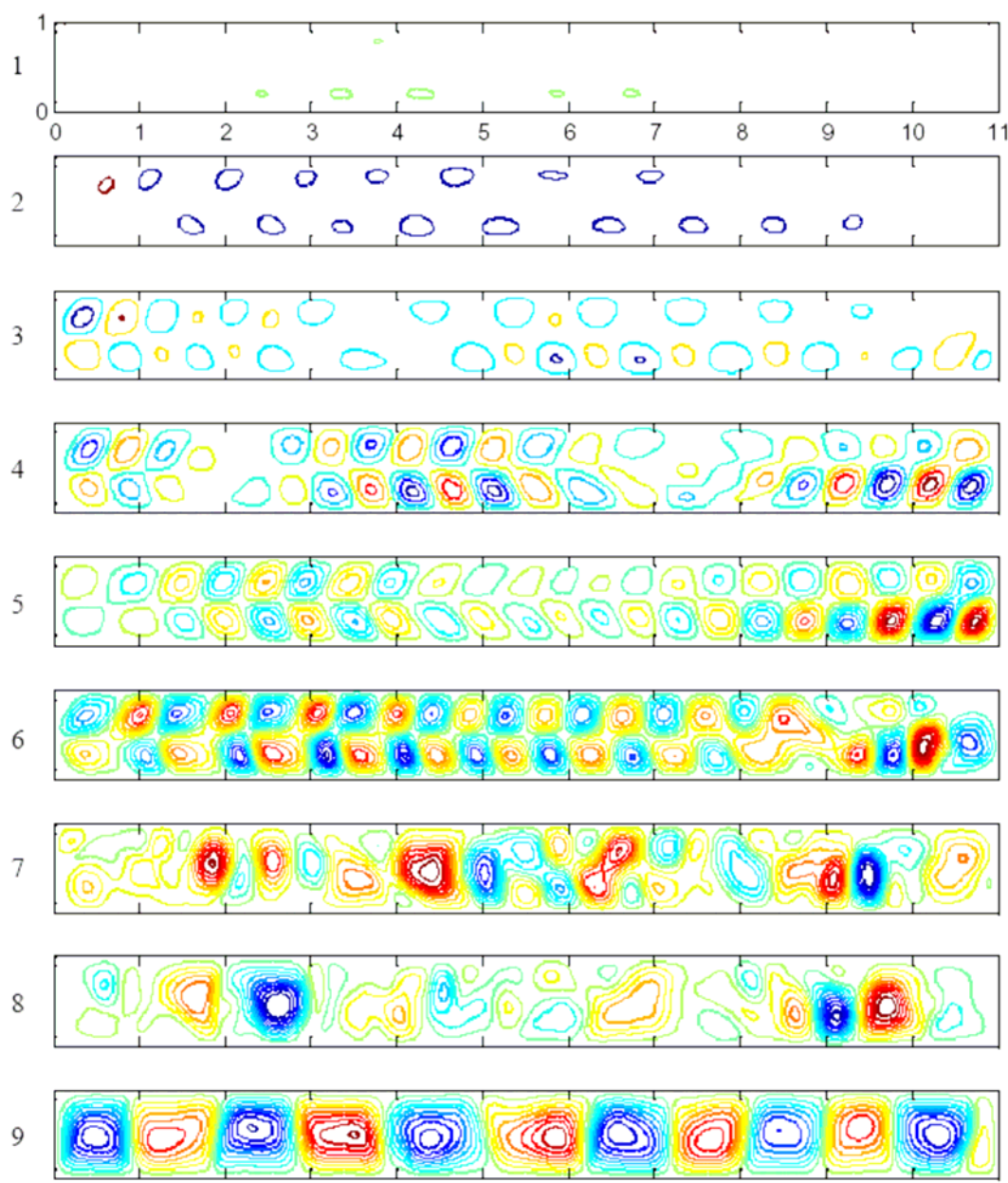


Figure 23. The time sequence of streamline image to illustrate the development of instability onset under steady gravity. The related parameters can be found in figure 22. Image 1 is the onset at  $t = 57.0$ .  $\Delta\psi = (-0.1 \sim 0.1)/18$  in images 1, 2, 3 and 4,  $\Delta\psi = (-0.35 \sim 0.35)/18$  in image 5,  $\Delta\psi = (-1.0 \sim 1.0)/18$  in image 6,  $\Delta\psi = (-2.0 \sim 2.0)/18$  in image 7, and  $\Delta\psi = (-3.5 \sim 3.5)/18$  in image 8,  $\Delta\psi = (-7.0 \sim 7.0)/18$  in image 9. The time interval is 1 min except image 9 which is 3 min after image 8.

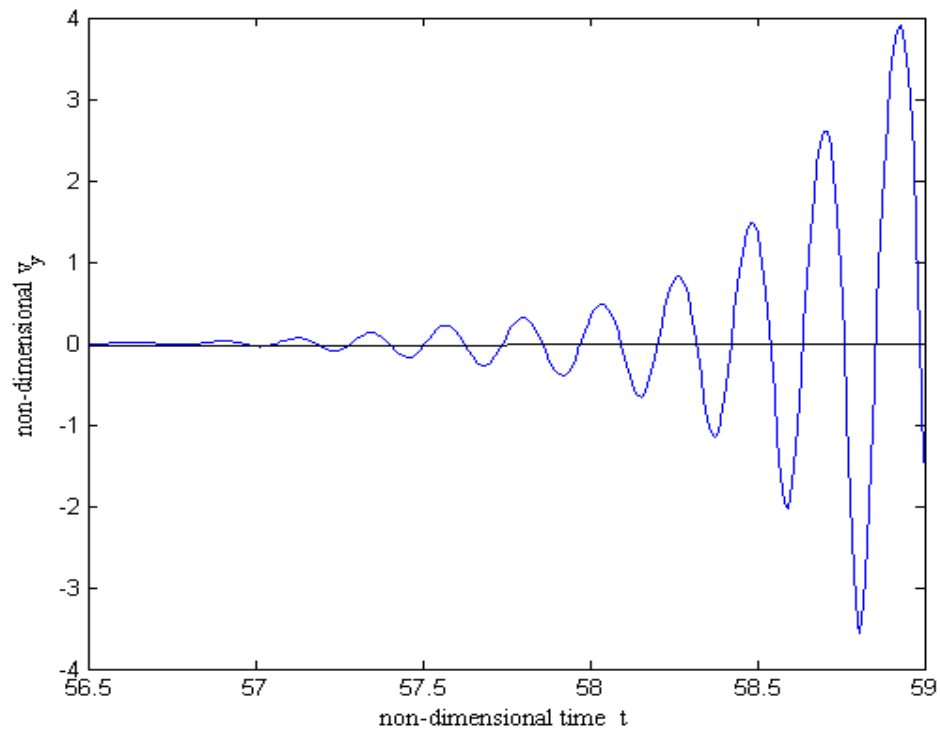
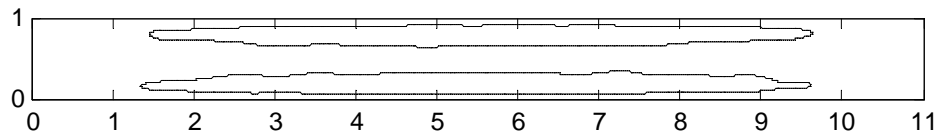


Figure 24. The evolution of velocity  $v$  at point (5.5, 0.25) under the steady gravity. The related parameters can be found in figure 22.



(a)



(b)

Figure 25. The creeping horizontal convection. (a) a streakline image from Experiment H2. The exposure time is 12 sec; (b) a computed stream function contour before the instability onset with  $Pr = 7.0$  ,  $Le = 118.3$  ,  $Ra_T = 161,560$  ,  $gy_0 = 1.0$  ,  $gy_1 = 0.0$  ,  $gx_0 = -0.01$  and  $gx_1 = 0.0$  .

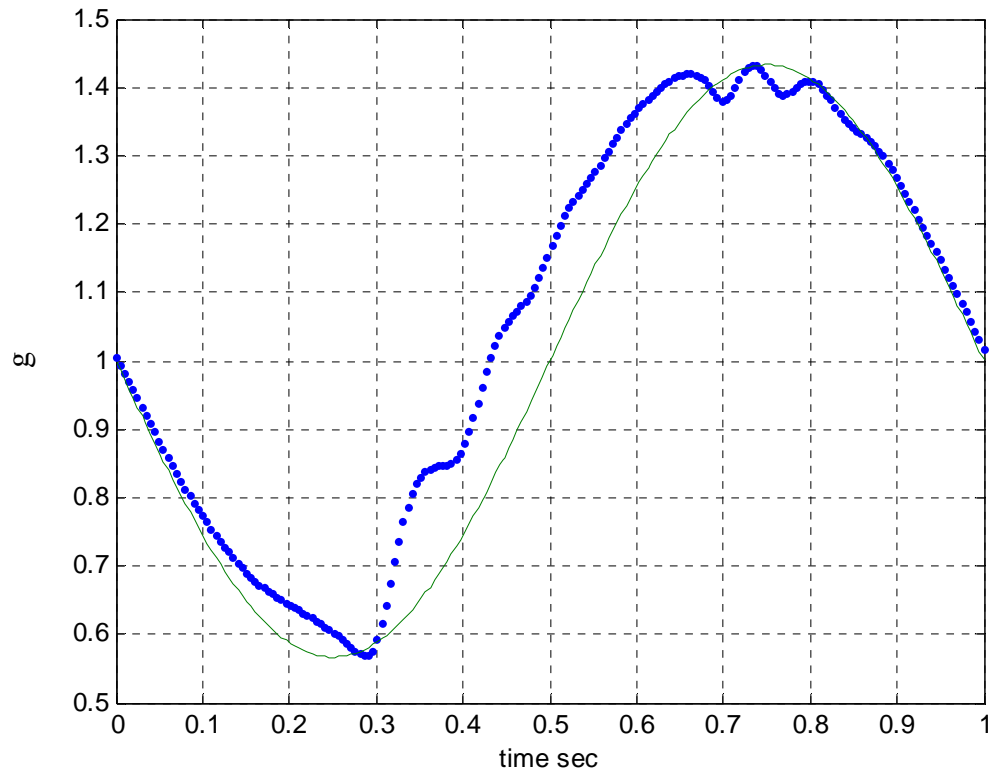


Figure 26. Comparison of the ideal and actual gravity modulations. Blue dots: actual measured gravity; Green line: ideal gravity.

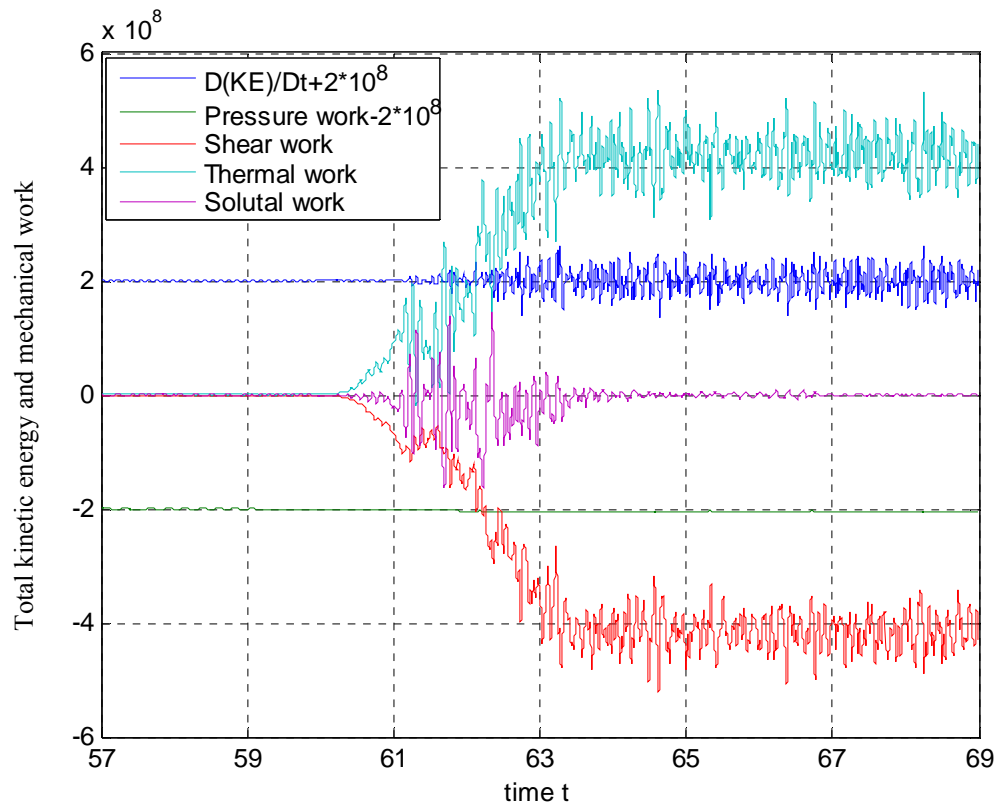


Figure 27. The time rate of change of the total kinetic energy and mechanical work by different forces throughout the instability onset under steady gravity. Note:  $\frac{D(KE)}{Dt}$  and pressure work are shifted upward and downward by  $2 \times 10^8$  respectively for clear view.

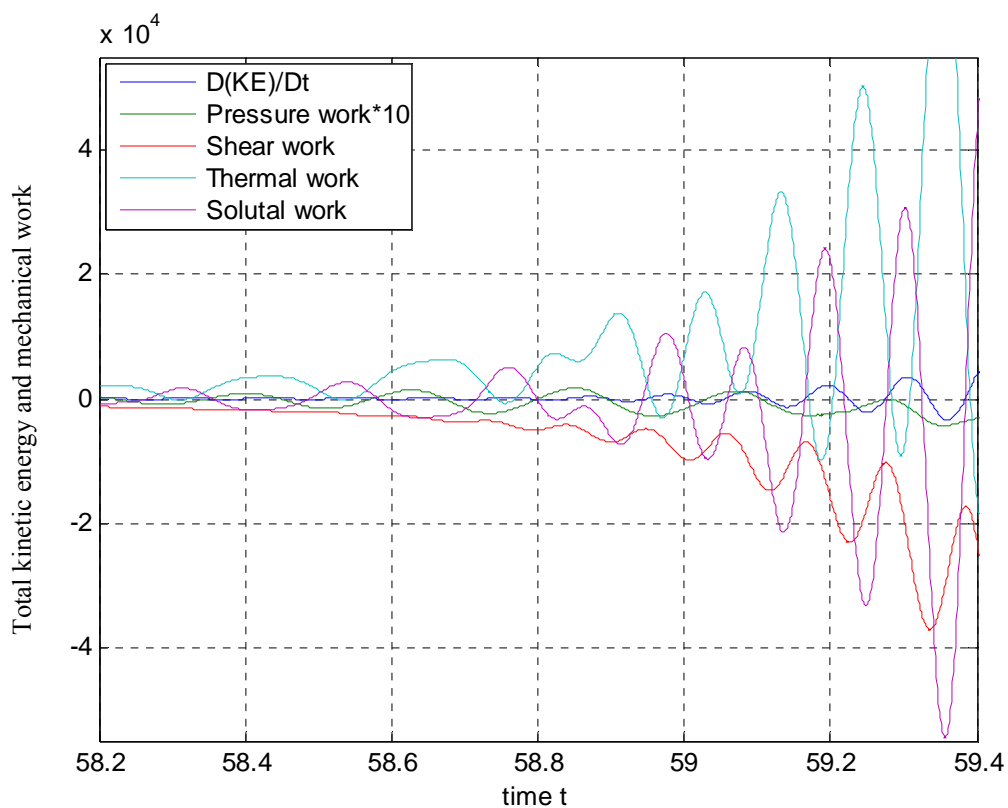


Figure 28. The oscillation frequencies of the total kinetic energy and mechanical work by different forces at the instability onset under steady gravity. Note: pressure work is magnified by factor of 10 for clear view.

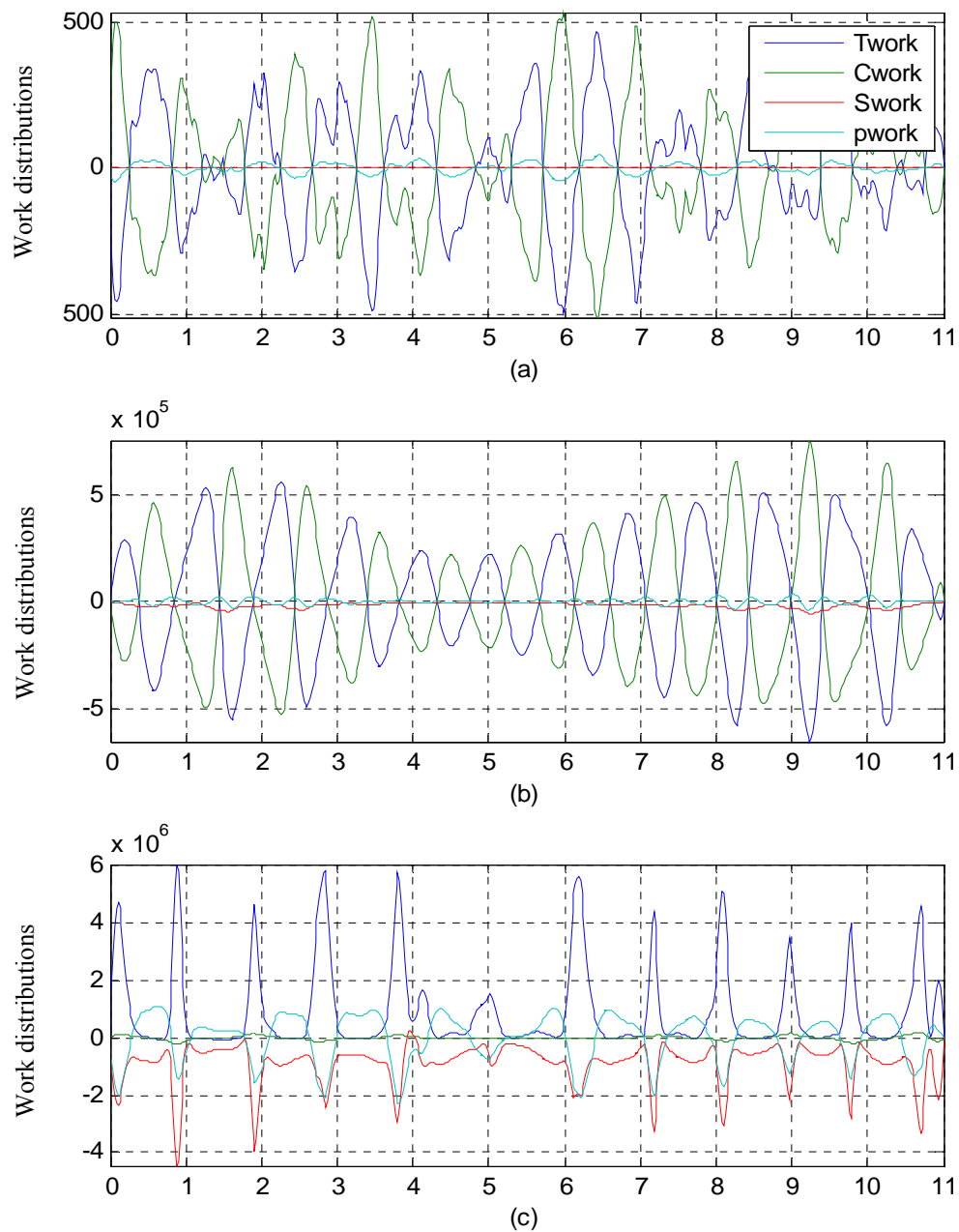


Figure 29. Longitudinal distributions of mechanical work by different forces  
 (a) before (b) at and (c) after the instability onset under steady gravity.

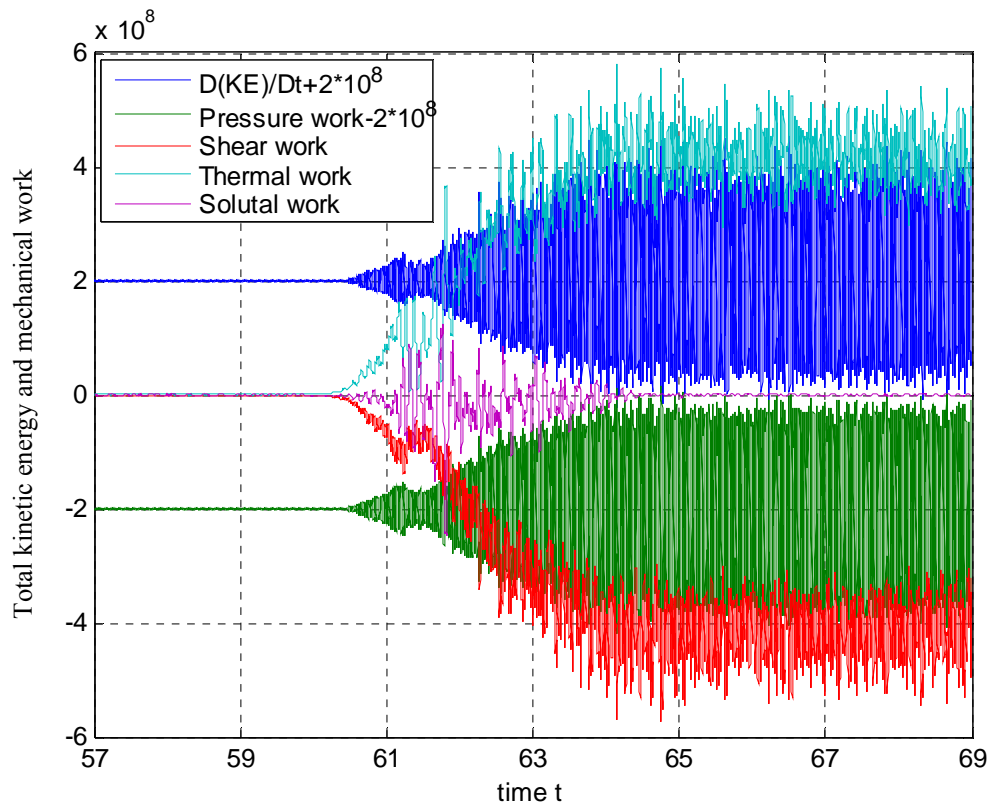


Figure 30. The time rate of change of the total kinetic energy and mechanical work throughout the instability onset under the ideal gravity of modulation of  $\omega_m = 628.3$  and  $gy_1 = 0.40$ . Note:  $\frac{D(KE)}{Dt}$  and pressure work are shifted upward and downward by  $2 \times 10^8$  respectively for clear view.

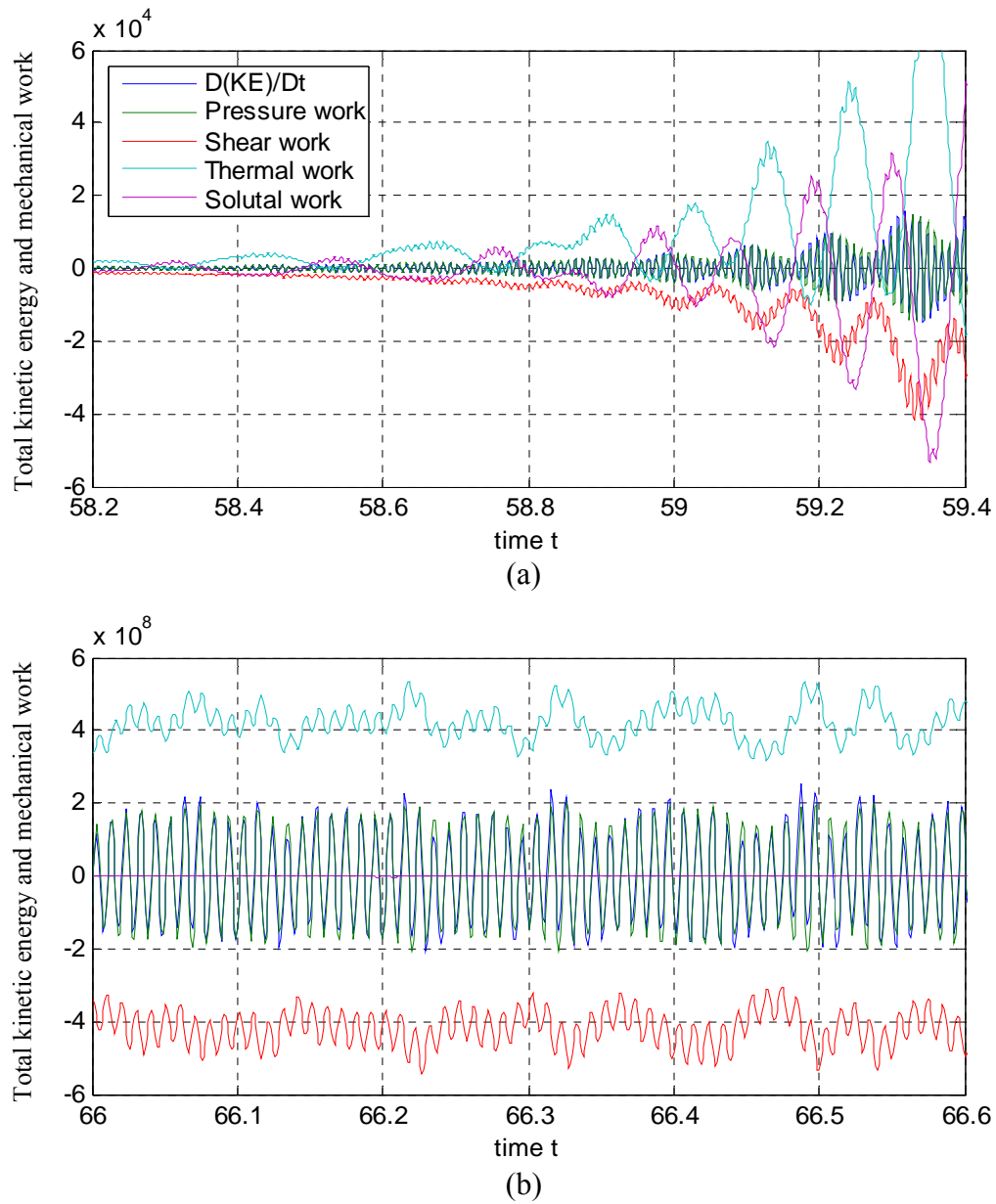


Figure 31. The oscillation frequencies of the total kinetic energy and mechanical work components (a) at (b) after the instability onset under the gravity modulation of  $\omega_m = 628.3$  and  $gy_1 = 0.40$ . Note:  $\frac{D(KE)}{Dt}$  is partially covered by pressure work due to their same oscillations.

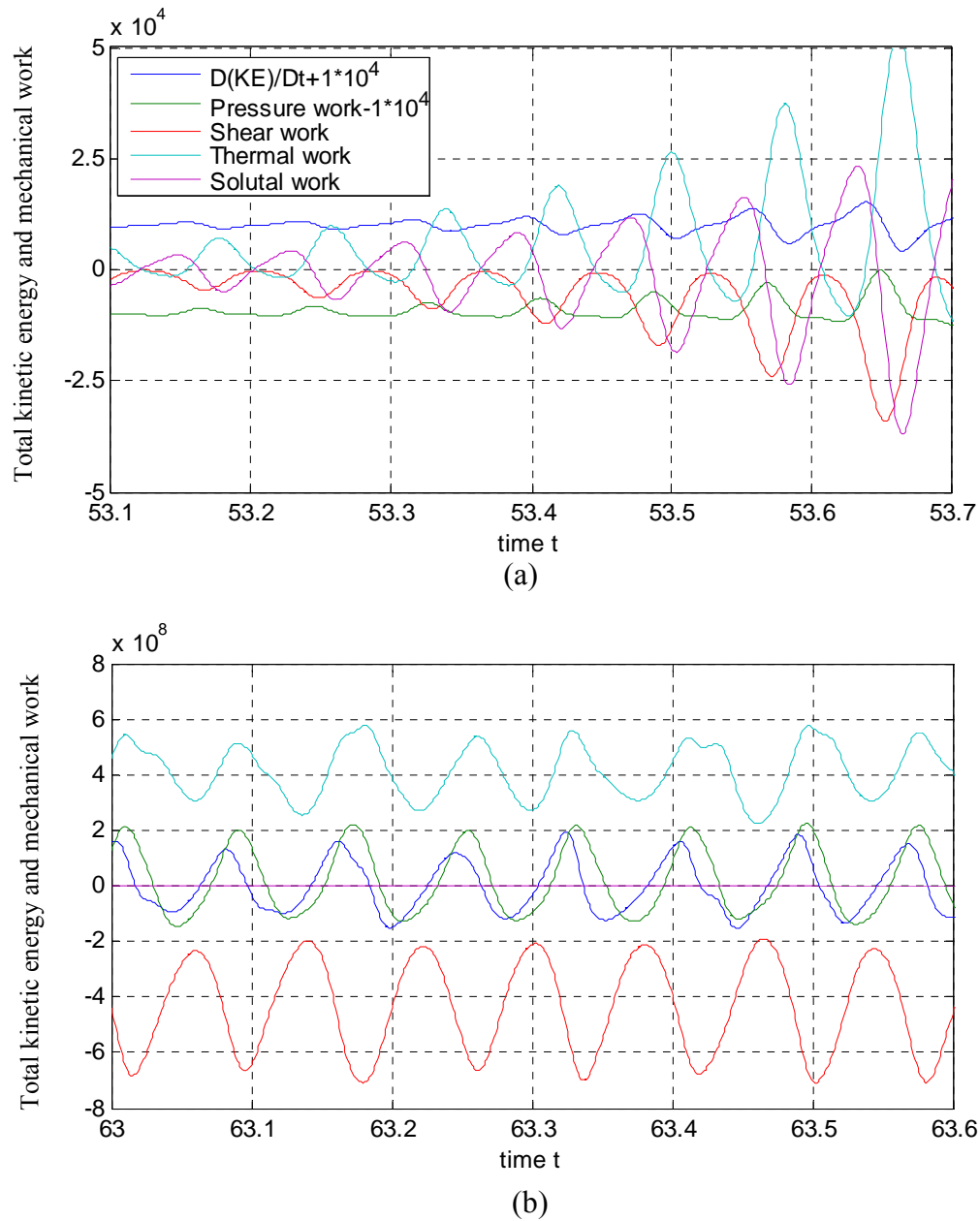


Figure 32. The oscillation frequencies of the total kinetic energy and mechanical work components (a) at (b) after the instability onset under the gravity modulation of  $\omega_m = 78.5$  and  $gy_1 = 0.40$ .  $\frac{D(KE)}{Dt}$  and pressure work are only shifted in (a) for clear view.

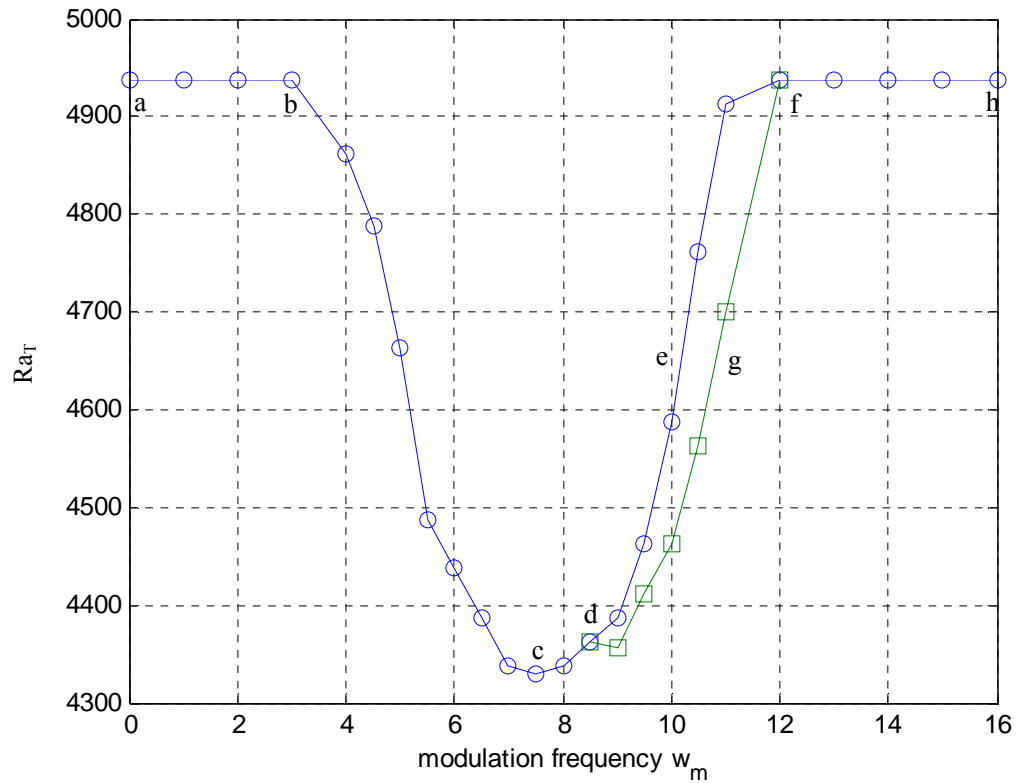


Figure 33. The resonance phenomenon under gravity modulation of  $gy_0 = 1.0$  and  $gy_1 = 0.40$ , with the condition of  $Pr = 7.0$ ,  $Le = 100$ ,  $Ra_s = 3200$  and linear temperature and solute profiles. Blue curve: double-diffusive instability; Green curve: density-mode instability.

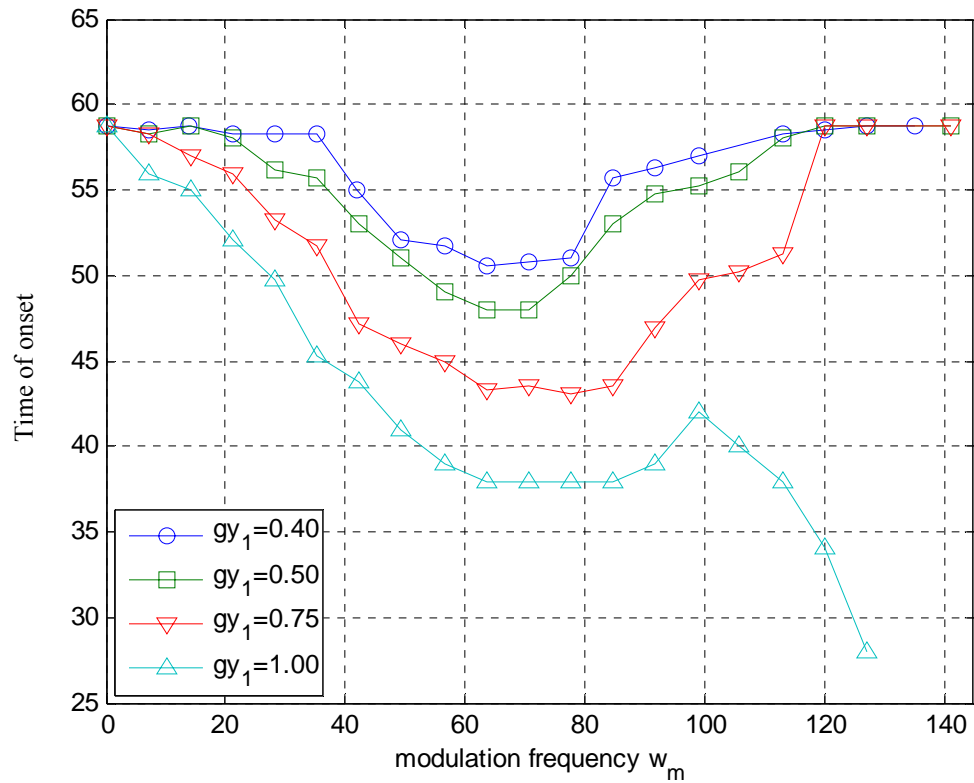
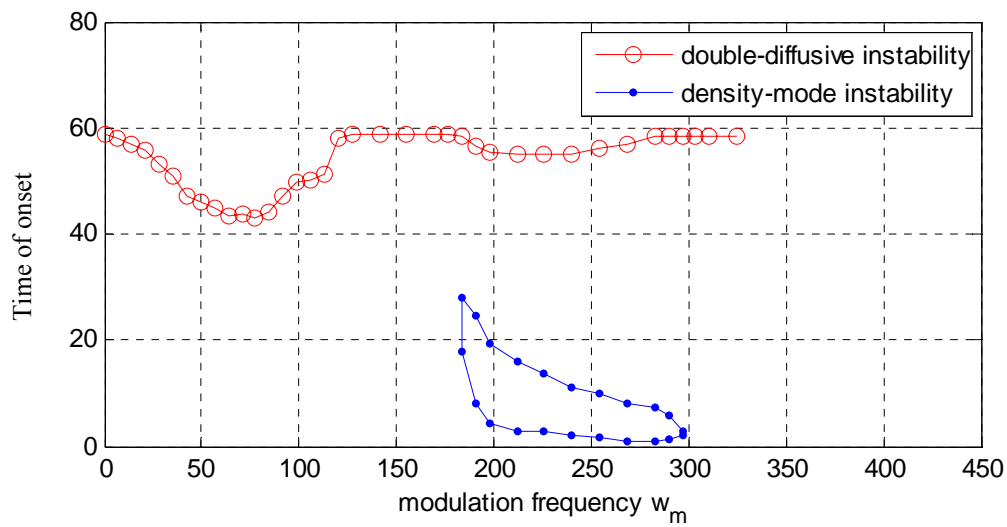
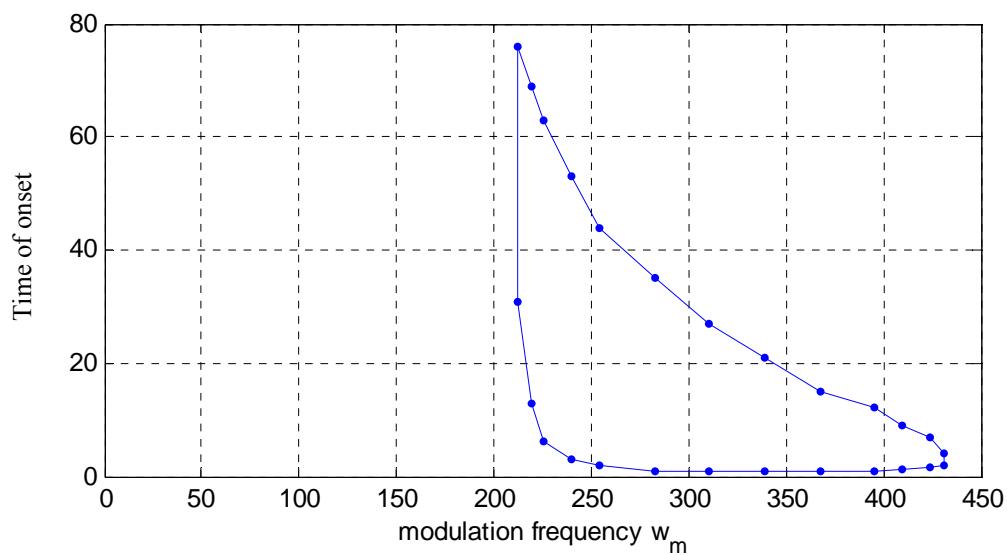


Figure 34. The resonance phenomenon under gravity modulation of  $gy_0 = 1.0$  and  $gy_1 = 0.40, 0.50, 0.75$  and  $1.00$ , with the lab condition of  $Pr = 7.0$ ,  $Le = 118.3$ , constant  $Ra_T = 161,560$  and initial  $Ra_S = 238,830$ .



(a)



(b)

Figure 35. The instability maps under gravity modulation of  $gy_1 = 0.75$  when (a)

$Ra_T = 161,560$  and (b)  $Ra_T = 0$ .

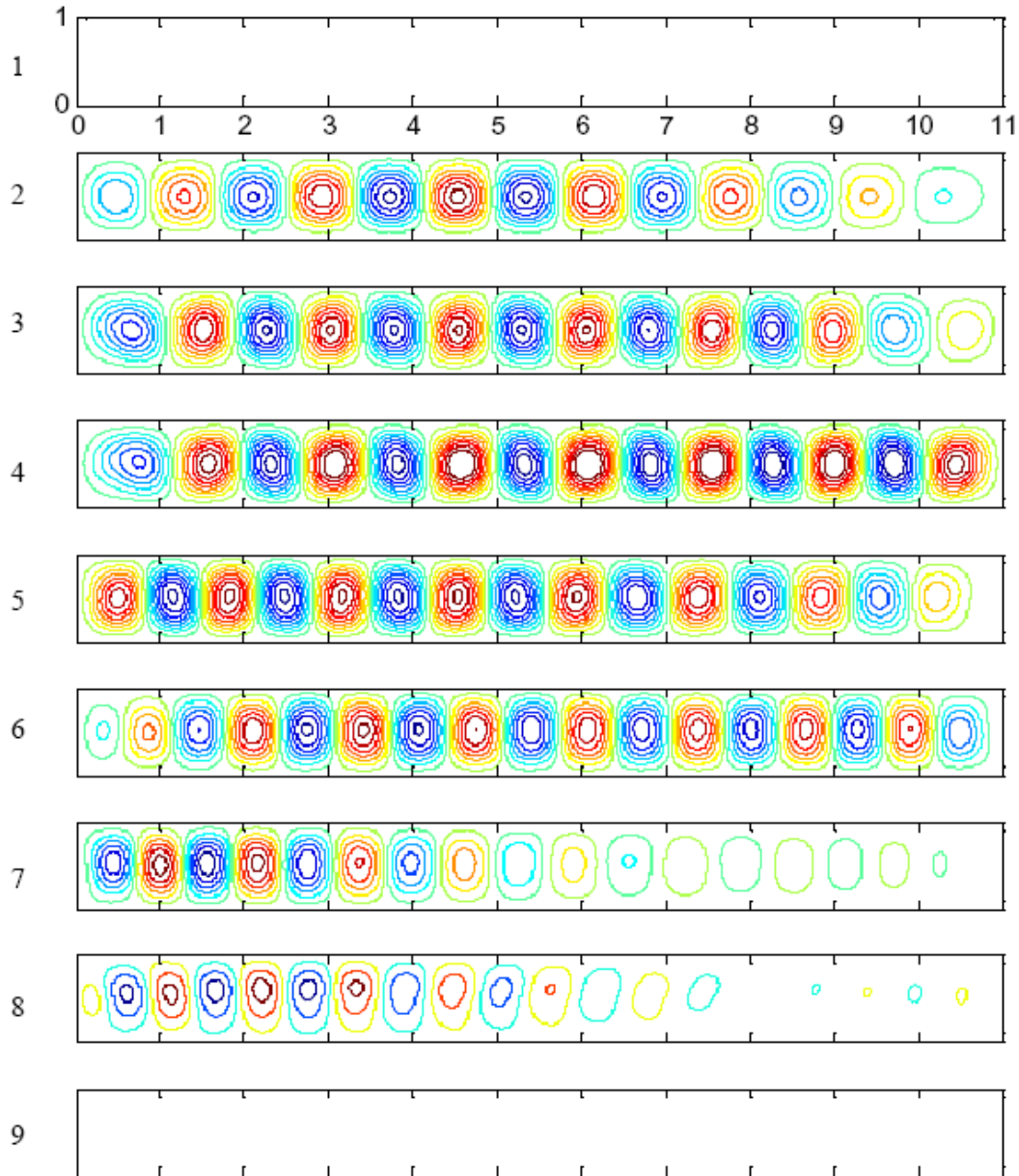


Figure 36. The time sequence of streamline contours of the unstable motion of the density-mode instability at  $Ra_T = 161,560$ ,  $\omega_m = 240.1$  and  $gy_1 = 0.75$ . Image 1 is at  $t = 2.0$ . (1)  $t = 1.0$ ,  $\Delta\psi = (-0.10 \sim 0.10)/16$ ; (2)  $t = 2.0$ ,  $\Delta\psi = (-0.25 \sim 0.25)/16$ ; (3)  $t = 3.0$ ,  $\Delta\psi = (-9.00 \sim 9.00)/16$ ; (4)  $t = 4.0$ ,  $\Delta\psi = (-9.00 \sim 9.00)/16$ ; (5)  $t = 6.0$ ,  $\Delta\psi = (-9.00 \sim 9.00)/16$ ; (6)  $t = 8.0$ ,  $\Delta\psi = (-4.00 \sim 4.00)/16$ ; (7)  $t = 9.0$ ,  $\Delta\psi = (-2.00 \sim 2.00)/16$ ; (8)  $t = 10.0$ ,  $\Delta\psi = (-0.20 \sim 0.20)/16$ ; (9)  $t = 11.0$ ,  $\Delta\psi = (-0.10 \sim 0.10)/16$ .

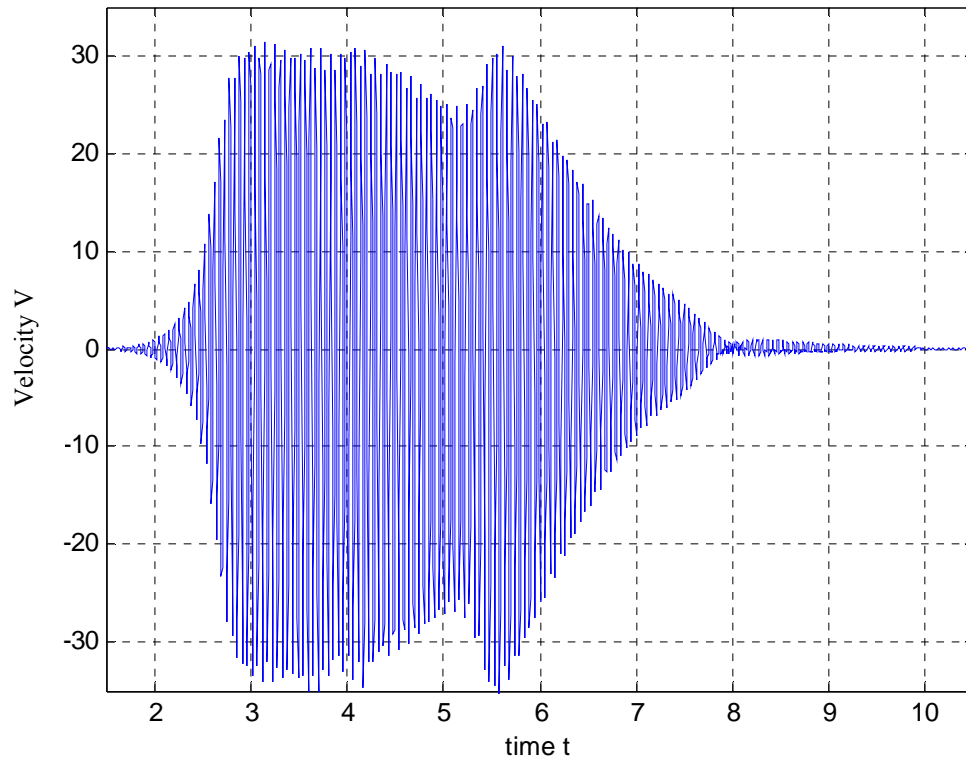


Figure 37. The evolution of vertical component of velocity  $v$  at point  $(5.5, 0.25)$  throughout the density-mode instability under gravity modulation of  $\omega_m = 240.1$  and  $gy_1 = 0.75$  with  $Ra_T = 161,560$ .

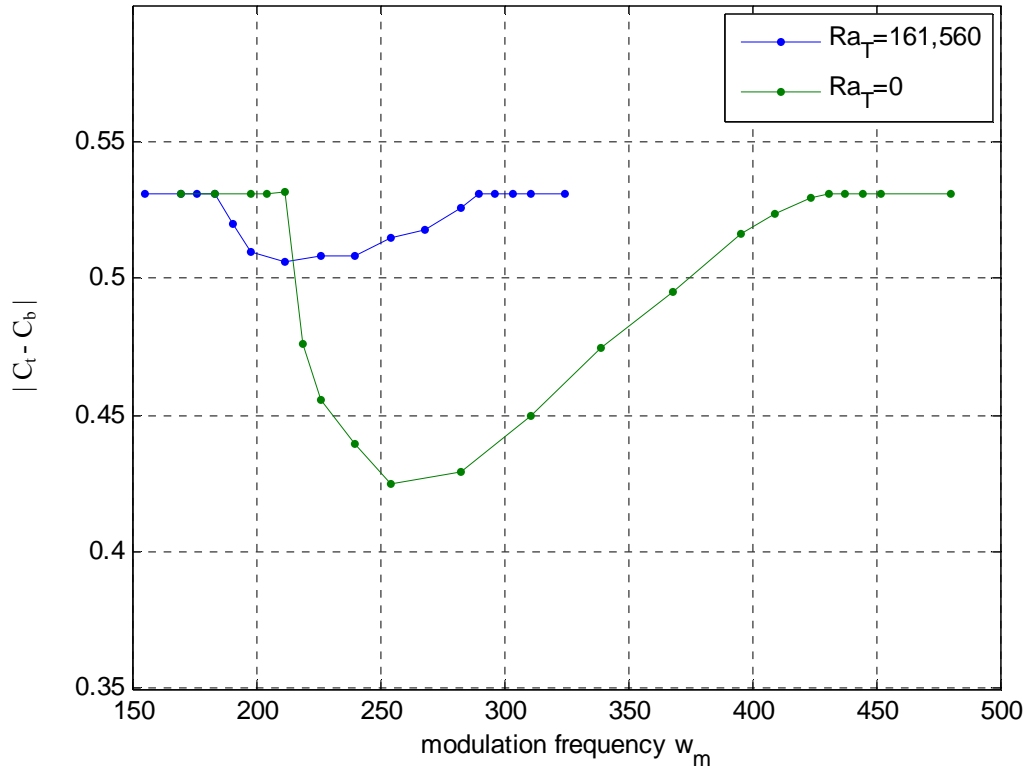


Figure 38. The solute differences across the fluid layer with (a)  $Ra_T = 161,560$  and (b)  $Ra_T = 0$  at  $t = 50.0$ . The corresponding  $Ra_S$  can be readily calculated by  $Ra_S = 250,240|C_t - C_b|$ .

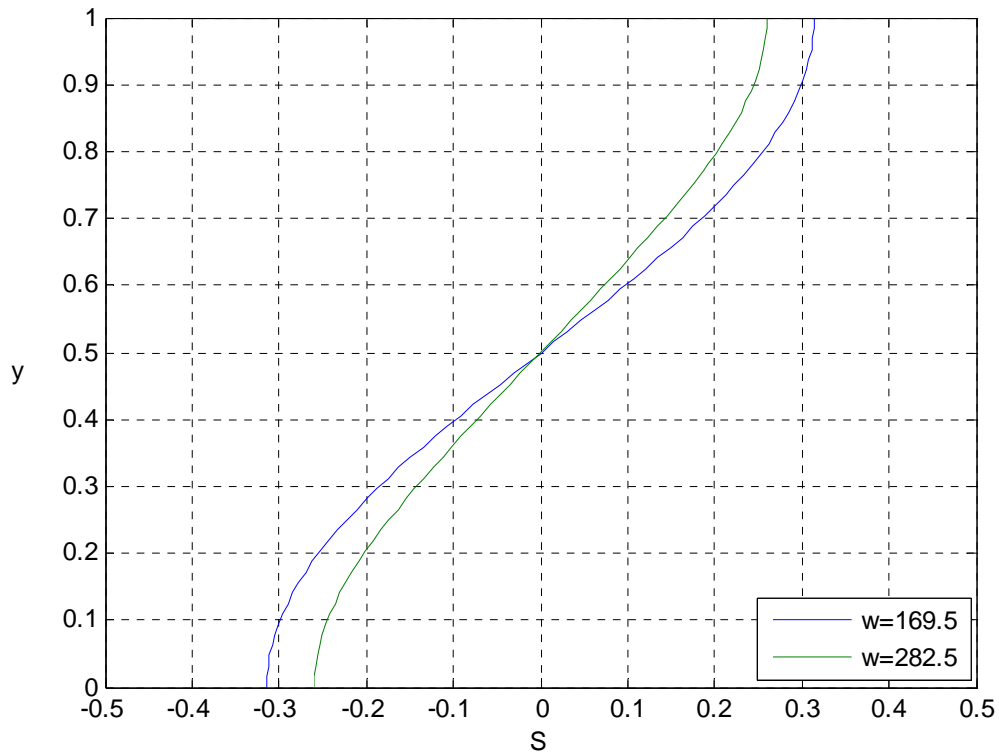


Figure 39. Solute profiles under modulated gravity of  $gy_1 = 0.75$  and  $\omega_m = 169.5, 282.5$  at  $t = 36.0$ . When  $\omega_m = 282.5$ , the fluid layer just comes out of the density-mode instability at this time. When  $\omega_m = 169.5$ , the fluid layer only experiences the diffusion up to this time. It is seen that the density-mode instability promote the mixing of the solute gradient.

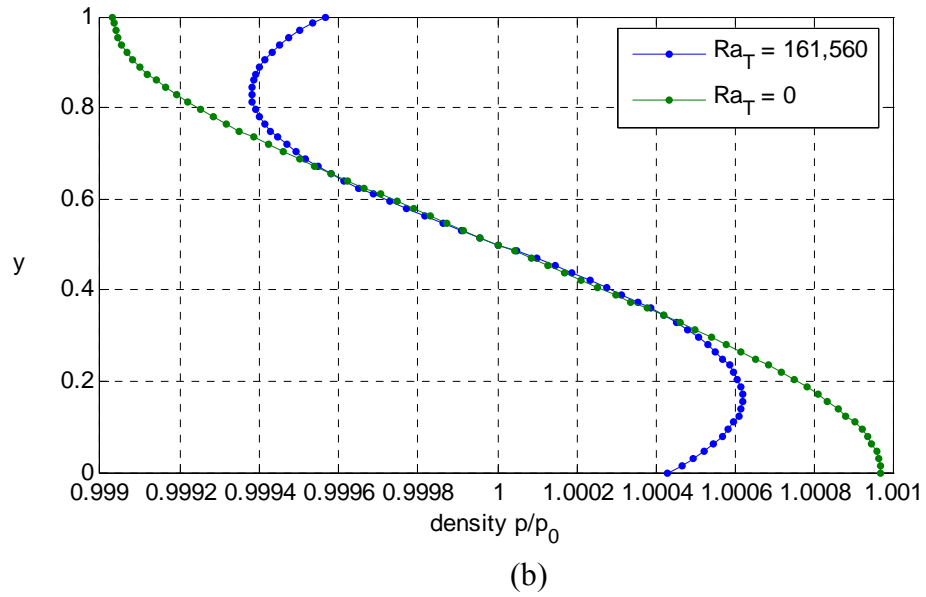
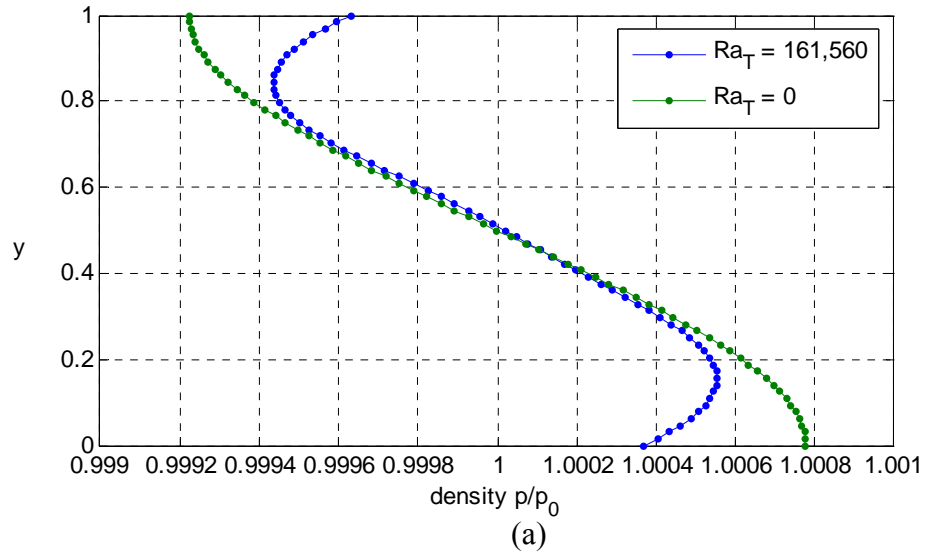
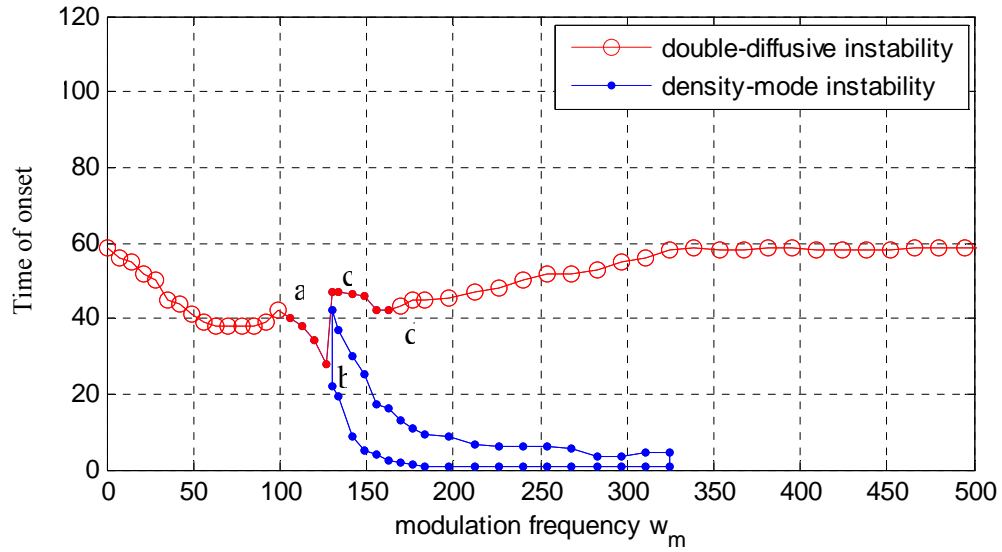
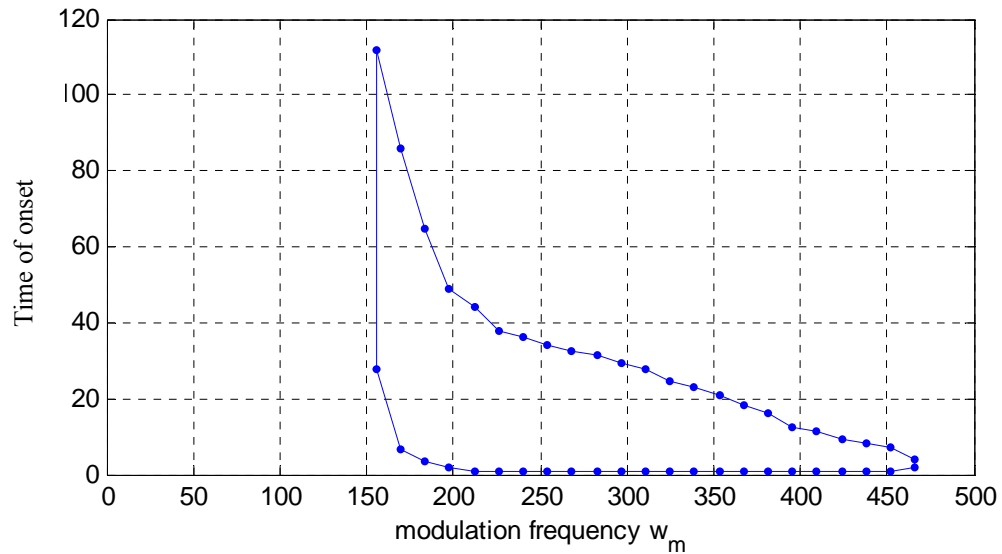


Figure 40. The distributions of non-dimensional density right after the density-mode instability under the gravity modulations of  $gy_1 = 0.75$  at (a)  $\omega_m = 240.1$  and (b)  $\omega_m = 282.5$ .



(a)



(b)

Figure 41. The instability maps under the gravity modulation of  $gy_1 = 1.00$  with (a)  $Ra_T = 161,560$  and (b)  $Ra_T = 0$ .

## APPENDIX B

## LIST OF TABLES

Table 1. Summary of $t_{onset}$ , $\Delta T$ and $Ra_T$ of experiments under steady gravity.....	122
Table 2. Summary of $t_{onset}$ , $\Delta T$ and $Ra_T$ of experiments under gravity modulation.....	123
Table 3. Summary of parameters at the instability onset determined by experiments and linear theory.....	124
Table 4. Summary of the parameters at the instability onset determined by computations under different gravity conditions.....	125
Table 5. Summary of $f_{onset}$ and $\omega_m$ of the density-mode instability with $gy_1 = 0.75$ and $Ra_T = 161,560$ .....	126
Table 6. Summary of $f_{onset}$ and $\omega_m$ of the density-mode instability with $gy_1 = 2.00$ and $Ra_T = 0$ .....	127
Table 7. Summary of $t_{onset}$ , $f_{onset}$ and $\omega_m$ with $gy_0 = 0.00$ , $gy_1 = 1.00$ , $Ra_T = 161,560$ and initial $Ra_T = 238,830$ .....	128

Table 1. Summary of  $t_{onset}$ ,  $\Delta T$  and  $Ra_T$  of experiments under steady gravity.

Exp	$t_{onset}$ min	$T_{inlet}$ °C	$T_{outlet}$ °C	$T_{bot}$ °C	$\Delta T_{\infty}$ °C	$\Delta T$ °C	$Ra_T$
H1(04/22/04)	99	17.18	17.04	28.31	11.20	10.26	163,080
H2(04/23/04)	98	17.16	17.00	28.17	11.09	10.16	161,540
H3(06/01/04)	92	17.15	17.04	28.20	11.11	10.17	161,770
H4(06/04/04)	90	17.13	17.00	28.07	11.01	10.08	160,310
H5(06/07/04)	91	17.17	17.03	28.16	11.05	10.12	160,910
H6(06/08/04)	99	17.17	17.01	28.20	11.11	10.17	161,770
Average	94.8	17.16	17.02	28.19	11.10	10.16	161,560

Note:  $T_{inlet}$ ,  $T_{outlet}$ ,  $T_{bot}$  are actually measured temperatures and first introduced in figure 2.

$\Delta T_{\infty} = T_{bot} - 0.5 \times (T_{inlet} + T_{outlet})$  and  $\Delta T = T_{bot} - T_{top}$ .  $\Delta T$  is solved from equation

$$\frac{\Delta T}{R_3} = \frac{\Delta T_{\infty}}{R_1 + R_2 + R_3} \text{ and } Ra_T \text{ is calculated by } Ra_T = \frac{g\beta_T H^3 \Delta T}{\kappa_T \nu} . R_1, R_2 \text{ and } R_3 \text{ are}$$

introduced in figure 2 as well.

Table 2. Summary of  $t_{onset}$ ,  $\Delta T$  and  $Ra_T$  of experiments under gravity modulation.

Exp	$t_{onset}$ min	$T_{inlet}$ °C	$T_{outlet}$ °C	$T_{bot}$ °C	$\Delta T_{\infty}$ °C	$\Delta T$ °C	$Ra_T$
H7(03/26/04)	90	17.17	17.04	28.29	11.18	10.24	162,790
H8(04/06/04)	87	17.19	17.05	28.27	11.15	10.21	162,360
H9(06/16/04)	91	17.15	17.01	28.29	11.21	10.27	163,230
H10(07/05/04)	82	17.16	17.03	28.10	11.00	10.07	160,170
H11(07/07/04)	81	17.21	17.06	28.15	11.01	10.08	160,310
H12(07/09/04)	87	17.17	17.02	28.16	11.06	10.13	161,040
H13(07/13/04)	82	17.19	17.04	28.06	10.94	10.02	159,290
Average	85.7	17.18	17.04	28.19	11.08	10.15	161,330

Note: The symbols and the procedure to determine  $\Delta T$  and  $Ra_T$  are the same as in Table 1.

Table 3. Summary of parameters at the instability onset determined by experiments and linear theory ( linear theory data, courtesy of Chen (2004)).

---

	$Ra_T$	$Ra_S$	$t_{\text{onset}}$	$f_{\text{onset}}$	$\lambda$
Experiment					
steady gravity	161,560	125,540	56.9/94.8min	27.02/0.043Hz	(0.91 ~ 1.09)
gravity modulation	161,330	136,140	51.4/85.7min	35.81/0.057Hz	(1.39 ~ 2.26)
Linear theory					
steady gravity	158,000	126,000	----	28.29	1.06
gravity modulation	158,000	126,000	----	----	----

---

Table 4. Summary of the parameters at the instability onset determined by computations under different gravity conditions.

	$Ra_T$	$Ra_S$	$t_{\text{onset}}$	$f_{\text{onset}}$	$\lambda$
Steady gravity					
$gx_0 = 0.00, gx_1 = 0.00$	161,560	122,560	58.2	28.27	(0.82 ~ 1.00)
$gx_0 = -0.01, gx_1 = 0.01$	161,560	124,030	57.0	28.27	(0.82 ~ 1.00)
Gravity modulation					
$gx_0 = 0.00, gx_1 = 0.00$ ideal modulation	161,560	122,560	58.2	28.27	(0.82 ~ 1.00)
$gx_0 = 0.00, gx_1 = 0.00$ actual modulation	161,560	124,330	55.8	30.66	(0.82 ~ 1.00)
$gx_0 = -0.01, gx_1 = 0.01$ ideal modulation	161,560	122,530	58.2	27.02	(0.82 ~ 1.00)
$gx_0 = -0.01, gx_1 = 0.01$ actual modulation	161,560	125,750	54.0	31.92	(0.82 ~ 1.00)

Table 5. Summary of  $f_{onset}$  and  $\omega_m$  of the density-mode instability with  $gy_1 = 0.75$  and  $Ra_T = 161,560$ .

---

$\omega_m$	185.5	197.7	211.9	226.0	240.1	254.3	268.4	282.5	296.6
$f_{onset}$	90.8	98.2	105.5	111.7	119.0	126.4	132.5	140.0	147.3
$\frac{f_{onset}}{\omega_m}$	0.49	0.50	0.50	0.49	0.50	0.50	0.49	0.50	0.50

---

Table 6. Summary of  $f_{onset}$  and  $\omega_m$  of the density-mode instability with  $gy_1 = 2.00$  and  $Ra_T = 0$ .

---

$\omega_m$	28.3	42.4	56.5	70.6	84.8	98.9	...	508.5	536.8	565.0
$f_{onset}$	27.6	41.4	55.2	35.3	41.4	49.1	...	251.6	267.0	279.2
$\frac{f_{onset}}{\omega_m}$	0.98	0.98	0.98	0.50	0.49	0.50	...	0.49	0.50	0.49

---

Table 7. Summary of  $t_{onset}$ ,  $f_{onset}$  and  $\omega_m$  with  $gy_0 = 0.00$ ,  $gy_1 = 1.00$ ,  $Ra_T = 161,560$  and initial  $Ra_T = 238,830$ .

---

$\omega_m$	$t_{onset}$	$f_{onset}$	$f_{onset}/\omega_m$
14.1	0.0	----	----
28.3	0.0	----	----
42.4	0.0	----	----
56.5	0.0	----	----
70.6	0.0	----	----
84.8	0.0	----	----
113.0	0.0	55.8	0.49
141.3	0.0	70.0	0.50
157.1	0.0	77.9	0.50
169.5	0.0	168.1/84.1	0.99/0.50
183.6	0.0	182.2/90.8	0.99/0.49
197.7	0.0/52.8	196.3/98.2	0.99/0.50
211.9	56.4	210.5	0.99
235.6	55.8	233.8	0.99
268.4	57.0	266.3	0.99
314.2	57.0	311.7	0.99
353.2	57.6	350.4	0.99
392.7	59.4	389.6	0.99
424.3	61.8	420.9	0.99
471.2	64.2	467.6	0.99
509.0	66.0	505.0	0.99
565.5	67.8	560.8	0.99
596.9	72.6	592.1	0.99
628.3	71.4	623.4	0.99
659.7	71.4	654.1	0.99
691.1	73.8	685.4	0.99
785.4	75.6	779.2	0.99
942.5	80.4	934.5	0.99

---

## REFERENCES

- 1 ARAKAWA, A. 1966 Computational design for long-term numerical integration of the equations of fluid motion: two-dimensional incompressible flow. Part I. *J. Comput. Phys.* 1, 119-143.
- 2 BAINES, P.G. & GILL, A.E. 1969 On thermohaline convection with linear gradients. *J. Fluid Mech.* 37, 289-306.
- 3 CHAN, C.L., YU, Y. & CHEN, C.F. 2004 Instability of convection of an ethanol-water solution in a vertical tank. *J. Fluid Mech.* 510, 243-265.
- 4 CHEN, C.F., BRIGGS, D.G. & WIRTZ, R.A. 1971 Stability of thermal convection in a salinity gradient due to lateral heating. *Int. J. Heat Mass Transfer.* 14, 57-65.
- 5 CHEN, C.F. & JOHNSON, D.H. 1984 Double-diffusive convection: a report on an engineering foundation conference. *J. Fluid Mech.* 138, 405-416.
- 6 CHEN, W.-Y. 2001 Effect of gravity modulation on the stability of a horizontal double-diffusive layer. PhD dissertation. University of Arizona.
- 7 CHEN, W.-Y. 2004 Communication within research group.
- 8 CLEVER, R., SCHUBERT & G., BUSSE, F.H. 1993 Two-dimensional oscillatory convection in a gravitationally modulated fluid layer. *J. Fluid Mech.* 253, 663-680.
- 9 DUFORT, E.C. & FRANKEL, S.P. 1953 Stability conditions in the numerical treatment of parabolic differential equations. *Math. Tables Other Aids Comput.* 7, 135-152.

- 10 GRESHO, P.M. & SANI, R.L. 1970 The effects of gravity modulation on the stability of a heated fluid layer. *J. Fluid Mech.* 40, 783-806.
- 11 Hayes, M.H. 1996 *Statistical digital signal processing and modeling*. John Wiley & sons, Inc..
- 12 HOUSTIS, E.N. & PAPATHEODOROU, T.S. 1979 High-order fast elliptic equation solvers. *ACM Trans. Math. Software* 5, 431-441.
- 13 HUPPERT, H.E. & TURNER, J.S. 1981 Double-diffusive convection. *J. Fluid Mech.* 106, 299-329.
- 14 INCROPERA, F.P. & DeWITT, D.P. 2002 *Fundamentals of heat and mass transfer*. p.492 John Wiley & sons, Inc..
- 15 JUE, T.C. & RAMASWAMY, B. 2002 Numerical analysis of thermosolutal flows in a cavity with gravity modulation effects. *Heat & Mass Transfer* 38, 665-672.
- 16 LANDOLT, H. & BORNSTEIN, R. 1989 *Eigenschaften der Materie in ihren aggregatzustaden*, part5, p.640. Springer.
- 17 PROAKIS, J.G. & MSNOLAKIS, D.G. 1996 *Digital signal processing: principles, algorithms, and applications*. Prentice Hall, Upper Saddle River, N.J..
- 18 ROACHE, P.J. 1982 *Computational fluid dynamics*. Hermosa, Albuquerque, N.M..
- 19 SAUNDERS, B.V., MURRAY, B.T., McFADDEN, G.B., CORIELL, S.R. & WHEELER, A.A. 1992 The effect of gravity modulation on thermosolutal convection in an infinite layer of fluid. *Phys. Fluids A* 4, 1176-1189.
- 20 SCHMITT, R.W. 1994 Double diffusion in oceanography. *Ann. Rev. Fluid Mech.* 26, 255-285.

- 21 SHIRTCLIFFE, T.G.L. 1967 Thermosolutal convection: observation of an overstable mode. *Nature, Lond.* 213, 489-490.
- 22 SHIRTCLIFFE, T.G.L. 1969 An experimental investigation of thermosolutal convection at marginal stability. *J. Fluid Mech.* 35, 677-688.
- 23 SHU, Y., LI, B.Q. & DE GROH, H.C. 2001 Numerical study of g-jitter induced double-diffusive convection. *Numerical Heat Transfer Part A* 39, 245-265.
- 24 TANNY, J., CHEN, C.C. & CHEN, C.F. 1995 Effects of interaction between Marangoni and double-diffusive instabilities. *J. Fluid Mech.* 303, 1-21.
- 25 TERRONES, G. & CHEN, C.F. 1993 Convective stability of gravity-modulated doubly cross-diffusive fluid layers. *J. Fluid Mech.* 255 301-321.
- 26 TURNER, J.S. 1968 The behavior of a stable salinity gradient heated from below. 33, 183-200.
- 27 TURNER, J.S. 1973 *Buoyancy effects in fluids.* Cambridge University Press.
- 28 TURNER, J.S. 1974 Double-diffusive phenomena. *Ann. Rev. Fluid Mech.* 6, 37-56.
- 29 TURNER, J.S. 1985 Multicomponent convection. *Ann. Rev. Fluid Mech.* 17, 11-44.
- 30 WRIGHT, J.H. & LOEHRKE, R.I. 1976 The onset of thermohaline convection in a linearly-stratified horizontal layer. *Trans. ASME C: J. Heat Transfer* 98, 558-563.
- 31 YU, Y. 2002 The instability of the natural convection of an ethanol-water solution in a vertical slot. MS thesis. University of Arizona.